

LONG-TERM IRRADIATION EFFECTS
ON REACTOR-PRESSURE VESSEL STEELS
INVESTIGATIONS ON THE NANOMETER SCALE

DISSERTATION

zur Erlangung des Doktorgrades der Naturwissenschaften
(Dr. rer. nat.)

der

Naturwissenschaftlichen Fakultät II
Chemie, Physik und Mathematik
der Martin-Luther-Universität
Halle-Wittenberg

vorgelegt von

Herrn Dipl.-Phys. Arne Wagner
geb. am 13.05.1982 in Kronstadt

Gutachter:

1. Prof. Dr. Reinhard Krause-Rehberg, Martin-Luther-Universität Halle-Wittenberg
2. PD Dr. Frank Bergner, Helmholtz-Zentrum Dresden-Rossendorf
3. Prof. Dr. Guido Schmitz, Universität Stuttgart

Tag der Verteidigung: 01.06.2017

“ A thing is a thing,
not what is said
of that thing. ”

Susan Sontag, as quoted in *Birdman*

ABSTRACT

The exposure of reactor pressure vessel (RPV) steels to neutron irradiation gives rise to irradiation-enhanced diffusion, a rearrangement of solute atoms and, consequently, a degradation of the mechanical properties. The increasing age of existing nuclear power plants raises new questions specific to long-term operation. Two of them are addressed in this thesis: flux effects and the late-blooming effect. Can low-flux irradiations up to a given fluence be reproduced by more rapid high-flux irradiations up to the same fluence? Can the irradiation response of RPV steels be extrapolated to higher fluences or are there unexpected "late-blooming" effects.

Small-angle neutron scattering (SANS), atom-probe tomography (APT) and Vickers-hardness testing were applied. A novel Monte-Carlo based fitting algorithm for SANS data was implemented in order to derive statistically reliable characteristics of irradiation-induced solute-atom clusters. APT was applied in selected cases to gain additional information on the composition and the shape of clusters. Vickers hardness testing was performed on the SANS samples to link the nanometer-scale changes to irradiation hardening.

The investigations on flux effects show that clusters forming upon high-flux irradiation are smaller and tend to have a higher number density compared to low-flux irradiations at a given neutron fluence. The measured flux dependence of the cluster-size distribution is consistent with the framework of deterministic growth (but not with coarsening) in combination with radiation-enhanced diffusion. Since the two effects on cluster size and volume fraction partly cancel each other out, no significant effect on the hardening is observed.

The investigations of a possible late-blooming effect indicate that the very existence (yes or no) of such an effect depends on the irradiation conditions. Irradiations at lower fluxes and a lower temperature (255 °C) give rise to a significant increase of the slope of both cluster-volume fraction and hardening versus fluence. Irradiations at higher fluxes and a higher temperature (290 °C) do not lead to significant changes of slope.

APT allows Cu-free and Cu-containing solute-atom clusters to be treated separately. It turned out that Cu-free clusters are responsible for the observation of a late-blooming effect. A two-path mechanistic model of cluster formation rationalizes these findings. An essential ingredient of the model is the Mn segregation to self-interstitial atom clusters and the operation of these objects as nuclei for the formation of Mn-Ni-Si-enriched clusters. The model also rationalizes why no late-blooming effect was observed for the high-flux irradiations.

CONTENTS

ABSTRACT	vii
TABLE OF CONTENTS	ix
ABBREVIATIONS AND SYMBOLS	xi
1 INTRODUCTION	1
1.1 Background	1
1.2 Reactor-pressure vessel steels	1
1.3 Nanostructural evolution during neutron irradiation	4
1.4 Long-term irradiation effects	6
1.5 Aims and scope	7
2 NANOSTRUCTURAL CHARACTERIZATION TECHNIQUES	9
2.1 Overview	9
2.2 Small-angle neutron scattering (SANS)	11
2.2.1 Principles of SANS	11
2.2.2 Transformation to size domain	16
2.3 Atom-probe tomography (APT)	21
2.3.1 Principles of APT	21
2.3.2 Data treatment	24
3 EXPERIMENTS	29
3.1 Materials	29
3.1.1 Chemical composition	29
3.1.2 Thermal treatment	30
3.1.3 Irradiation conditions	31
3.1.4 Tensile Tests	33
3.2 Experimental set-up	35
3.2.1 Small-angle neutron scattering	35
3.2.2 Atom-probe tomography	40
3.2.3 Vickers hardness	43
4 RESULTS	45
4.1 Flux effects (SANS)	45
4.2 Late-blooming effect (SANS)	51
4.3 Late-blooming effect (APT)	57
5 DISCUSSION	67
5.1 Flux Effects	67
5.1.1 Approach	67
5.1.2 Normalization of cluster parameters	67
5.1.3 Models of cluster evolution	69
5.1.4 Models of hardening	73

5.2	Late-blooming effect	79
5.2.1	Overview	79
5.2.2	Heterogeneous nucleation via Cu-vac mechanism	82
5.2.3	Heterogeneous nucleation via Mn-SIA mechanism	84
5.2.4	Origin of the change of slope	86
5.2.5	RH irradiation versus BR2 irradiation	88
6	CONCLUSIONS	91
	BIBLIOGRAPHY	95
	LIST OF PUBLICATIONS	107
	LIST OF FIGURES	109
	LIST OF TABLES	111
	ACKNOWLEDGMENTS	113
	CURRICULUM VITAE	115
	DECLARATION	117

ABBREVIATIONS AND SYMBOLS

α	Obstacle strength
β	Geometry factor of APT tip
$\Delta\eta$	Scattering contrast
ΔR	Cluster radius increment
$\Delta\sigma_y$	Yield stress increase
ΔT	Transition temperature shift
ΔHV_{10}	Vickers hardness increase
η	Scattering length density
θ	Half scattering angle
λ	Neutron wave length
ρ_{CL}	Threshold of cluster element concentration
ϕ	Neutron flux
ϕ_t	Transition neutron flux
ϕt	Neutron fluence
ψ	Neutron wave function
a	Lattice parameter of bcc Fe
aDLD	Advance delay line detector
A	A ratio
APT	Atom-probe tomography
$b_{nuc/mag}$	Nuclear/magnetic scattering length
b	Burgers vector
BKS	Bacon-Kocks-Scattergood
BR2	Material-test reactor in Mol, Belgium
C_m	Monomer concentration
CL	Cluster elements
CoS	Change of slope
CRC	Cu-rich cluster
CVN	Cu-vacancy nucleus
d_s	SANS sample thickness
d_{at}	Atomic plane distance
d	Obstacle diameter
$d\Sigma/d\Omega$	Macroscopic scattering cross section
D_{th}	Thermal diffusion constant
DB	Dispersed barrier
E_{bind}	Lattice binding energy
E_{kin}	Kinetic energy of a neutron
E	Electric field strength
ECoWATAP	Energy compensated wide-angle tomographic atom probe

f_v	Cluster volume fraction
F	SANS form factor
FEG-STEM	Field-emission gun - scanning TEM
FlexTAP	Flexible tomographic atom probe
FKH	Friedel-Kroupa-Hirsch
FP	Frenkel pair
G	Shear modulus
G_m	Monomer generation term
GiPS	Gamma-induced positron spectroscopy
I	SANS scattering intensity
ICP-MS	Inductively coupled plasma-mass spectrometry
IFT	Indirect Fourier transformation
k_b	Boltzmann constant
K_m	Monomer reaction-rate constant
L	APT sample-detector distancer
LBE	Late-blooming effect
LTO	Long-term operation
LaWATAP	Laser-assisted wide-angle tomographic atom probe
m/n	Mass-over-charge ratio
M	Taylor factor
MCF	Monte Carlo fitting
MCP	Micro-channel plate
MD	Matrix damage
ME	Maximum entropy
MNC	Mn-Ni(-Si)-rich cluster
MTR	Material-test reactor
n	Ion charge state
N_{mon}	Neutron monitor counts
N	Cluster number density
NPP	Nuclear power plant
P	APT projection point
PAS	Positron-annihilation spectroscopy
PD	Point defect
PFPE	Perfluoropolyether
PKA	Primary knock-on atom
PSD	Position sensitive detector
Q_{act}	Activation energy
Q_{eff}	APT detector efficiency
Q	SANS scattering vector
r_0	Monomer recombination radius
r_e	Classical electron radius
\bar{R}	Mean cluster radius
R_{gyr}	Radius of gyration
R_{max}	Maximum cluster radius

R_{\min}	Minimum cluster radius
R_{tip}	Tip radius of APT needle
RB	Russel-Brown
RED	Radiation-enhanced diffusion
RH	VVER prototype reactor in Rheinsberg, Germany
RPV	Reactor pressure vessel
S	SANS structure factor
SANS	Small-angle neutron scattering
SD	SANS sample-detector distance
SEM	Scanning-electron microscopy
SIA	Self-interstitial atom
SIAC	Self-interstitial atom cluster
t_{irr}	Irradiation time
T_{irr}	Irradiation temperature
T	SANS transmission factor
TEM	Transmission electron microscopy
TOF	Time of flight
U_{\sim}	High frequency voltage
U_0	Standing voltage
U_m	Monomer interaction energy
V_{at}	Volume of bcc-Fe atom
VVER	Water-water energetic reactor

INTRODUCTION

1.1 BACKGROUND

The global demand of emission-free electricity continues to rise in today's society. Nuclear energy is one pillar of energy sources available in Europe, constituting about 30 % of the current mix of techniques. However, over a third of the nuclear power plants (NPPs) in Europe are older than 30 years [1] and are going to reach the end of their planned lifetime in ten years or less. One of the strategies to satisfy the increased energy demand, without increasing the global carbon dioxide emission, is the extension of the lifetime of the NPPs from originally planned 40 years of operation to 60 – 80 years.

This raises the essential question, whether the long-term operation (LTO) of an NPP poses potential safety risks, in particular with regard to long-term irradiation effects on the reactor-pressure vessel (RPV), which is the main barrier for shielding the radioactive fuel from the outer environment. Since the RPV is considered to be irreplaceable, its structural integrity directly limits the lifetime of an NPP.

During its operation, the RPV is exposed to high energy neutrons emitted from the core fuel. This has significant detrimental effects on the mechanical properties of the RPV, which manifest themselves in an increased hardening and embrittlement of the material. Since the early 1970s, the effects of neutron irradiation on RPV steels have not only been studied by mechanical testing but also on a nanostructural level. It was revealed that the deterioration of the mechanical properties mainly originates from nanometer-sized defect-solute clusters, which impede the free movement of dislocations in the Fe lattice. Despite the significant progress that has been made in the understanding of the nature of irradiation-induced features, some major points, in particular related to long-term effects of neutron irradiation, are not well understood. This is a matter of ongoing international research projects.

1.2 REACTOR-PRESSURE VESSEL STEELS

RPV CONSTRUCTION: The RPV in a light-water reactor is made from a low-alloy ferritic steel with a body-centered cubic (bcc) lattice structure. During manufacturing, the steel is forged to rings of about 3 to 4 m in diameter, which are welded to form the circumferential part of the pressure vessel. Fig. 1 shows a technical drawing and a photograph of an RPV from the now decommissioned VVER-prototype reactor in Greifswald, Germany. The highlighted region next to the reactor core is exposed to the highest neutron fluences. This region consists of base material and weld. Both base material and weld are required to be investigated.

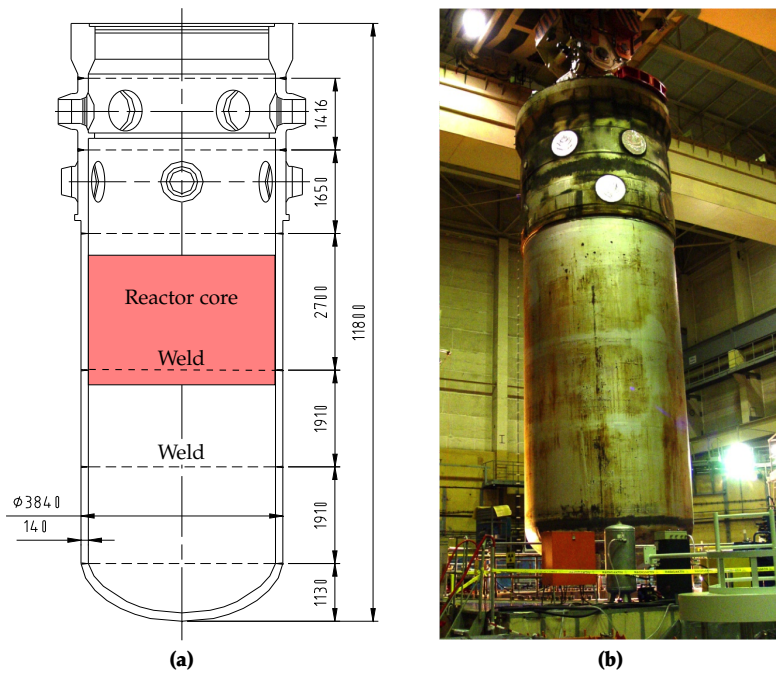


Figure 1: (a) Technical drawing of a VVER-type RPV, dimensions given in mm. The highlighted region next to the reactor core is exposed to the highest neutron fluences. (b) Photograph of a dismantled RPV of the decommissioned VVER-prototype reactor in Greifswald, Germany. By courtesy of Dr. H.-W. Viehrig.

For safe operation, the steels used for RPVs are required to have a high fracture toughness to prevent brittle fracture even under severe loading conditions, such as a pressurized thermal shock during emergency cooling.

The required properties of the steels are obtained with the addition of alloying elements to the heat, followed by a specific thermal treatment. The chemical composition and the heat treatment govern not only the initial mechanical properties of the metal but also the sensitivity to neutron irradiation. The three alloying elements [2] known to be most responsible for the sensitivity to neutron irradiation are Manganese, Nickel and Silicon.

- The addition of Mn reduces the brittleness of the steel by binding free sulfur. Furthermore, Mn refines the grain structure and acts as a deoxidizing agent.
- Ni is added to increase fracture toughness and improve forgeability.
- Si is added to operate as deoxidizer at the molten stage.

Some impurity elements such as Copper and Phosphorus are also known to have a significant influence on the steel's susceptibility to irradiation.

- Cu has a solubility limit of about 0.005 wt.% [3, 4] at typical RPV operation temperatures. Since the late 1960s it is known that residual Cu can cause serious hardening and embrittlement upon neutron irradiation. In modern RPV steels the residual Cu is restricted to be well below 0.05 wt.%.

- P tends to segregate to the grain boundaries of the steel. This can lower the cohesion between grains and can, therefore, lead to intergranular fracture in the material, which is the origin of non-hardening embrittlement.

To summarize, the sensitivity to irradiation of the steel is governed by the material composition, that is, the type and amount of alloying elements added to the heat and the purity with regard to residual elements.

RPV IRRADIATION: The fuel core in the center of the RPV emits high energy neutrons. The surrounding materials are exposed to a relatively low neutron flux between 1.2 and $4 \cdot 10^{10}$ n cm⁻² s⁻¹. After 40 years of operation [5] this amounts to a fluence of about $4 \cdot 10^{19}$ n cm⁻².

As the continuous irradiation of the RPV leads to a degradation of the mechanical properties, this process needs to be monitored. One approach for this safety assessment is based on the accelerated irradiation of surveillance samples. To this end, samples of the same base and weld material as used for the actual RPV are inserted into an irradiation channel close to the fuel rods. The increased neutron flux at this position leads to the accumulation of a certain fluence level in a shorter time period. After a specific sample accumulated the required fluence, it is removed from the irradiation channel and its mechanical properties are tested. The test results give insight to the irradiation susceptibility of the specific material used for the RPV, and the material behavior during the next surveillance interval can be anticipated.

Additionally, an interest to describe the materials behavior under irradiation in terms of empirical embrittlement trend curves arose. These trend curves express the hardening and embrittlement as a function of neutron fluence as a shift in Charpy impact transition temperature, ΔTT . ΔTT can also be expressed in terms of an increase in yield stress, $\Delta\sigma_y$, or hardening, ΔHV_{10} , since the three units are strongly correlated. There are different assumptions on how embrittlement evolves as a function of neutron fluence. In most cases, a power-law dependence turned out to be suitable:

$$\Delta TT = \chi (\phi t)^n \quad (1)$$

The chemical pre-factor, χ , expresses the dependency of the embrittlement on the chemical composition of the steel. The exponent, n , is less than one and was found [6] to be in many cases around $n = (0.4 \pm 0.2)$, as shown in Fig. 2, indicated by the black solid line and the grey scatter band.

However, there is increasing evidence [7–9] that under certain conditions the fluence dependence of hardening and embrittlement does not follow a power-law-like dependency with an exponent $n < 1$. Instead, a late onset of an additional embrittlement mechanism was anticipated [7]. The main feature of this behavior is a (gradual or abrupt) change of slope, typically an increase of slope of the curve. This effect, also referred to as late-blooming effect (LBE), is depicted by the dotted line in Fig. 2.

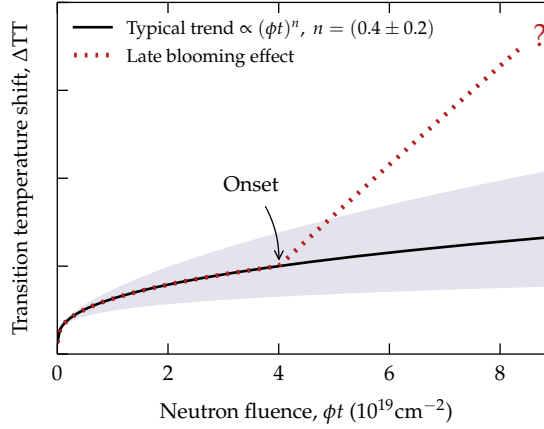


Figure 2: Schematic plot of the evolution of the irradiation damage, represented by the transition temperature shift, $\Delta T T$, as a function of neutron fluence, ϕt , and its exponent, n .

1.3 NANOSTRUCTURAL EVOLUTION DURING NEUTRON IRRADIATION

The nuclear fission in the reactor core leads to the emission of high-energy neutrons penetrating the surrounding materials. If a high-energy neutron passes through an RPV steel, it can collide with lattice atoms of the metal. A neutron with a kinetic energy of $E_{\text{kin}} = 1$ MeV transfers up to 70 keV to a single Fe atom. The energy transfer from the high-energy neutron to this primary knock-on atom (PKA) leads to its displacement from the lattice site. The accelerated PKA interacts with the surrounding lattice atoms in a series of collisions, leading to further displacements of surrounding atoms in a tree-like manner and the formation of Frenkel pairs (FPs). Part of the recoil energy during this process dissipates in the electron cloud of the metal. This process continues until the energy of the PKA is lower than the lattice binding energy of $E_{\text{bind}} = 40$ eV in bcc Fe. The maximum number of FPs created during the cascade is reached within 1 to 2 ps. A single neutron-PKA collision can induce several hundreds of displacements in the surrounding volume. A schematic representation of the collision cascade caused by a single high-energy neutron is shown in Fig. 3a. Fig. 3b shows a simulated [10] distribution of vacancies (red) and interstitials (green) at the time of maximum damage. The majority of vacancies and interstitials annihilate already within 5 – 7 ps after the neutron collision and, depending on the irradiation temperature, only a small fraction of point defects (PDs) remains in the surrounding lattice volume.

PDs are mobile in the lattice. Interstitials migrate and rearrange to form disk-shaped self-interstitial clusters, also referred to as dislocation loops. Similarly, vacancies migrate and form vacancy clusters. Grain boundaries and pre-existing dislocations act as point defect sinks. The supersaturation of PDs, in particular vacancies, in the Fe lattice leads to irradiation-enhanced diffusion of solute atoms giving rise to the rearrangement of solute atoms including the formation of solute atom clusters and the segregation to grain boundaries. Dislocation loops, vacancy clusters

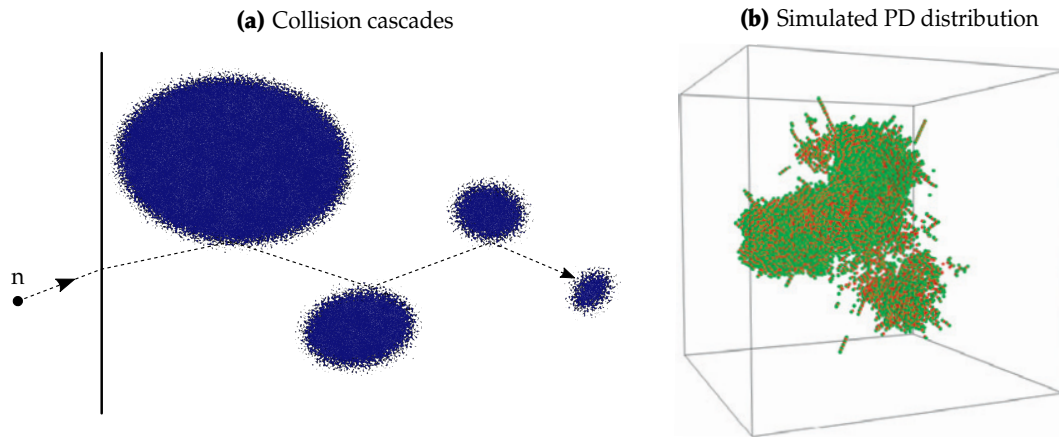


Figure 3: (a) Schematic representation of a collision cascade. PDs are represented by blue dots. (b) Simulated PD distribution [10] of a collision event at peak damage for a 20 keV incident neutron. Vacancies and interstitials are indicated by red and green spheres, respectively.

and solute atom clusters additionally impede the movement of dislocations through the lattice. This is the origin of the increase in hardening and embrittlement upon neutron irradiation.

The nano-scale features formed upon neutron irradiation are typically characterized in two main categories, that is, matrix damage (MD) and solute-atom clusters. MD refers to self-interstitial atoms, vacancies and their clusters.

Solute-atom clusters comprise alloying and impurity elements, such as Cu, Mn, Ni and Si. Depending on the Cu content of the RPV steel, two different types of clusters, which form upon neutron irradiation, are typically distinguished in the literature. In high-Cu steels, Cu is the main constituent of the clusters forming during neutron irradiation. These clusters are known as Cu-rich clusters (CRCs). Other elements, such as Mn and Ni, are also found in the CRCs, but to a lesser extent than Cu.

In low-Cu steels (< 0.1 wt.% Cu), the clusters are composed mainly of Mn, Ni and Si and only a small amount of Cu is found. By definition, a cluster is referred to as Mn-Ni(-Si-rich) cluster (MNC) if the sum of Mn, Ni and Si atoms is more than the amount of Cu atoms.

Note that the distinction between low- and high-Cu material at a threshold of 0.1 wt.% Cu is not made due to physical considerations. In fact, it is generally accepted in the literature [5, 11–13] that CRCs are the predominant features at Cu levels well above 0.1 wt.% and MNCs well below this value, with a region of overlap near this threshold.

The formation of CRCs in irradiated high-Cu steels can be rationalized by the strong supersaturation of Cu in the Fe matrix. Neutron irradiation, leading to radiation-enhanced diffusion [14], merely accelerates the precipitation of Cu.

In contrast, this reasoning cannot be adopted to the formation of MNCs in low-Cu RPV steel. The concentrations of Mn, Ni and Si are well below the solubility limit at typical irradiation temperatures. Thus, under separate consideration of the

solubility limits of either Mn in Fe or Ni in Fe or Si in Fe, the solutes would stay in solid solution even upon neutron irradiation.

1.4 LONG-TERM IRRADIATION EFFECTS

MNCs were clearly identified only in the mid-1990s, when newly acquired SANS and FEG-STEM data were combined [15] with previously published [16] SANS results.

In subsequent studies [7, 11, 17], the experimental findings [15] of MNCs were reproduced by means of equilibrium lattice Monte Carlo simulations [7, 11, 17] with inputs taken from a CALPHAD [18] database. According to these simulations, it is energetically favorable for Mn, Ni and Si to cluster around a core of Cu atoms and to form a new phase. A low irradiation temperature, high fluence and low neutron flux, i.e. long irradiation times, would favor the formation of such a phase [7, 11, 15, 17].

In addition, the simulations predicted an incubation period for the formation of MNCs in high-Cu materials. At high fluence levels, once most of the supersaturated Cu in a high-Cu steel is trapped in CRCs, the matrix is low in Cu concentration. In the matrix, now being essentially a low-Cu steel, the formation of MNCs is triggered and the cluster volume fraction increases again at a different rate. It is due to the delayed appearance of these thermodynamically stable phases that MNCs are also known as *late-blooming phases* (LBPs).

Recently, the naming LBP has been under debate, e.g. [19, 20], as the naming implicates much about the origin and nature of these features. This is, however, a matter of ongoing scientific discussions: While the classical approach on the basis of Odette's findings [15] suggests that MNCs are thermodynamically stable phases and that these phases appear late, i.e. after exceeding a threshold fluence, more recent publications [19, 21–23] argue that the formation of MNCs cannot be explained on thermodynamical grounds, but is rather a consequence of solute-atom segregation to PD clusters. In any case, agreement on the dominant formation mechanism and detailed structure of MNCs has not yet been reached.

The label “late-blooming *effect*” (LBE) seems to be more appropriate than the debatable term “late-blooming *phase*”, as it does not implicate any assertion on the formation mechanism or thermal stability of the nanoscale features.

The other long-term irradiation effect discussed in this thesis is the influence of neutron flux on the irradiation response of RPV steel. As introduced in Section 1.2, the standard safety procedure in NPPs is based on the accelerated irradiation, that is irradiations at higher flux of surveillance samples to anticipate the neutron embrittlement at higher fluence levels in a shorter period of time. In some reactors, typically in those of highest age, surveillance material was not foreseen, is used up or not available for additional testing to a sufficient extent.

Whether or not surveillance samples are available, research aimed at assessing safe operation is accompanied by more basic, understanding-oriented research. The required irradiations are performed in material-test reactors at even higher fluxes

than those allowed for the purpose of surveillance testing. This additionally raises the importance of an understanding of flux effects. How the flux effects manifest themselves in terms of differences in the nanostructure and the mechanical properties of the RPV steels, and whether these two domains are interrelated, is discussed in this thesis.

For both, LBE and flux effects, the nano-scale characterization of the irradiation-induced features is crucial for the understanding of the underlying formation mechanisms. On this basis, it can provide qualitative and quantitative insight on long-term operation behavior of the RPV steel.

It is important to recognize that the both small size and the low concentration of irradiation-induced features in RPV steels make their characterization extremely challenging. Standard techniques, such as optical microscopy or scanning-electron microscopy (SEM), are not able to resolve the nanometer-sized irradiation-induced features. In fact, no single technique by itself is able to characterize the irradiation-induced features in all aspects. For this, a combination of several techniques is required.

1.5 AIMS AND SCOPE

The present work is going to investigate two of the main issues [24] with regard to long-term irradiation of RPV steels: The so-called flux effects and the late-blooming effect. The investigations are motivated by the fact that the current knowledge of these effects is still limited. Knowledge gaps include:

- the functional form of the flux dependence of cluster size and volume fraction,
- the consequences for the mechanical properties,
- the significance and origin of the change of slope in the fluence dependence of the nanofeature characteristics and the resulting mechanical properties.

First, the issue of flux effects is going to be investigated. For this, pairs of samples of RPV steels which have been neutron irradiated to the same level of fluence, with fluxes as different as possible, are selected. The sample pairs are characterized by means of SANS and hardness tests. SANS enables the characterization of the irradiation-induced clusters in the materials. The evolution of the characteristics of the cluster population is going to be contrasted with two analytical models of cluster evolution, namely deterministic growth and coarsening. Subsequently, the nanostructure evolution is going to be linked to the changes in mechanical properties with a number of analytical hardening models. Finally, the significance of flux effects on the nanostructure and mechanical properties of the materials are elaborated.

Second, the appearance of the late-blooming effect is investigated. Typically, the irradiation damage in an RPV is expected to show a smooth, square-root like dependence on the neutron fluence. Under certain conditions, deviations from the typical smooth irradiation response may occur [24]. In the present work, two RPV steels, for

which such a discontinuous irradiation response was reported [8] in both nanostructural and mechanical properties, are investigated. This involves the characterization of additional irradiation conditions of the same materials and the compilation of supplementary information on the irradiation-induced clusters, such as the shape and the chemical composition of clusters, by means of APT. The APT and SANS data are then going to be used to evaluate several models of cluster evolution, which were reported to be the origin of a sudden increase of irradiation response.

The present thesis is organized as follows: Chapter 2 introduces the nanostructural characterization methods, namely small-angle neutron scattering and atom-probe tomography, which are applied in this work to characterize the features arising from neutron irradiation. The assumptions and concepts used for data treatment are presented.

Chapter 3 covers the materials including composition, thermal treatment, irradiation conditions and basic mechanical properties. This is followed by a description of the experimental set-ups and the parameters used for the SANS and APT experiments.

The experimental results are presented in Chapter 4, separately for flux effects (SANS) and the late-blooming effect (SANS & APT).

The first part of the discussion, Chapter 5, is dedicated to flux effects. The results on flux effects are compared with analytical models of cluster evolution and hardening. The second part addresses the late-blooming effect. The experimental findings are contrasted with data from the literature. A two-path model of cluster evolution is proposed. Furthermore, the conditions under which a late-blooming effect occurs are considered.

Chapter 6 summarizes the findings of this thesis. Conclusions are drawn.

This chapter covers a general overview of nanostructural characterisation techniques typically used for the analysis of irradiation damage in RPV steels. As the irradiation-induced defects have sizes in the nanometer range and concentrations lower than 0.1 vol.%, standard methods, such as optical microscopy and scanning electron microscopy, are not suitable. This is also the reason why usually a number of techniques are put to use, such that a more complete picture of the irradiation damage can be obtained.

In the present work, small-angle neutron scattering (SANS) and atom-probe tomography (APT) are applied for the characterisation of irradiation damage. The general overview is followed by a more detailed description of both SANS and APT.

2.1 OVERVIEW

Small-angle neutron scattering (SANS)

Small-angle neutron scattering [25, 26] is able to resolve nanometer-sized features in irradiated RPV steels. Solute clusters in a size range from 0.5 to up to 100 nm are identified through an increase in scattering intensity. Information on the size distribution of scatterers, their number density and volume fraction is obtained with an inverse transformation of the scattering pattern.

SANS is able to probe a sample volume of several tenths of mm^3 , while still resolving changes on a sub-nanometer scale. Apart from the information about the size and density of clusters, additional information about the average chemical composition of clusters is obtained.

Atom-probe tomography (APT)

Atom-probe tomography (APT) is based on field evaporation of atoms from a small sample volume of about $100 \times 100 \times 500 \text{ nm}^3$ [27, 28]. APT can resolve a three-dimensional distribution of elements within the probed sample volume. One measurement consists of the position and type of element of several tens of millions of atoms. The acquired three-dimensional dataset is analyzed for heterogeneities, such as solute clusters, utilizing cluster-detection algorithms. These yield information on the size distribution of clusters, their number density, volume fraction and chemical composition. The lower detection limit in cluster size strongly depends on the efficiency of the used detector. The APT devices used in the present work are able to resolve clusters with radii of about $> 0.4 \text{ nm}$.

Positron-annihilation spectroscopy (PAS)

In contrast to SANS and APT, positron annihilation spectroscopy (PAS) is sensitive to open-volume defects [29]. Positrons are the anti-particles of electrons and can be used to probe a material for positron affine heterogeneities, such as vacancies, dislocation loops or special types of solute clusters.

The technique is non-destructive and involves the injection of positrons into a specimen. After thermalization, diffusion and trapping, the positrons eventually annihilate with the electrons in the material [29]. An annihilation event produces two coincidentally γ -rays at an angle of approximately 180° and an energy of about 511 keV.

The presence of lattice defects, i.e. positron traps, in the irradiated material matrix modifies the outcome of the annihilation events in relation to an undamaged reference condition. By evaluating the spectrum of positron lifetimes and/or the energy spread (Doppler broadening) and angles between the emitted γ -rays, information about the type, size and concentration of the defects is obtained. PAS is an extremely sensitive technique and can resolve single-vacancy defects at very low concentrations (1 ppm). A detailed discourse on the theory and various applications of PAS are available elsewhere [29].

PAS has been used to investigate irradiation damage in model and RPV steels since the mid-1980s [30–33]. It is important to note that conventional PAS experiments on neutron-irradiated RPV steels are particularly difficult to perform and to analyze. In conventional PAS, ^{22}Na is used as positron source. The β^+ decay in the source emits a single γ quantum, which is used as a start signal for the lifetime measurement. Unfortunately, the γ -start signal overlaps with the ^{60}Co decay at 1.2 to 1.3 MeV, which occurs in neutron-irradiated RPV steels. One approach reducing the background signal from the ^{60}Co decay is to use triple coincidence measurements, which enables the filtering of the data for real annihilation events. However, triple coincidence leads to a considerable prolongation of measuring time to several days or weeks per specimen. A more advanced approach is to use Gamma-induced Positron Spectroscopy (GiPS) [34, 35]. With GiPS, the start signal for lifetime measurement is automatically known from a pulsed beam of bremsstrahlung and therefore not influenced by the ^{60}Co decay in radioactive steels. In addition, GiPS measures over the whole sample thickness, i.e. surface effects are mitigated.

Transmission electron microscopy (TEM)

Transmission electron microscopy (TEM) is a method capable of characterizing matrix damage, such as dislocation loops in RPV steels [36, 37]. The technique involves the transmission of electrons with energies of several 100 keV through a thin (30 to 100 nm) specimen. The scattered electrons give information about phase, lattice periodicity and electron densities in the sample.

2.2 SMALL-ANGLE NEUTRON SCATTERING (SANS)

2.2.1 Principles of SANS

The neutron is a subatomic particle with a mass of 1.674×10^{-27} kg. It is a spin- $1/2$ particle with a magnetic moment of $-1.041 \times 10^{-3} \mu_B$. A free neutron has a mean lifetime of 885.7 s, after which it decays into a proton, an electron and an antineutrino. Thus, its lifetime is long enough to perform scattering experiments, if a readily available neutron source is present. Currently, there are two types of neutron sources available, which yield neutron fluxes sufficient for the conduction of SANS experiments, that is, nuclear reactors and spallation sources. The former generates a continuous stream of neutrons as a product of nuclear fission, while the latter produces neutrons (typically pulsed) via the collision of high-energy protons with a target.

The following section gives an overview on the scattering of neutrons at small angles ($< 5^\circ$) and introduces the assumptions that are made during the analyses of the SANS data in the present work.

Under the assumption of a monochromatic neutron beam with a wavelength, λ , the steady state incident neutron wave is expressed as a planar wave function

$$\psi(\mathbf{x})_i = \psi_0 \exp(i\mathbf{k}_i \mathbf{x}) , \quad (2)$$

at a distance \mathbf{x} from the nucleus. The wave vector \mathbf{k}_i has a magnitude of $k_i = 2\pi/\lambda$. The scattering of a neutron on a point-like nucleus at distance \mathbf{r} gives rise to a spherical symmetrical wave function

$$\psi(\mathbf{r})_s = -\frac{b_{\text{nuc}}}{r} \psi_0 \exp(-i\mathbf{k}_s \mathbf{r}) . \quad (3)$$

The nuclear scattering length, b_{nuc} , does not depend in a systematic manner on the atomic number of the nucleus. Its value can be negative, as for Mn (-3.73 fm) and even varies between different isotopes of the same element, as for ^{54}Fe and ^{56}Fe with nuclear scattering lengths of 4.21 and 9.94 fm, respectively [38]. The non-periodicity of b_{nuc} is a major advantage of SANS over small-angle X-ray scattering (SAXS), as elements adjacent in the periodic table show a distinct difference in b_{nuc} .

Moving from the scattering on a single nucleus in Eq. (3) to the scattering on an array of n nuclei, we get

$$\Psi_s = -\sum_j^n \frac{b_j}{r} \Psi_0 \exp(i\mathbf{k}_i \mathbf{r}) \cdot \exp(i\mathbf{Q} \mathbf{r}) . \quad (4)$$

The wave vector, \mathbf{k} , changes only in direction and not in magnitude due to the elastic neutron-nuclei interaction [25]. The difference between incident wave vector, \mathbf{k}_i , and scattered wave vector, \mathbf{k}_s , defines the scattering vector, \mathbf{Q} , as illustrated in Fig. 4.

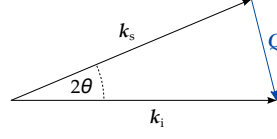


Figure 4: Geometrical relationship between the incident and scattered wave vector, k_i and k_s , respectively, and the scattering vector, Q .

The magnitude of Q is expressed in inverse length units (nm^{-1}) of the reciprocal space, given with

$$Q = \left| \frac{4\pi}{\lambda} \sin \theta \right| , \quad (5)$$

where 2θ is the scattering angle. In SANS, the intention is to observe structures larger than the interatomic distances. Therefore, the scattering angle is chosen to be smaller than about 5° to avoid the observation of high-intensity Bragg peaks.

It is interesting to note that Eq. (5), when combined with Bragg's law, gives an estimate of the necessary Q range that needs to be measured to observe scatterers of radii, R :

$$Q = \frac{\pi}{R} \quad \text{or, vice-versa} \quad R = \frac{\pi}{Q} . \quad (6)$$

As a rule of thumb, the highest scattering vector Q_{max} needs to be about 3.1 nm^{-1} to resolve structures of radii of about $R = 1 \text{ nm}$.

The differential cross section over a solid angle, Ω , for an array of n nuclei is written as

$$\frac{d\sigma}{d\Omega}(\mathbf{Q}) = \frac{1}{n} \left| \sum_j^n b_j \cdot \exp(i\mathbf{Q}\mathbf{r}_j) \right|^2 . \quad (7)$$

If the sum over n atoms is replaced by the integral over the scattering-length density, $\eta(\mathbf{r}) = \sum b_i / V_{i,\text{at}}$, Eq. (7) becomes the macroscopic cross section

$$\frac{d\Sigma}{d\Omega}(\mathbf{Q}) = \frac{n}{V_{\text{tot}}} \frac{d\sigma}{d\Omega}(\mathbf{Q}) = \frac{1}{V_{\text{tot}}} \left| \int_V \eta(\mathbf{r}) \cdot \exp(i\mathbf{Q}\mathbf{r}) d\mathbf{r} \right|^2 , \quad (8)$$

which is normalized by the total sample volume, V_{tot} . Only deviations, $\Delta\eta(\mathbf{r})$, from the average scattering-length density, $\bar{\eta}$, contribute to the scattering intensity. With $\eta(\mathbf{r}) = \Delta\eta(\mathbf{r}) + \bar{\eta}$, it follows that

$$\frac{d\Sigma}{d\Omega}(\mathbf{Q}) = \frac{1}{V_{\text{tot}}} \left| \int_{V_1} \Delta\eta(\mathbf{r}) \exp(i\mathbf{Q}\mathbf{r}) d\mathbf{r} \right|^2 . \quad (9)$$

From Eq. (9), we can see that the intensity of the signal that is measured in SANS is ultimately a consequence of heterogeneities in the scattering-length density, $\Delta\eta$, in the sample volume. Moreover, the integral term is equivalent to the Fourier transform of the spatial arrangement of these heterogeneities. Unfortunately, by measuring $d\Sigma/d\Omega$, the phase information gets lost in the scattering-cross section due to the square of the Fourier transform. Therefore, it is not possible to simply perform an inverse Fourier transform of the measured cross section $d\Sigma/d\Omega$ to retrieve information about the spatial distribution of $\eta(\mathbf{r})$.

For a two-phase system, the scattering-length density becomes independent of \mathbf{r} , such that $\Delta\eta^2 = (\eta_1 - \eta_2)^2$ and

$$\frac{d\Sigma}{d\Omega}(\mathbf{Q}) = \frac{1}{V_{\text{tot}}}\Delta\eta^2 \left| \int_{V_1} \exp(i\mathbf{Q}\mathbf{r}) d\mathbf{r} \right|^2. \quad (10)$$

For scatterers of identical shape, Eq. (10) is represented as

$$\frac{d\Sigma}{d\Omega}(\mathbf{Q}) = \Delta\eta^2 NV^2(R) \cdot F(\mathbf{Q}, R) \cdot S(\mathbf{Q}, R), \quad (11)$$

where $N = \nu/V_{\text{tot}}$ is the number density of scatters and ν is the number of scatterers. The structure factor, S , is related to the pair-correlation function and contains information about interference between singular scatterers. For the case of a dilute system, which is adequate for the materials investigated in this work, S becomes equal to one.

The form factor, F , relates to the shape of the scatterers. Analytical expressions for F are available for many different shapes, such as spheres and ellipsoids. For the purpose of the present work, a spherical form factor for the scatterers is appropriate. A single sphere of radius R shows a scattering pattern

$$F(\mathbf{Q}, R)_{\text{sph}} = \left[\frac{3(\sin(QR) - QR \cos(QR))}{(QR)^3} \right]^2. \quad (12)$$

The interference pattern of a single sphere of radius R is shown in Fig. 5 as a function of dimensionless QR . The limits of the curve can be approximated for both large and small QR . The region for $QR < 1$ is described with the Guinier approximation $F \propto \exp(Q^2 R_{\text{gyr}}^2/3)$, where $R_{\text{gyr}} = \sqrt{5/3}R$ is the radius of gyration for a sphere with radius R . This relation is utilized to get a first estimate of the radius of the scatterers by fitting a straight line to the representation $\log(F)$ vs. Q^2 and considering the slope $m = -R_{\text{gyr}}/3$. However, this estimate is ambiguous if the scatterers are not monodisperse, but show a distribution of different sizes in the material [39].

For large QR values, in the so-called Porod regime, F shows a dependence $\propto (QR)^{-4}$. The exponent of -4 holds true not only for spherical scatterers, but for arbitrary form factors, as long as the interface between matrix and scatterers is flat. The surface of scatterers is a factor of proportionality in this relation.

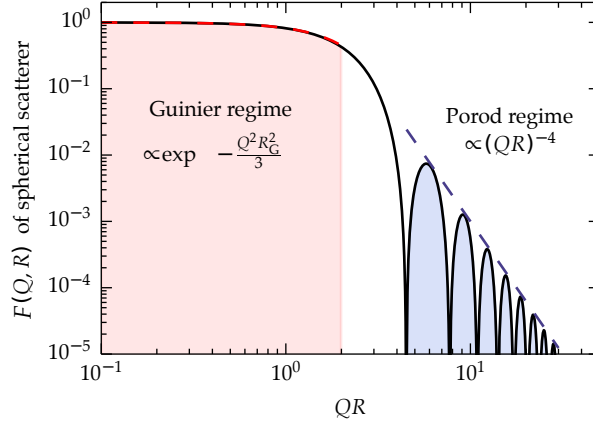


Figure 5: Form factor of a spherical scatterer with radius $R = 1$ nm as a function of QR . The Guinier region and the Porod region are highlighted.

The preceding considerations on neutron scattering are related to nuclear scattering. Similarly, incident neutrons also interact with the magnetic moment of atoms with unpaired electron spins. This magnetic interaction is independent of the nuclear one and it is characterized by its magnetic scattering length given with

$$b_{\text{mag}} = \mu \frac{\gamma r_e}{2} = \mu \cdot 2.7 \text{ fm} , \quad (13)$$

where μ is the magnetic moment of the scatterer, $\gamma = 1.913$ the gyromagnetic factor of the neutron in units of the Bohr magneton, $\mu_B = 5.788 \cdot 10^{-5} \text{ eV} \cdot \text{T}^{-1}$, and $r_e = 2.818 \text{ fm}$ is the classical electron radius.

According to Eq. (13), the magnetic scattering length of Fe is $b_{\text{mag}} = 6.0 \text{ fm}$ [40]. Under the assumption that the scatterers (index s) are coherent with the Fe matrix (index m) and can be treated as non-magnetic [16] ($b_s = 0 \text{ fm}$), the magnetic scattering contrast is written as

$$\Delta\eta_{\text{mag}}^2 = \frac{4}{a^6} (b_s - b_m)^2 = 2.598 \cdot 10^{-7} \text{ nm}^{-4} , \quad (14)$$

where the lattice parameter of bcc Fe is $a = 0.2866 \text{ nm}$.

The existence of both nuclear and magnetic scattering enables to retrieve information about the chemical composition of scatterers. To separate the contributions of nuclear and magnetic scattering-cross section, the sample under investigation is placed in a saturating magnetic field.

The A ratio is defined [16] as the ratio of scattering-cross section perpendicular (\perp) and parallel (\parallel) to the magnetic field applied to the sample, such that

$$A = \frac{d\Sigma_{\perp}}{d\Omega} \Big/ \frac{d\Sigma_{\parallel}}{d\Omega} = \left(\frac{d\Sigma_{\text{nuc}}}{d\Omega} + \frac{d\Sigma_{\text{mag}}}{d\Omega} \right) \Big/ \frac{d\Sigma_{\text{nuc}}}{d\Omega} . \quad (15)$$

A specific chemical composition of clusters results in a specific value of the A ratio. The A ratios of clusters embedded in a Fe matrix are, for example, for pure Cu clusters and MnNiSi of equal proportions 13.0 and 1.9, respectively. However, it is not possible to directly calculate the cluster composition from a measured A ratio, as many compositions can have the same A ratio. Rather, the measured A ratios are used to cross check with cluster compositions from model assumptions or other characterization techniques.

In real systems, the total differential scattering-cross section does not only show a Q dependent, coherent scattering contribution but also contains a Q independent, incoherent contribution:

$$\frac{d\Sigma}{d\Omega}(\mathbf{Q}) = \frac{d\Sigma_{\text{coh}}}{d\Omega}(\mathbf{Q}) + \frac{d\Sigma_{\text{inc}}}{d\Omega}. \quad (16)$$

The incoherent scattering does not carry any structural information on the distribution of scatterers in the system. It stems from both the random distribution of isotopes in the material and from features with sizes below the resolution limit of SANS of about $R_{\text{min}} = 0.5$ nm. For the present purpose, the contribution of $d\Sigma_{\text{inc}}/d\Omega$ is considered to be an offset in the signal, which is to be subtracted prior to further data treatment. The magnitude of the incoherent scattering is estimated by performing a linear fit in the Porod representation ($d\Sigma/d\Omega$ vs. Q^4).

Unlike in many biological systems, where scattering structures are often equal in size, the features present in irradiated RPV steels are polydisperse. In our model, this is accounted for by the number-density size distribution, N_R , defined as

$$N = \int N_R(R) dR. \quad (17)$$

Inserting Eq. (17) in the expression of the scattering-cross section of a monodisperse system, Eq. (11) and assuming a dilute system of scatterers ($S = 1$), results in the scattering function of polydisperse spheres

$$\frac{d\Sigma}{d\Omega}(\mathbf{Q}) = \Delta\eta^2 \int N_R(R) \cdot V_{\text{sph}}^2(R) \cdot F_{\text{sph}}(\mathbf{Q}, R) dR \quad (18)$$

$$= 12\pi \cdot \Delta\eta^2 \int N_R(R) \cdot R^6 \cdot \left[\frac{\sin(\mathbf{Q}R) - \mathbf{Q}R \cos(\mathbf{Q}R)}{(\mathbf{Q}R)^3} \right]^2 dR, \quad (19)$$

where $V_{\text{sph}}(R)$ is the volume of a sphere with radius R . The transformation of Eq. (19) to the size domain is the inverse problem to be solved in SANS data treatment. Finding the inverse yields several characteristics of the cluster population that we are interested in:

$$\text{Number density: } N = \int N_R(R) \, dR \quad (20)$$

$$\text{Volume fraction: } f_v = \int f_R(R) \, dR = \int N_R(R) \cdot V_{\text{sph}}(R) \, dR \quad (21)$$

$$\text{Mean radius: } \bar{R} = \frac{\int R \cdot N_R(R) \, dR}{\int N_R(R) \, dR} \quad (22)$$

It is important to note that both N and f_v are calculated under the assumption that the scattering contrast, $\Delta\eta^2$, is a known quantity.

2.2.2 Transformation to size domain

The solution to the inverse problem of retrieving the size distribution of clusters from the SANS scattering curve is underdetermined due to the loss of phase information in $d\Sigma/d\Omega$ and the limited Q range observed during a real experiment. There are several approaches available in the literature for transforming the measured scattering-cross sections to the size domain. However, different algorithms may yield different fits to the experimental values in the Q domain and consequently in the calculated characteristics of the cluster population.

- The simplest approach is to fix the type of size distribution to an analytical expression. The parameters of an analytical function, such as the position of the center peak and the width are then fitted via a common least-squares algorithm. Suitable distributions that have been applied to the characterization of irradiation-induced clusters in RPV steels are e.g. the Gaussian, the log-normal or the gamma distribution [41]. Obviously, the downside of this approach is that the type of distribution has to be known prior to the data analysis to yield reasonable results.
- In the maximum entropy (ME) method, e.g. [42–44], the size distribution is discretized in size classes. This method has been successfully applied for the analysis of irradiated RPV steels. Classical ME algorithms, however, suffer from lack convergence in some cases [45].
- The Indirect Fourier Transformation (IFT) [46–49] involves the modeling of $N_R(R)$ with a linear combination of a fixed number, ϵ , of cubic B-splines. Each spline covers a specific range of R . To avoid oscillating results in the size domain, the base of each spline is linked with a Lagrange parameter, λ_p , for dampening.

The IFT is a powerful technique for the determination of the characteristics of the cluster population and has been successfully applied in many cases [8, 13, 50, 51] for the analysis of irradiated RPV steels. One advantage of the IFT over direct techniques is that the shape of the size distribution is not bound by pre-defined functions. It is, however, important to note that IFT requires the user to set several parameters during the analysis, such as λ_p and ϵ . Although there

are guidelines [25] on how to select a proper set of parameters, the choice of parameters ultimately depend on the user's preferences [52]. This might lead to results which are difficult to reproduce. This is particularly relevant for the case of the integrated cluster properties \bar{R} and N .

Furthermore, oscillating solutions in the size domain may lead to partly negative, i.e. unphysical, size distributions.

- In the present work, the transformation of the scattering curves to the size domain was performed by means of a self-written Monte Carlo fitting (MCF) routine. The algorithm is based on a method introduced by Martelli et al. [53]. Similarly to IFT and ME methods, the MCF algorithm involves no prior selection of the type or shape of the size distribution. Within the present work, the original algorithm was reproduced and extended for correct scaling of N_R , a better convergence of the fitting process for small clusters ($R < 1$ nm) and estimations on the robustness of the parameters of the cluster population. The steps of the MCF algorithm are introduced below.

The aim is to retrieve the size distribution of scatterers $N_R(R)$ from the measured scattering-cross section based on the considerations in Eqs. (18) and (20). The MCF algorithm requires the values of the scattering intensity $I(Q_i)$ and the number density distribution, $N_R(R_j)$ to be in discrete form. The measured scattering intensity $I_{\text{exp}}(Q_i)$ is already in the proper shape as it is discretized during the raw-data treatment. The size distribution in Eq. (17) is now discretized in a similar manner. We write the simulated scattering curve

$$I_{\text{sim}}(Q_i) = \kappa \cdot \Delta\eta^2 \cdot \sum_{R_j=R_{\min}}^{R_{\max}} N_R(R_j) \cdot R_j^6 \cdot F_{\text{sph}}(Q_i, R_j) \cdot \Delta R, \quad (23)$$

where the constants are grouped in the parameter κ . The cluster radius R_j ranges from R_{\min} to R_{\max} in steps of ΔR . The boundaries of R_j can either be set automatically with the Q range acquired experimentally (see Eq. (6)), or chosen manually.

At start, the number-density size distribution is empty, $\sum N_R = 0$. For the first iteration, a value R_j is chosen from a uniformly random pool of radii ranging from R_{\min} to R_{\max} . The chosen R_j value is added to N_R . An intermediate scattering intensity $I_{\text{tmp}}(Q_i)$ is calculated according to Eq. (23). As we are in the first iteration, the resulting scattering intensity has a Q dependence equal to the form factor of a single sphere, F_{sph} , plotted in Fig. 5. The intermediate scattering intensity, I_{tmp} , is then fitted to the experimental scattering curve, I_{exp} , by varying the scaling of N by means of a least-squares minimization:

$$\chi_{\min}^2 = \min \left(\sum_i \left[\frac{I_{\text{exp}}(Q_i) - I_{\text{tmp}}(N, Q_i)}{w(Q_i)} \right]^2 \right), \quad (24)$$

where the weights, $w(Q_i)$, of each data point are calculated from the inverse of the experimental uncertainty, I_{err} . The value for $\chi_{\min(1)}^2$ of the first iteration is saved for later comparison.

The next iteration adds another randomly chosen R_j to the size distribution N_R and a new scattering intensity I_{tmp} is calculated and minimized according to Eq. (24). If the new I_{tmp} results in a lower χ^2 than the one from the old I_{sim} , i.e. $\chi_{\text{min}(2)}^2 < \chi_{\text{min}(1)}^2$, the added radius R_j is kept in N_R and I_{tmp} becomes the new I_{sim} . Otherwise, I_{tmp} is rejected, and a new R_j trial is initiated.

At first, the initial procedure is performed for 100 randomly chosen R_j values. It is then checked if the minimization routine is trapped in a local minimum, i.e. no further R_j s are accepted. In this case, all variables are reset, and the algorithm is restarted with a new random seed. If the initial procedure is not trapped in a local minimum, more R_j s are added until convergence is reached. For the present cases, this involves about $2 \cdot 10^6$ trials of randomly chosen R_j s and corresponding minimizations.

The whole procedure is performed for at least ten times with a different pool of uniformly distributed random numbers R_j . For each run, the number-weighted and volume-weighted cluster size distributions are calculated and the integrated parameters, N , f_v and \bar{R} are determined in accordance with Eqs. (20) to (22).

Finally, the arithmetic mean and uncertainty of the parameters are calculated. The estimated uncertainties of the parameters correspond to the 3σ standard deviation of the results from each run.

Clearly, the calculated uncertainties are not the real experimental uncertainties. These would also include systematic errors from calibration and material heterogeneities. Due to the random starting conditions of each MCF run, the uncertainty rather corresponds to an estimate on how stable the used model, i.e. dilute, poly-disperse spherical scatterers with radii between R_{min} and R_{max} , is reproduced by the fit. This kind of error estimate is more conclusive than the standard uncertainty estimations based the covariance matrix of the least-squares fit.

The advantages of the established MCF procedure are summarized below:

- The calculated size distributions, N_R and f_R , are always ≥ 0 , i.e. yield physically meaningful results. This is given by how the algorithm operates [53]. In contrast, the IFT algorithm can lead to partly negative, non-physical size distributions.
- There are no fitting parameters to be set by the user. The parameters that *can* be altered (R_{min} , R_{max} , ΔR) may be left fixed for most cases. In fact, the scattering curves of the materials investigated in the present work were all transformed to the size domain with the same set of fitting parameters. This advantage was also put to use for the SANS analyses of different classes of materials, such as oxid-dispersion strengthened steels [54].
- The uncertainties of the integrated properties of the cluster distribution (N , f_v and \bar{R}) give a meaningful estimate of the stability and reproducibility of the fit. For the present case of irradiated RPV steels, this is particularly important for the development of models of cluster evolution, as outliers are recognized and treated accordingly by the error-weighted fitting procedure.

- One particular challenge of the analyses of the RPV materials investigated in the present work is the extremely small size of the clusters, which, for some materials are on the edge of the observable radii. According to simulated size distributions [55] and the analyses performed in the present work, the results from the MCF algorithm are more stable for the smallest clusters in the vicinity of the SANS resolution limit ($R \approx 0.5 \dots 0.8$ nm) than typically applied methods [48].

2.3 ATOM-PROBE TOMOGRAPHY (APT)

2.3.1 Principles of APT

Atom-probe tomography is a nanostructural analysis technique that delivers a three-dimensional distribution of chemical elements within sample volume with near-atomic resolution. A comprehensive introduction to the technique can be found in the books of Miller [27] and Gault [28].

APT is a destructive technique that uses field evaporation to successively remove ions from the tip of a needle-shaped specimen. The experimental set-up of an APT device is schematically depicted in Fig. 6. The working principle is the following: Ions released from the surface of the sample tip are accelerated in an electric field. A time-of-flight (TOF) mass spectrometer is used to determine the mass-to-charge ratio of the ions. The impact positions of the ions are recorded on a two-dimensional detector. By timing each ion-evaporation event and combining the mass spectrometer with a position-sensitive ion detector, it is possible to reconstruct a three-dimensional map of the chemical composition of the sample at near-atomic scale.

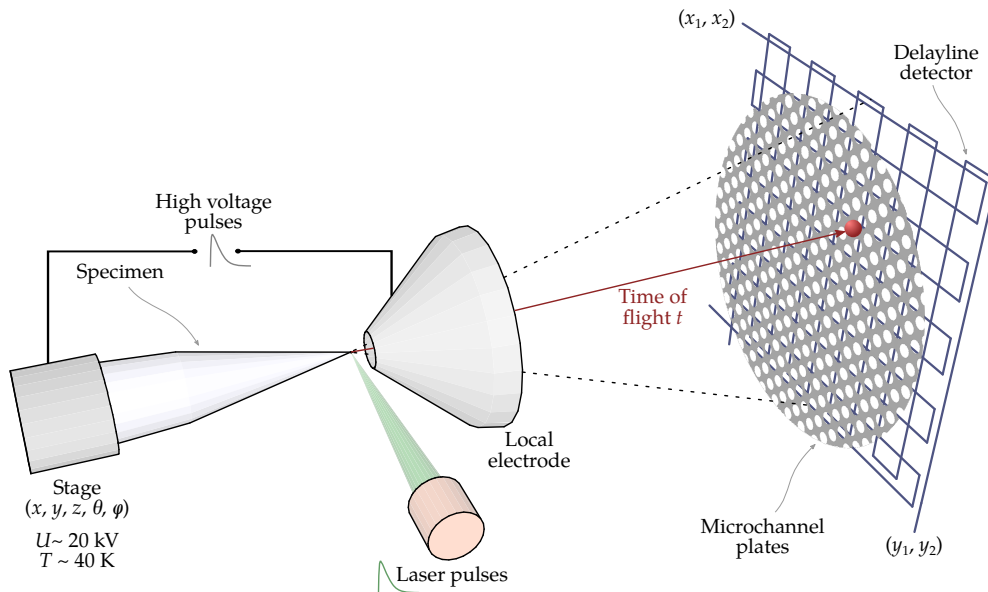


Figure 6: Basic set-up of an APT device. Ions are field evaporated from the tip surface. The time-of-flight and the impact position of the ions are recorded on the two-dimensional detector.

The sample is kept in an ultrahigh vacuum chamber at a pressure of about 10^{-10} mbar and a temperature of about 40 K. A positive standing voltage $U_0 \approx 20$ kV is applied to the specimen, which is just below the ionization threshold. To make

field evaporation possible at reasonable voltages, the radius of the sample tip, R_{tip} , needs to be < 70 nm. The electric field at the apex of the sample tip is given with

$$E = \frac{U_0}{\beta R_{\text{tip}}}, \quad (25)$$

where β is a geometry factor, which depends on the shape of the tip and its electrostatic environment. For a perfect sphere, β would be equal to 1, for a real tip shape, the value is between 2 and 8 [27]. An additional high-frequency pulsed voltage $U_{\sim} \approx 0.2 \cdot U_0$ is applied to the specimen, to trigger field evaporation at a known point in time, t_0 . This value is recorded and used as the start time for the TOF measurement of the ion hitting the detector at a distance L .

The electric field penetrates only fractions of atomic radii into the material. Therefore, only atoms at the surface of the tip are ionized and escape the material matrix. As the atoms have to be evaporated in a controlled way, the actual evaporation rate, $k(t)$, is time dependent and only increased for short timed pulses in the order of several ps. The Arrhenius-type equation of the evaporation rate is given by

$$k(t) = \nu \cdot \exp\left(\frac{-Q_{\text{act}}(E(t))}{k_b T(t)}\right), \quad (26)$$

where Q_{act} is the activation energy for field evaporation, T and ν are the temperature and the vibration frequency of the atoms at the tip surface, respectively. Considering ν as constant, Eq. (26) states that a pulsed increase of the evaporation rate can either be achieved by an increase of the electric field $E(t)$ or of the temperature $T(t)$. This means that there are in fact two ways to evaporate ions in a pulsed way: Either by electric mode, i.e. applying an additional pulsed voltage to the tip, or by laser mode, i.e. illuminating the tip surface with a pulsed laser and increasing the temperature. Both methods were applied in the present work for all conditions, i.e. the non-irradiated, the medium-fluence and the high-fluence samples. Fig. 6 shows both methods, voltage pulses and laser pulses, at the same time for illustration purposes.

The impacting ions are registered at the detector. The difference between start time, t_0 , which coincides with the pulse and stop time, t_{hit} , at detector hit is the time of flight, t , for each event. With this, the mass-over-charge ratio

$$\frac{m}{n} = 2e (U_0 + U_p) \cdot \left(\frac{t}{L}\right)^2 \quad (27)$$

is calculated for each detector event. The ion charge state $n \in (1^+, 2^+, \dots)$ has to be selected manually later in data treatment, whereas the standing voltage, U_0 , and pulsed voltage, U_{\sim} , are known quantities, as is the flight length, L , after calibration. In data treatment, the recorded data is then represented as a mass-over-charge histogram. For steels, the mass resolution is typically given at the 10 % width $M/\Delta M_{10\%}$ of the main $^{56}\text{Fe}^{++}$ peak. The mass resolution of both electric and laser atom probe is

sufficient to separate isotopes of individual elements. A significant improvement of the mass resolution is achieved by extending the sample-detector distance, L . However, this decreases the field of view of the detector and leads to smaller visible measuring volumes. For voltage-pulsed atom probes, an additional improvement of the mass resolution is achieved by making use of an ion-reflectron lens [28], which compensates for deviations in the ion velocity.

The impact position of the ion on the detector is determined by means of an amplifying micro channel plate (MCP) and an advanced delay-line detector (aDLD). The ion impact creates an electron cascade in the MCP, which is then registered as an electric pulse by the aDLD. The latter consist of two Cu wires rotated 90° to each other, as shown in Fig. 6. The time differences in the signal delay measured at the wires are used to calculate the two-dimensional position, (x, y) , of the impact on the detector.

The original coordinates of the ion on the tip surface (x', y') are calculated with the coordinates (x, y) on the detector and an inverse projection. The image magnification, G , is given by

$$G = \frac{L}{(m+1)R_{\text{tip}}} \quad . \quad (28)$$

The image-compression factor, m , is linked to the projection point, P , as shown in Fig. 7.

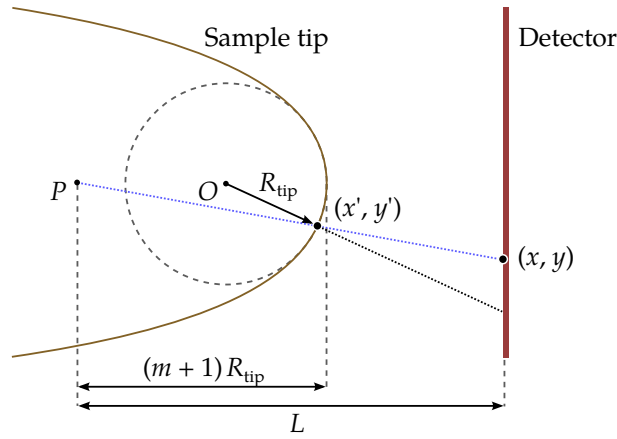


Figure 7: Geometric relations for the image compression factor G . The connection $P \rightarrow (x', y')$ shows a compressed projection on the detector compared to the radial connection $O \rightarrow (x', y')$.

According to Eq. (25), the tip radius is determined by the expression

$$R_{\text{tip}} = \frac{U}{E\beta} \quad . \quad (29)$$

When the magnification, G , is determined, the position of the ion in the specimen, (x', y') , can be calculated by the simple relation

$$(x', y') = \frac{(x, y)}{G} . \quad (30)$$

The tip of the sample evaporates atom by atom and layer by layer. As this process shortens the sample, the depth position, Δz , is obtained by adding up the increments of the number of ions, Δn , evaporated:

$$\Delta z = \frac{\Delta n V_{\text{at}}}{Q_{\text{eff}} d^2} \cdot G^2 , \quad (31)$$

where V_{at} is the volume of each atom in the lattice structure, Q_{eff} is the detection efficiency and d the detector size. The detector efficiency of the atom probe devices used in this work is in the range of 0.50 to 0.65. This is due to inter-channel regions of the MCP, where no electron cascade occurs. It is important to note that the loss of ions is a random process and that this effect does not introduce a bias for the composition measurement.

The reconstruction parameters, $E\beta$ and $(m + 1)$, are adjusted for each specimen to match the interplanar spacing, d , for bcc Fe. For the case of $(h, k, l) = (1, 1, 0)$ the spacing between atomic planes is

$$d_{(1,1,0)} = \frac{0.2866 \text{ nm}}{\sqrt{1^2 + 1^2 + 0^2}} = 0.2027 \text{ nm} . \quad (32)$$

Typical starting points for the reconstruction of Fe based alloys are $E\beta = 19 \text{ V/nm}$ and $(m + 1) = 1.5$ for laser pulsed samples. Fig. 8a shows a view from the top of a 3D reconstruction. A triangular region, highlighted in red, shows a lower atomic density in the lattice. This is the pole region. Upon magnification of this low-density region, atomic planes become visible, as shown Fig. 8b. The 3D reconstruction parameters are adjusted to match the measured lattice distance according to Eq. (32) for proper scaling of the reconstructed volume.

2.3.2 Data treatment

MASS SPECTRUM: The data of the TOF mass spectrum is represented as a mass-over-charge ratio, m/n , according to Eq. (27). The mass spectrum is calculated from the histogram of the m/n data. A complete spectrum covers a range of about 1 to 100 atomic mass units (amu). Fig. 9 shows a magnified view of a mass spectrum acquired from an RPV steel sample, which was measured with the ECoWaTAP device.

The intervals surrounding each peaks are manually set by the user and the corresponding isotopes and charge states, n , are assigned to the peaks. The background signal, indicated by the gray line in Fig. 9, is determined by linear fitting between the anchor points of each mass interval and removed by subtracting the fitted line.

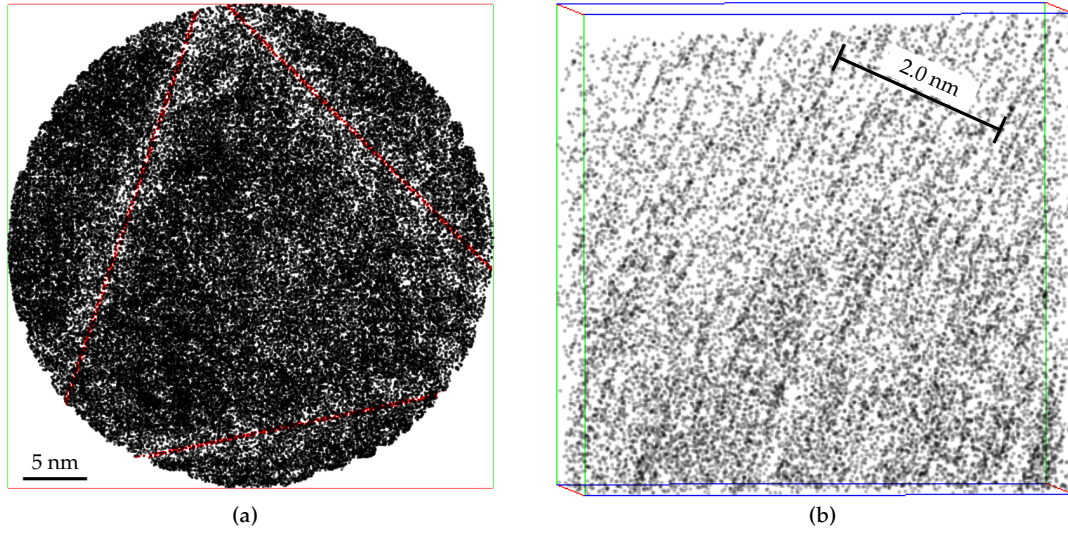
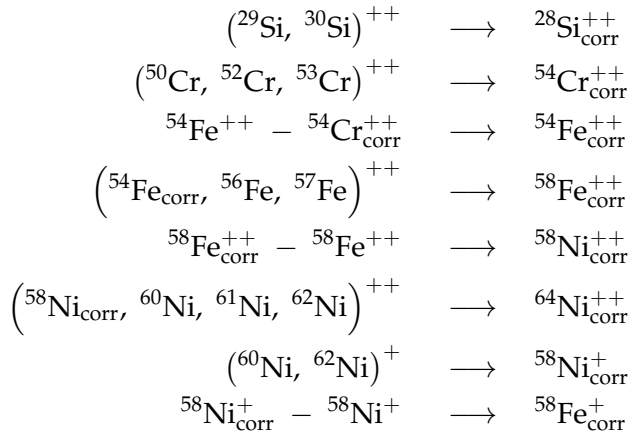


Figure 8: (a) Top view of a 3D reconstruction. The black dots represent Fe atoms. A triangular region shows a lower atomic density in the lattice due to a pole. (b) This pole region is shown in a magnified view. Ten atomic planes were used to estimate the plane distance, d .

For several cases, it is not possible to unambiguously assign a specific isotope or element to a peak since two or more species happen to share the same interval of mass-over-charge ratio. The convolution of peaks from different species is corrected via a natural abundance calculation of each element and isotope. For the case of RPV steels, the number of atoms for the following intervals are corrected with lever rules of the natural isotopic abundances:



The corrected number of atoms, X_{corr} , is used for the calculation of the chemical composition. Finally, the concentration, C , of an element, X , in atomic percent is given by

$$C_X = \frac{n_X}{n_{\text{tot}}}, \quad (33)$$

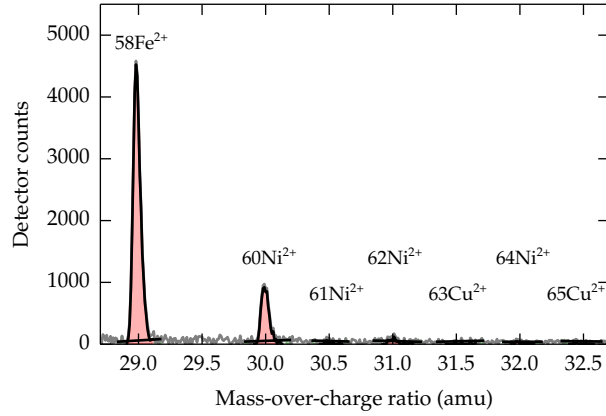


Figure 9: Magnified view of a TOF mass spectrum. The red highlighted areas denote detector hits assigned to a specific chemical element. Linear fits between the anchor points of intervals are used for background determination.

where n_X and n_{tot} are the number of atoms of the element, X , and the total atom number, respectively, in the selected volume. The uncertainty of the concentration is estimated by simple Poisson statistics and given with

$$\Delta C_X = 2\sqrt{\frac{C_X(1 - C_X)}{n_{\text{tot}}}}. \quad (34)$$

CLUSTER IDENTIFICATION: A complete 3D reconstruction of a sample volume consists of tens of millions of atoms. It is, therefore, necessary to apply automated algorithms for the quantitative analysis of an acquired data set. A variety of algorithms are available for the cluster detection. In the present work, the iso-concentration algorithm [23] is used to identify regions of increased solute concentration, i.e. solute clusters. The working principles of the algorithm are schematically shown in a 2D illustration in Fig. 10. In a first step, elements, X_i , that are considered to be the main constituents of clusters, such as Cu, Ni, etc. are unified such that

$$\text{CL} = \bigcup_i X_i. \quad (35)$$

In Fig. 10a, the distribution of cluster elements, CL, is indicated by the white circles. The sample volume is then divided into sub-volumes of equal size, Fig. 10b, and the concentration, C_{CL} , of the cluster elements is calculated in each segment according to Eq. (33). In the following step, Fig. 10c, the concentration in the sub-volumes is tri-linearly interpolated, in such a way that the interpolated concentration can be calculated for any position, (x, y, z) , in the volume. This way, an interpolated concentration value is assigned to each atom at the position $C_{\text{CL}}^{(x,y,z)}$.

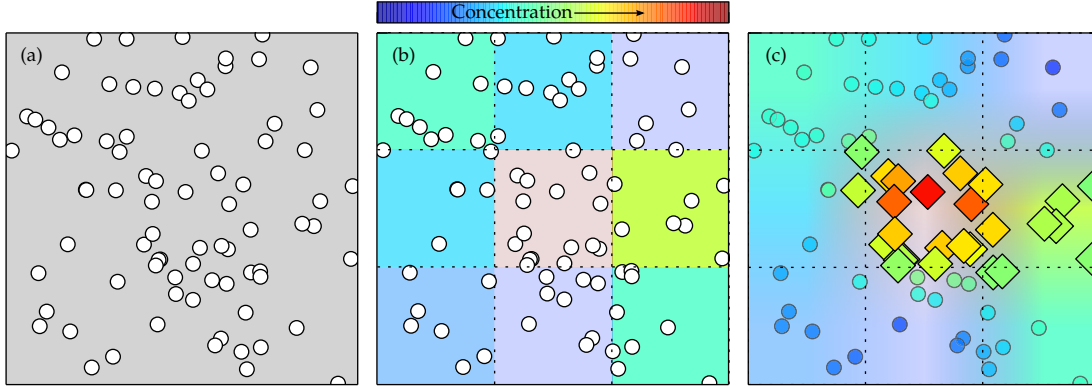


Figure 10: 2D illustration of the iso-concentration algorithm: (a) Atoms from the cluster elements (Cu, Ni, etc.) are selected (\circ symbols). (b) The area is subdivided with an equidistant grid, and the concentration of atoms is calculated in each subsection. (c) The concentration values are tri-linearly interpolated and assigned to each atom at position (x, y, z) . A minimum concentration threshold is chosen by the user. Only atoms with an assigned concentration value higher than the threshold are considered to belong to a cluster (\diamond symbols).

The group of cluster atoms, CL, is then filtered by setting a minimum concentration threshold value, C_{CL}^{\min} . This parameter is set by the user. Each atom that fulfills the relation

$$C_{CL}^{(x,y,z)} > C_{CL}^{\min} \quad (36)$$

is considered to be an atom belonging to a cluster, indicated by the \diamond shaped symbols in Fig. 10c. The atoms with lower concentrations belong to the matrix. The final step involves segmenting the group of cluster atoms into individual clusters. This is performed by checking the distance between each cluster atom: If the distance between two cluster atoms, d , is smaller than the maximum separation distance, d_{\max} , the two atoms considered belong to one cluster. Finally, clusters that contain less atoms than a minimum threshold, n_{\min} , are removed from the group of clusters and assigned to be matrix atoms. The parameters d_{\max} and n_{\min} are also to be set by the user.

The radius of gyration of a cluster is calculated according to

$$R_{\text{gyr}} = \sqrt{\frac{1}{n} \sum_{i=1}^n (x_i - \bar{x})^2 + (y_i - \bar{y})^2 + (z_i - \bar{z})^2}, \quad (37)$$

where $(\bar{x}, \bar{y}, \bar{z})$ is the center of mass of the cluster. The corresponding sphere radius, R , which corresponds to the radii given by SANS, is calculated with $R = \sqrt{3/5} \cdot R_{\text{gyr}}$.

The average parameters of the cluster population are calculated according to the following relations:

$$\text{Number density: } N = \frac{N_{\text{CL}} Q_{\text{eff}}}{N_{\text{at}} V_{\text{at}}}, \quad (38)$$

$$\text{Volume fraction: } f_v = \frac{N_{\text{at}(\text{CL})}}{N_{\text{at}}}, \quad (39)$$

$$\text{Mean radius: } \bar{R} = \sum_j^{N_{\text{CL}}} \frac{R_j}{N_{\text{CL}}}. \quad (40)$$

N_{CL} is the number of clusters, N_{at} the total number of atoms and $N_{\text{at}(\text{CL})}$ the number of atoms in clusters in the sample volume. Clusters on the edge of the volume are counted as half for the number density calculation and ignored for the calculation of the mean radius and composition to avoid bias.

EXPERIMENTS

3.1 MATERIALS

The materials investigated in the present work are base and weld metals representative of German and European RPV steels. The investigations focus on long-term irradiation effects. Performing neutron irradiation just for the purpose of this work is not feasible mainly because of long irradiation times of about one to ten years for the low-flux irradiation. Therefore, archive material from national and European research projects is studied.

The model steels JPB and JPC originate from an IAEA coordinated research program (CRP) [56] on RPV embrittlement. This program was initiated in the mid-1980s to investigate the influence of chemical composition on irradiation-induced embrittlement. Both materials are low-Cu steels and differ mainly in the residual P content in the bulk. The fabrication was performed by Nippon Steel Corporation (Japan) according to the ASTM standard A533 Type B Class 1. For this, pure iron plates were smelted in a laboratory electric furnace and the weight percent of residual elements according to the desired target levels was added. The resulting ingots were then hot-rolled into 30 mm thick plates. Subsequently, the plates were heat treated and cut into impact test samples of dimensions of $10 \times 10 \times 55 \text{ mm}^3$. The nanostructural investigations presented in this work were then initiated within the European LONGLIFE project [57, 58] for materials and irradiation conditions, which showed indications of special long-term irradiation effects [8].

The base metal GBC, as well as the welds GWC and GWD are provided by Areva GmbH and originate from the national projects CARISMA [59] and CARINA [60]. Both projects were focused on the investigation of irradiation-induced changes of the mechanical properties. The materials in this set are representative of modern Western-type RPV steels. However, material GWD has an artificially raised Cu-impurity level of about 0.2 wt.%.

The base metal BBA is not associated with a specific project. The material originates from a Belgian surveillance program. It is included in this work to contribute to investigations on flux effects.

The weld FWA was provided by VTT Espoo (Finland) within the European LONGLIFE project. The material originates from a surveillance program of a VVER-440-type reactor. It is also selected for the study of flux effects.

3.1.1 *Chemical composition*

The composition of the materials is given in Table 1 in wt.%. Some of the analyses referenced in Table 1 were conducted within the preceding projects mentioned above.

In addition, further in-house measurements are performed on the SANS specimens after completion of the SANS and hardness experiments. The in-house analyses are performed by means of inductively coupled plasma-mass spectrometry (ICP-MS) according to DIN EN ISO 17294-2. The accuracy of this method is given as about 10 %. Chemical heterogeneities within different specimens of the same material can have an impact on the irradiation response of the material. In order to study this effect, each data set available for a given material is listed here.

Table 1: Chemical composition of the materials investigated. The element content is given in wt.%. Fe in balance. The uncertainty of the in-house measurements given with about 10 %.

Material	Analysis	Mn	Ni	Si	P	Cu	Mo	V	Cr	Co	Al
JPB	in-house	1.445	0.880	0.260	0.015	0.015	0.575	0.000	0.191	0.003	0.020
JPB	[61]	1.30	0.74	0.24	0.020	0.030	0.57	0.009	0.17	n/a	n/a
JPB	[8, 56]	1.42	0.83	0.26	0.017	0.010	0.54	0.010	0.15	n/a	n/a
JPC	in-house	1.416	0.849	0.279	0.004	0.010	0.558	0.000	0.152	0.003	0.023
JPC	[61]	1.32	0.73	0.24	0.005	0.030	0.55	0.006	0.16	n/a	n/a
JPC	[8, 56]	1.45	0.81	0.27	0.007	0.010	0.54	0.010	0.15	n/a	n/a
GBC-u	in-house	0.876	1.062	0.150	0.003	0.083	0.619	0.001	0.429	0.015	0.019
GBC-hf	in-house	0.894	1.052	0.167	0.002	0.084	0.623	0.001	0.436	0.015	0.018
GBC-lf	in-house	1.132	0.752	0.164	0.002	0.086	0.629	0.001	0.428	0.016	0.017
GBC	[62]	0.81	0.96	0.15	0.006	0.090	0.53	<0.01	0.40	0.016	0.016
GWC-u	in-house	1.436	0.061	0.375	0.012	0.021	0.445	0.014	0.029	0.019	0.001
GWC-hf	in-house	1.502	0.077	0.297	0.011	0.023	0.476	0.015	0.035	0.020	0.001
GWC-lf	in-house	1.553	0.084	0.416	0.008	0.022	0.445	0.011	0.039	0.019	0.001
GWC	[62]	1.51	0.09	0.40	0.014	0.022	0.48	0.020	n/a	0.060	0.006
GWD-u	in-house	1.088	1.138	0.142	0.013	0.225	0.599	0.004	0.765	0.007	0.008
GWD-hf	in-house	1.260	1.187	0.151	0.013	0.230	0.624	0.004	0.793	0.006	0.006
GWD-lf	in-house	1.257	1.254	0.174	0.012	0.236	0.625	0.004	0.805	0.006	0.007
GWD	[63]	1.14	1.11	0.15	0.015	0.220	0.60	<0.001	0.74	n/a	0.013
BBA	n.d.	1.39	0.64	0.21	0.013	0.170	0.50	n/a	n/a	n/a	n/a
FWA	[64]	1.06	0.13	0.60	0.02	0.2	0.46	0.2	1.57	0.018	n/a

3.1.2 Thermal treatment

During the manufacturing process an RPV steel is exposed to several heat treatment steps. A heat treatment procedure [56] typical for the production of a base material is shown in Fig. 11. Here, the steel is austenitized at 880 °C and water-quenched to room temperature, followed by a tempering step at 640 °C.

The situation is more complex for welds: A multilayer welding seam typically experiences a temperature-time regime which strongly varies from position to position in the material. This gives rise to a heterogeneous microstructure. A typical temperature profile, as for base material, can therefore not be specified.

To reduce internal stresses, the whole bulk material is finally exposed to a stress-relief treatment. The stress relieve heat treatment does however not alter the nanostructure. A detailed discussion on heat treatments and its effects on the materials can be found elsewhere [65, 66].

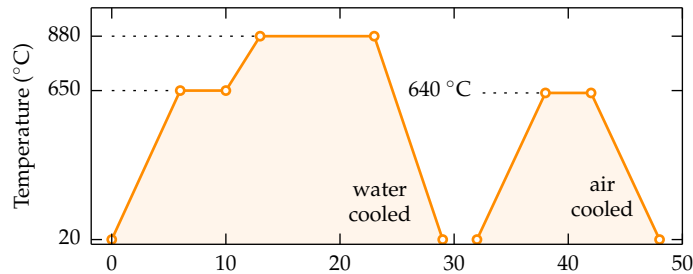


Figure 11: Temperature profile of a typical heat treatment of RPV steel: Austenitizing, quenching and tempering.

3.1.3 Irradiation conditions

The irradiation conditions are listed in Table 2. The unirradiated condition of each material was taken as reference to investigate only irradiation-induced changes of the nanostructure and mechanical properties.

For material JPB and JPC two sets of irradiation campaigns were performed, each in a different reactor: The first irradiation campaign was conducted at the now decommissioned prototype reactor VVER-2 in Rheinsberg (RH), Germany, at an irradiation temperature of $T_{\text{irr}} = 255 \text{ }^\circ\text{C}$. Further details on the irradiation conditions and the calculations on the fluence levels can be found elsewhere [67, 68].

The second irradiation campaign was initiated within this thesis and subsequently performed at the material-test reactor BR-2 in Mol, Belgium. The irradiation temperature was $(290 \pm 5) \text{ }^\circ\text{C}$, which is – in contrast to the relatively low irradiation temperature of the RH irradiation – a typical temperature of RPVs in western light water reactors. The medium- and the high-fluence level of the BR2 irradiations are higher by a factor of about 2 compared to the RH irradiations. However, this was attained within less than one tenth of the irradiation time of the RH irradiations. Further details about this irradiation campaign are found in an external LONGLIFE report [69].

The materials of the G-series were provided by Areva GmbH. The low-flux conditions ($\approx 0.05 \cdot 10^{12} \text{ n cm}^{-2} \text{ s}^{-1}$) originate from surveillance programs of German nuclear reactors. Accelerated neutron irradiations with higher fluxes ($\approx 1 \dots 2 \cdot 10^{12} \text{ n cm}^{-2} \text{ s}^{-1}$) were performed at the test reactor VAK, Kahl (Germany).

For material BBA, a high- and a low-flux condition is available. The high-flux condition of the base metal was irradiated at BR-2 in Mol, Belgium. The low-flux condition originates from a surveillance program.

Table 2: Irradiation conditions of the samples investigated. Neutron fluences, ϕt , and fluxes, ϕ , given for energies $E > 1$ MeV. T_{irr} is the irradiation temperature. The irradiation time t_{irr} is given in effective full-power days.

Material	Reactor	ϕt (10^{19} n/cm 2)	ϕ (10^{12} n/cm 2 /s)	t_{irr} (d)	T_{irr} ($^{\circ}$ C)
	–	0	–	0	–
JPB RH [8]	RH	0.737	0.1077	792	255
	RH	5.702	2.224	297	255
	RH	8.941	3.487	297	255
	–	0	–	0	–
JPC RH [8]	RH	0.867	0.1267	792	255
	RH	5.702	2.224	297	255
	RH	8.941	3.487	297	255
	–	0	–	0	–
JPB BR $_2$ [70]	BR $_2$	1.15	6.4	21	290
	BR $_2$	6.38	35.4	21	290
	BR $_2$	15.03	83.4	21	290
	–	0	–	0	–
JPC BR $_2$ [70]	BR $_2$	2.53	14	21	290
	BR $_2$	9.31	51.6	21	290
	BR $_2$	11.67	64.7	21	290
	–	0	–	0	–
GBC [62]	NPP	3.03	0.219	1605	300
	NPP	2.99	0.0414	8353	300
	–	0	–	0	–
GWC [62]	NPP	3.02	0.218	1605	300
	NPP	2.99	0.0414	8353	300
	–	0	–	0	–
GWD [63, 64]	VAK	2.21	2.1	122	288
	NPP	2.23	0.0609	4238	285
	–	0	–	0	–
BBA [71]	BR $_2$	6.38	35.5	21	290
	n/a	6.41	0.1	7419	290
	–	0	–	0	–
FWA [64]	LV	4.0	1.6	289	270
	LV	4.2	0.28	1736	270

Two samples of material FWA were irradiated with high and low neutron flux, respectively, up to the same level of fluence. Further details can be found in the LONGLIFE report D3.1 [64].

3.1.4 *Tensile Tests*

The yield stress, σ_y , and its irradiation-induced increase, $\Delta\sigma_y$, is given in Table 3. The tensile tests of the samples from the RH irradiation were performed at room temperature with a servo-hydraulic 50 kN test system MTS-810 at a constant cross-head velocity of 0.25 mm/min. The dumbbell-shaped sample geometry is shown in Fig. 12 on the right, with a length of 20 mm and a diameter of 6 mm.

The other values are taken from published literature. Details about the experimental conditions can be found in the publications listed in Table 3. Each value of σ_y , which is given in Table 3 is calculated from the mean value of at least three tensile experiments.

Table 3: Yield stress σ and yield-stress increase $\Delta\sigma$ for the different materials and irradiation conditions. The fluence levels ϕt and fluxes ϕ are referring to neutron energies $E > 1$ MeV.

Material	ϕt (10^{19} n/cm ²)	ϕ (10^{12} n/cm ² /s)	σ_y (MPa)	$\Delta\sigma_y$ (MPa)
JPB RH [8]	0	–	511	–
	0.737	0.1077	595	84
	5.702	2.224	637	126
	8.941	3.487	734	223
JPC RH [8]	0	–	497	–
	0.867	0.1267	562	65
	5.702	2.224	590	93
	8.941	3.487	695	198
JPB BR ₂ [70]	0	–	507	–
	0.61	3.4	554	47
	4.05	22.5	592	85
	7.31	40.5	627	120
	13.36	74.1	673	166
	15.46	85.7	686	180
JPC BR ₂ [70]	0	–	499	–
	1.45	8.0	519	20
	5.38	29.8	549	50
	9.96	55.2	585	86
	11.1	61.6	598	99
	11.69	64.8	590	91
GBC [62]	0	–	430	–
	0	–	415	–15
	3.44	2.48	517	87
	3.37	2.43	512	82
GWC [62]	0	–	481	–
	0	–	487	6
	3.33	0.24	535	54
	3.35	0.24	533	52
GWD [63, 64]	0	0	604	–
	1.37	0.037	788	184
	2.16	2.049	821	217
	2.23	0.061	789	185
BBA [71]	0	–	n/a	–
	6.38	35.5	533	n/a
	6.41	0.1	552	n/a
FWA [64]	0	–	379	22
	0	–	381	270
	4.1	1.6	652	22
	3.9	1.6	541	270

3.2 EXPERIMENTAL SET-UP

3.2.1 *Small-angle neutron scattering*

SAMPLE GEOMETRIES: The majority of SANS specimens were prepared from sections of impact testing samples. The sample geometry and the applied cutting scheme is shown on the left side in Fig. 12. The samples were cut to a dimension of $(10 \times 10 \times 1) \text{ mm}^3$. A circular aperture of 7 mm inner diameter is used for this sample geometry.

For some irradiations, no impact testing specimens were available, and sections of the cylindrical heads (diameter of 6 mm) of tensile specimens are used as material source for the SANS specimens, as shown in Fig. 12 on the right. Here, a smaller aperture of 5.5 mm in diameter is used. The smaller aperture is compensated with a longer measuring time for similar statistics compared to the SANS experiments from impact testing samples. The thickness, d_s , is chosen to be 1 mm for both geometries. For steel, a sample thickness of about 1 mm gives the best compromise between a good count rate on the detector and a negligible probability for multiple scattering [50].

The precise value of d_s for each sample is determined after sectioning with an accuracy of $\pm 1 \text{ }\mu\text{m}$ since the precise sample thickness needs to be known for absolute calibration.

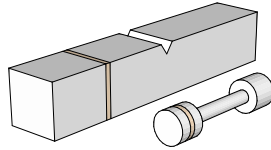


Figure 12: The SANS specimens (orange) are sectioned from impact testing samples (left) or the smaller tensile testing samples (right).

The unirradiated samples are sectioned with a water-cooled diamond cut-off saw. The irradiated samples are cut with a wire-traveling electro-erosive discharging machine (EDM). Differences in sample-surface properties do not have a significant impact on scattering, as SANS probes the whole through-thickness volume of the samples.

SANS FACILITIES: The set-up of a typical SANS experiment is schematically depicted in Fig. 13. A continuous stream of polychromatic neutrons is generated in a nuclear reactor, which is usually located at a distance of at least 100 m from the detector position to maintain a low background noise. The fast neutrons from the reactor are decelerated in a moderator tank filled with D_2O and guided to a mechanical velocity selector, which consists of high-speed rotating blades made of a neutron absorbing material. The neutron wavelength spread, $\Delta\lambda/\lambda$, after the velocity selector is between 9 and 12 %, depending on the experimental set-up. Several wave guides are positioned in the beam for collimation. By adding or removing the guides, the collimation is adjusted in accordance with the selected sample-detector distance. At

the lowest collimation setting, the neutron flux at the sample position is of the order of $10^8 \text{ n cm}^{-2} \text{ s}^{-1}$ at the best facilities.

The incident neutrons are scattered in the sample by nuclear and magnetic interaction. Since the sample is exposed to a magnetic field, B , perpendicular to the neutron beam, the magnetic interaction is suppressed in this direction. The position sensitive detector is placed behind the sample at a distance SD . The detector position can be moved on the beam axis to adjust the covered Q range.

A beam stop, usually made of B_4C or Cd , is placed behind the sample in the beam trajectory to prevent the detector from overcharging due to the transmitted neutrons.

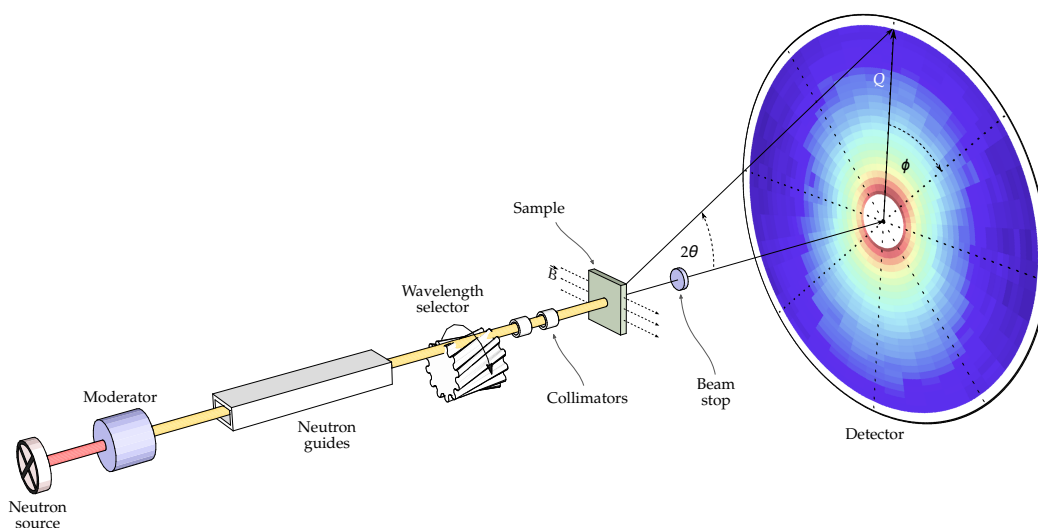


Figure 13: Schematic view of a SANS set-up. The moderated neutron beam is guided through a wavelength selector. After collimation, the neutrons beam is scattered in the sample. The sample is placed in a magnetic field to separate nuclear and magnetic scattering contribution.

To gain access to sufficient beam time for all SANS experiments foreseen, scientific proposals were submitted to different SANS facilities. One cycle – consisting of proposal submission, review, experiment and analyses – takes about one year. The facilities and experimental conditions are listed in Table 4.

The detector D11 at ILL Grenoble was upgraded during the time-span of this work to a newer model with larger detector diameter, d_{det} , and higher pixel count. The experimental parameters were adjusted accordingly.

Each sample is measured at two sample-detector distances $SD_{1,2}$ to cover a sufficiently broad Q -range of $0.5 \dots 3.2 \text{ nm}^{-1}$. The first distance SD_1 is chosen to be as short as possible given the experimental constraints, which consist of the sample holder geometry at the detector chamber entrance the magnet geometry. The distance between the pole pieces needs to be $< 2 \text{ cm}$ to attain a sufficiently high magnetic field of $B > 1.2 \text{ T}$ at the sample position. However, if the sample-detector distance is too small, the pole pieces cause shadowing effects on the detector. The

Table 4: Main parameters and set-up of the SANS experiments. All experiments are performed at two sample-detector distances, SD. d_{det} is the detector diameter, EC the empty cell for efficiency correction, λ the neutron wavelength and B the magnetic field strength on the sample position.

Institute	Detector:				Parameters:					
	Name	Type	d_{det} (m)	Pixel	EC	λ (nm)	SD ₁ (m)	SD ₂ (m)	B (T)	Software
HZB Berlin	V4	¹⁰ B	1.0	128 × 128	H ₂ O	0.605	1.7	8.0	1.2	BerSANS
ILL Grenoble	D11	³ He	0.64	64 × 64	H ₂ O	0.5	1.46	5.95	1.3	GRASP
ILL Grenoble	D11	³ He	1.0	128 × 128	H ₂ O	0.6	1.5	8.0	1.3	GRASP
KFKI Budapest	YS	BF ₃	0.64	64 × 64	H ₂ O	0.573	1.03	5.6	1.4	BerSANS
LLB Saclay	PAXE	BF ₃	0.64	64 × 64	Plexi	0.55	1.58	5.08	1.8	Own code

second distance SD₂ is chosen to extend the Q range as far as possible to small values with a short overlap of the Q range obtained from the first distance.

The uncertainty estimation of the measured detector counts is based on Poisson statistics ($\sim \sqrt{n}$). For sufficient data quality, the total number of detector counts is set to be $> 10^6$ per measurement. This is achieved with measuring times ranging from 30 minutes to up to 8 hours, depending on the available neutron flux at the facility and the corresponding geometry set-up.

RAW-DATA TREATMENT: The neutron counts I_{ij}^{raw} are recorded for each pixel (i, j) on the position sensitive detector (PSD). The raw values are corrected in data treatment for dead time τ and normalized according to

$$I_{ij} = \frac{I_{ij}^{\text{raw}}}{\left(1 - \frac{\tau}{t} \sum I_{ij}^{\text{raw}}\right) \cdot N_{\text{mon}}}, \quad (41)$$

where t is the total measurement time and N_{mon} the number of neutron monitor counts. To perform the full correction to absolute units of the sample scattering $(d\Sigma/d\Omega)_{s,ij}$, additional properties of the set-ups are taken into consideration:

- The transmission factor of the sample T_s is measured. For this, the beam stop is removed, and an attenuator is inserted into the direct beam to protect the detector from overload.
- The scattering intensity and transmission of the empty sample holder $I_{\text{EB},ij}$ and T_{EB} , respectively, is recorded.
- The background signal $I_{\text{Cd},ij}$ is determined with a neutron absorber (e.g. cadmium sheet) positioned at the sample position.
- The measurement of the scattering intensity of water $I_{\text{H}_2\text{O},ij}$ and its transmission factor $T_{\text{H}_2\text{O}}$ are utilized for two corrections: First, the isotropic signature of

the water scattering is used to correct for varying pixel efficiency on the detector. Second, the measured intensity is normalized to the known [25] scattering-cross section of water $(d\Sigma/d\Omega)_{\text{H}_2\text{O}}$ for calibration to absolute units.

- To correct for effects of the water cuvette (empty cell), its scattering intensity $I_{\text{EC},ij}$ and transmission factor T_{EC} are taken into account.

The full correction is then calculated according to

$$\left(\frac{d\Sigma}{d\Omega}\right)_{s,ij} = \frac{\frac{I_{s,ij} - I_{\text{Cd},ij}}{T_s T_{\text{EB}}} - \frac{I_{\text{EB},ij} - I_{\text{Cd},ij}}{T_{\text{EB}}}}{\frac{I_{\text{H}_2\text{O},ij} - I_{\text{Cd},ij}}{T_{\text{H}_2\text{O}} T_{\text{EC}}} - \frac{I_{\text{EC},ij} - I_{\text{Cd},ij}}{T_{\text{EC}}}} \cdot \left(\frac{d\Sigma}{d\Omega}\right)_{\text{H}_2\text{O}}. \quad (42)$$

In addition, the same reference steel sample was measured at each beam line for cross-checking the calibration. Further details on the corrections of the raw-data and calibration are found elsewhere [72–74].

A saturation magnetic field is applied perpendicular to the neutron beam and parallel to the x direction of the detector (see also Fig. 13). The spin alignments from the magnetic field lead to an angular-dependent magnetic scattering contribution on the detector screen, such that

$$\left(\frac{d\Sigma}{d\Omega}(Q_k)\right)_{\text{tot}} = \left(\frac{d\Sigma}{d\Omega}(Q_k)\right)_{\text{nuc}} + \left(\frac{d\Sigma}{d\Omega}(Q_k)\right)_{\text{mag}} \sin^2 \alpha. \quad (43)$$

In data treatment, this $\sin^2 \alpha$ dependence is fitted to the two-dimensional scattering intensity (Fig. 14) for each length of scattering vector Q_k . The beam-stop affected area and faulty pixels on the detector are masked out and do not contribute to the fit. The results are two one-dimensional, Q -dependent scattering curves: the nuclear and the magnetic scattering-cross section. Both curves still include an incoherent scattering contribution,

$$\left(\frac{d\Sigma}{d\Omega}(Q_k)\right)_{\text{nuc, mag}} = \left(\frac{d\Sigma}{d\Omega}(Q_k)\right)_{\text{nuc, mag}}^{\text{coh}} + \left(\frac{d\Sigma}{d\Omega}\right)_{\text{nuc, mag}}^{\text{inc}}, \quad (44)$$

originating mainly from the mixture of natural isotopes and heterogeneities in the material smaller than the resolution limit of SANS. Typically, the value for the nuclear incoherent scattering is around $(0.005 \pm 0.002) \text{ cm}^{-1}$, while the magnetic part is about one magnitude lower due to the absence of the isotopic contribution. Using a method introduced by Porod [75, 76], the scattering cross-section is approximated for large Q values (i.e. $QR > 2$) with

$$\left(\frac{d\Sigma}{d\Omega}\right) \cdot Q^4 = A + B \cdot Q^4, \quad (45)$$

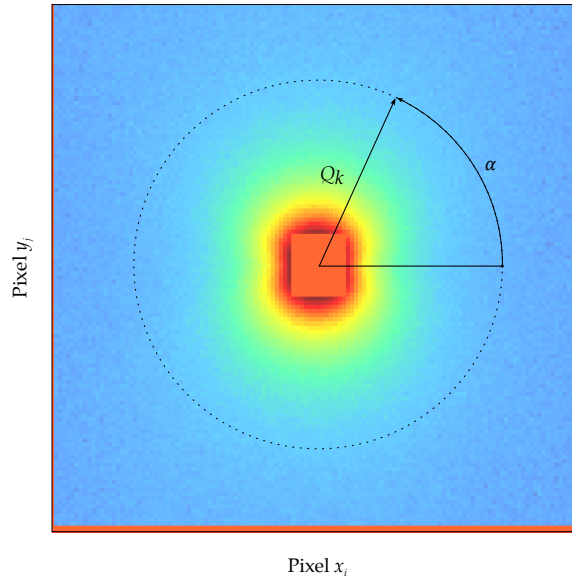


Figure 14: Calibrated and efficiency-corrected SANS scattering intensity pattern. The orange colored areas in the center and corner are masked out pixels. For each Q_k the intensity is fitted along the angle α . The magnetic field is applied parallel to the x -axis and perpendicular to the beam direction.

where the slope, B , of the linear fit is the incoherent contribution $(d\Sigma/d\Omega)^{\text{inc}}$ (see also Section 2.2.1). This approach is used to specify the incoherent scattering contribution for the unirradiated reference condition of a material in the present work.

For the irradiated conditions, it was found that Eq. (45) yields in a strong overestimation of incoherent contribution and, therefore, cannot be applied. To avoid any ambiguity of the results, the value determined for the unirradiated reference sample is used to correct measurements of the irradiated samples.

Finally, after calibration and background correction, the scattering curve of the unirradiated material is subtracted from the scattering curve of all as-irradiated conditions of the same material. Therefore, the resulting difference-scattering curve contains explicit information about the irradiation-induced features in the material.

TRANSFORMATION TO SIZE DOMAIN: The nuclear and the magnetic difference-scattering curves are fitted by means of the Monte-Carlo fitting (MCF) routine introduced in Section 3.2.1. This yields a representation of the irradiation-induced features in terms of number-density and volume-size distribution.

The following parameters are used as boundary conditions for the transformation: The minimum radius of scatterers is set to $R_{\text{min}} = 0.5$ nm. Features with a radius smaller than ≈ 0.5 nm are below the resolution limit of SANS and are not taken into account during analysis. A maximum radius of $R_{\text{max}} = 7.5$ nm ensures a sufficiently large headroom for large features detected in the measured Q range. The radius increment is set to a constant value of $\Delta R = 0.05$ nm.

The experimental scattering curve is fitted with a scattering curve constructed from the summation of spherical form factors of different radii. The radii used are

progressively drawn from a pool of random numbers. These are generated with uniform probability distribution, ranging from R_{\min} to R_{\max} . The total number of radii in the pool is set to $2 \cdot 10^6$. This is sufficient to reach fit convergence in the present cases. Each fit is repeated ten times for one experimental scatter curve; each single fit with a newly generated pool of random radius values. The final fit result is determined from the χ^2 -weighted arithmetic mean of the ten converged fits.

The scattering contrast, $\Delta\eta^2$, needs to be set for the calculation of the volume fraction and number density of clusters in the material. According to Eq. (14), a value of $\Delta\eta_{\text{mag}}^2 = 2.598 \cdot 10^{-7} \text{ nm}^{-4}$ for the magnetic scattering contrast is used. This value corresponds to the contrast of non-magnetic scatterers embedded in a magnetic α -Fe matrix (see Section 2.2.1). Given the integrated measured scattering cross section (i.e. the product of scattering contrast and total volume fraction of scatterers, see Section 2.2.1, Eq. (18) and (21)), a higher contrast results in a lower volume fraction. It therefore yields a lower bound for the true cluster-volume fraction. The nuclear scattering contrast strongly depends on the chemical composition of clusters. However, in most cases the composition is not known. If the composition is available from other techniques, such as APT, the nuclear scattering contrast can be calculated directly.

The A ratio is an indirect indicator of the chemical composition of clusters, as introduced in Section 2.2.1 and defined in Eq. (15). In the present work, the A ratio is calculated for each measurement *after* transformation to size space, such that

$$A = \left(\frac{d\Sigma_{\text{mag}}}{d\Omega} \bigg/ \frac{d\Sigma_{\text{nuc}}}{d\Omega} \right) + 1 \xrightarrow{\text{MCF}} A = \frac{\int N_{R,\text{mag}} \bar{R}_{\text{mag}}^6 dR \Delta\eta_{\text{mag}}^2}{\int N_{R,\text{nuc}} \bar{R}_{\text{nuc}}^6 dR \Delta\eta_{\text{nuc}}^2} + 1. \quad (46)$$

Both definitions of A , Eq. (15) and the right-hand side of Eq. (46), are equivalent, given that the MCF transformation is a good representation of the experimental scattering data. However, the second relation in Eq. (46) has the advantage that possible size-dependent changes of the A ratio, i.e. of the chemical composition of the clusters, are directly visible.

The final fit result is presented in terms of cluster-size distribution, weighted with respect to both the cluster-volume, $f_{v,R}$ and the cluster-number density, N_R , according to Eqs. (20) and (21), respectively. The mean cluster radius, \bar{R} , is determined directly from the number-density weighted distribution, Eq. (22).

3.2.2 Atom-probe tomography

SAMPLE PREPARATION: The APT samples are prepared in a two-step process: First – similarly as for the SANS specimens – the APT specimens are sectioned by EDM from either impact or tensile specimens, as shown in Fig. 12. Depending on the original geometry, the samples are cut to a rectangular shape of either $0.3 \times 0.3 \times 10.0 \text{ mm}^3$ or $0.5 \times 0.5 \times 6.0 \text{ mm}^3$. Special care is taken to produce rods of square cross section (within margins of about 0.05 mm). Larger deviations lead to ellipsoidal tip shapes upon the subsequent electro-polishing step. Since the 3D reconstruction

algorithm assumes a spherical tip geometry, an ellipsoidal tip can lead to strong distortions in the reconstructed sample volume.

The APT experiments are performed at the Institute for Material Physics (GPM) of the University of Rouen, France. Final tip preparation was performed at GPM just before the APT experiment to minimize oxidation effects on the tip surface. Fig. 15 shows the two set-ups, which were used for the electro-chemical polishing of the rectangular rods into thin needles with a tip radius $R_{\text{tip}} < 70$ nm. In Fig. 15a, the sample rod is inserted into a two-layer solution of perchloric-acetic acid (ratio 1 : 3) and a chemically inert PFPE¹-liquid.

The material is eroded and a neck is formed by moving the center of the sample up and down inside the acidic liquid and by applying a voltage of about 12 V. The up and down movement is continued until the rod is split into two pieces at the thinnest part of the neck. The sample tips are then examined in a TEM for residual oxides on the surface and the tip radius is checked. The TEM image of a sample with a sufficiently small tip radius ($R_{\text{tip}} \approx 60$ nm) is shown in Fig. 16a.

In case the tip radius is too large, the sample is re-polished in a micro-loop setup, shown in Fig. 15c. The set-up consists of a Pt-wire loop, which is covered with a drop of acidic solution. While inserting the tip into the drop, a pulsed voltage of about 6 V is applied. The first third of the tip is moved rapidly in and out of the drop. This leads to the erosion of the material. The voltage pulses are immediately stopped when the thinned part of the tip breaks off, since further erosion would lead to an increase in tip radius.

A needle tip penetrating the acidic drop is shown in Fig. 16b. The area of erosion is controlled precisely by a micrometer-moving table and an optical microscope directed to the interface between acidic drop and needle.

EXPERIMENTAL CONDITIONS: The experiments were performed on three different APT devices: The Energy Compensated Wide-Angle Tomographic Atom Probe (ECoWATAP), the Laser-Assisted Wide-Angle Tomographic Atom Probe (LaWATAP) and the Flexible Tomographic Atom Probe (FlexTAP). All devices are equipped with

¹ Perfluoropolyether

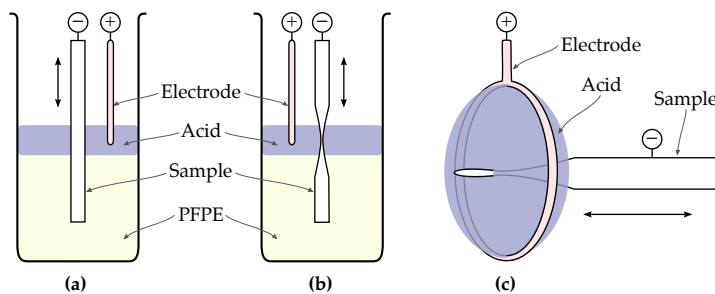


Figure 15: Schematic illustration of electro-polishing procedure: (a) The sample is moved up and down in an acidic solution. (b) A neck is formed at the acid layer. By continuing the erosion, the sample splits into two halves. (c) Re-polishing is performed in the micro-loop set-up (magnified view).

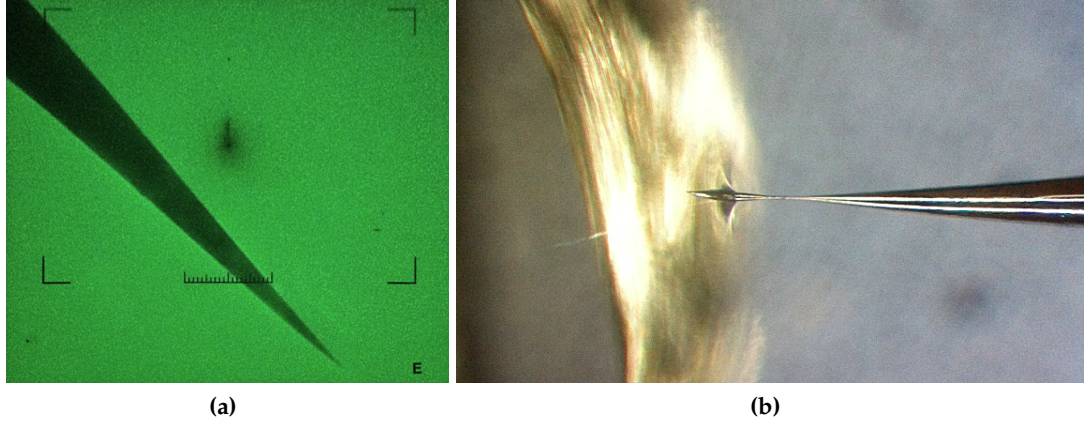


Figure 16: (a) The radius of the needle tip (here $R_{\text{tip}} \approx 60$ nm) is checked in a TEM. (b) View from an optical microscope of the re-polishing process of an APT needle in a micro-loop setup. The tip is inserted into the acidic solution.

an advanced delay-line detector, which has a high detection efficiency of about 60 % and can handle multi-hit events. Details on the different atom probes are listed in [77]. In all cases the evaporation of the tip surface is performed at a chamber temperature of 40 K with a pulse fraction of 20 %. This corresponds to the evaporation of a single atom every fifth laser pulse or electric pulse, respectively. The UV/green laser assisted evaporation is performed with a power of 0.9 to 1.1 mW.

DATA TREATMENT: The detector counts are evaluated in terms of mass-to-charge histograms in a range between 1 . . . 100 atomic-mass units (amu). The three-dimensional reconstruction is performed according to Section 2.3.1 with a calibrated $E\beta$ factor for each measurement. One experiment yields a total of 5 . . . 50 million atoms, depending on the tip quality and the device used. For cluster detection, the iso-concentration algorithm according to Section 2.3.2 is applied. The elements Mn, Ni, Si, Cu and P were specified as cluster elements (CL) and a threshold concentration, ρ_{CL} , of 9 . . . 11 % is set.

In addition, each cluster radius is manually checked for the following condition:

$$R_{\text{gyr}}^{(\text{CL})} \approx R_{\text{gyr}}^{(\text{CL} + \text{Fe})} \quad \text{within a margin of } \pm 0.2 \text{ nm}, \quad (47)$$

where $R_{\text{gyr}}^{(\text{CL})}$ and $R_{\text{gyr}}^{(\text{CL} + \text{Fe})}$ are the radii of gyration calculated with only CL atoms and with CL and Fe atoms, respectively. If the condition given in Eq. (47) is not fulfilled for a specific cluster, atoms from the cluster surface are removed by an erosion algorithm until the condition is fulfilled. This ensures that residual matrix atoms do not bias the size or composition of the cluster under investigation.

3.2.3 *Vickers hardness*

Hardness measurements are carried out after completion of the SANS experiments to avoid possible bias in the SANS measurements. The hardness testing is performed according to DIN EN ISO 6507-1:2005 with a micro-hardness testing device HSV-20 by Shimadzu. Each measurement point is calculated by the average of at least ten sampling points. The sample geometries are either $10 \times 10 \times 1 \text{ mm}^3$ cuts from impact testing specimens, or cylindrical disks with a diameter of 6 mm and a height of 1 mm, as also shown in the highlighted regions in Fig. 12.

Characterizing the irradiation-induced changes by hardness measurements has several advantages over yield-stress measurements: On the one hand, the hardness measurements can be performed on the already available SANS specimens. This means that both SANS and HV10 results are measured in the same sample volume. Differences originating from large-scale material inhomogeneities can be neglected. On the other hand, this parameter is easily accessible. Special sample preparation or geometry prerequisites are not necessary.

RESULTS

The experimental results are grouped into two main sections: In the first section, results regarding the flux effect are presented. Here, pairs of the same materials were irradiated up to the same level of neutron fluence with different neutron fluxes. The irradiation-induced changes for both the high- and the low-flux condition were investigated by means of SANS and hardness measurements – both methods performed on the same specimen.

The second section comprises the results of LBE-related experiments. The focus here lies on low-Cu reference steels JPB and JPC. Both materials were neutron-irradiated at two different reactors, RH and BR2, comprising different irradiation conditions. For each irradiation campaign and each material, three fluence levels are investigated by means of SANS and Vickers hardness measurements. This is followed by the presentation of complementary APT results on the non-irradiated, the medium- and the high-fluence samples of material JPC-RH.

4.1 FLUX EFFECTS (SANS)

Five different RPV steels are selected for the investigation of flux effects on the nanostructure and mechanical properties. The results of the SANS experiments are shown in Figs. 17 and 18. Each plot shows the results for one flux pair of a material, comprising the high- and the low-flux condition, which were irradiated up to the same level of neutron fluence. On the left side of Figs. 17 and 18, i.e. Subfigs. (a), (c) and (e), the empty markers depict the measured magnetic difference-scattering cross-section, with the unirradiated condition taken as reference. The error bars show the uncertainties of the least squares \sin^2 -fit to the 2D scattering pattern on the detector. Each scattering curve is transformed into a representation in size space via the MCF routine, introduced in Section 3.2.1. The fit to the difference scattering cross-sections is indicated by the solid line. The corresponding cluster-size distribution is depicted on the right side of Figs. 17 and 18, i.e. Subfigs. (b), (d) and (f).

The cluster-size distributions are given in terms of volume-weighted $f_{v,R}$ and number weighted cluster-size distribution¹. The mean cluster radius \bar{R} for each condition is highlighted with an empty circle marker in the number density representation, N_R . The shaded regions in the volume-size distribution, $f_{v,R}$, indicate the scatter band of the multiple fitting procedures (see Section 2.2.2).

The parameters of the cluster population, which are calculated from the cluster-size distributions in Figs. 17 and 18, and the hardness increase, ΔHV_{10} , are listed in Table 5. The uncertainties of the cluster parameters are calculated from the 3σ standard deviation of the set of multiple MCF fits and give an estimate of the fit

¹ Indicated by the sparklines on top of each plot marked as N_R .

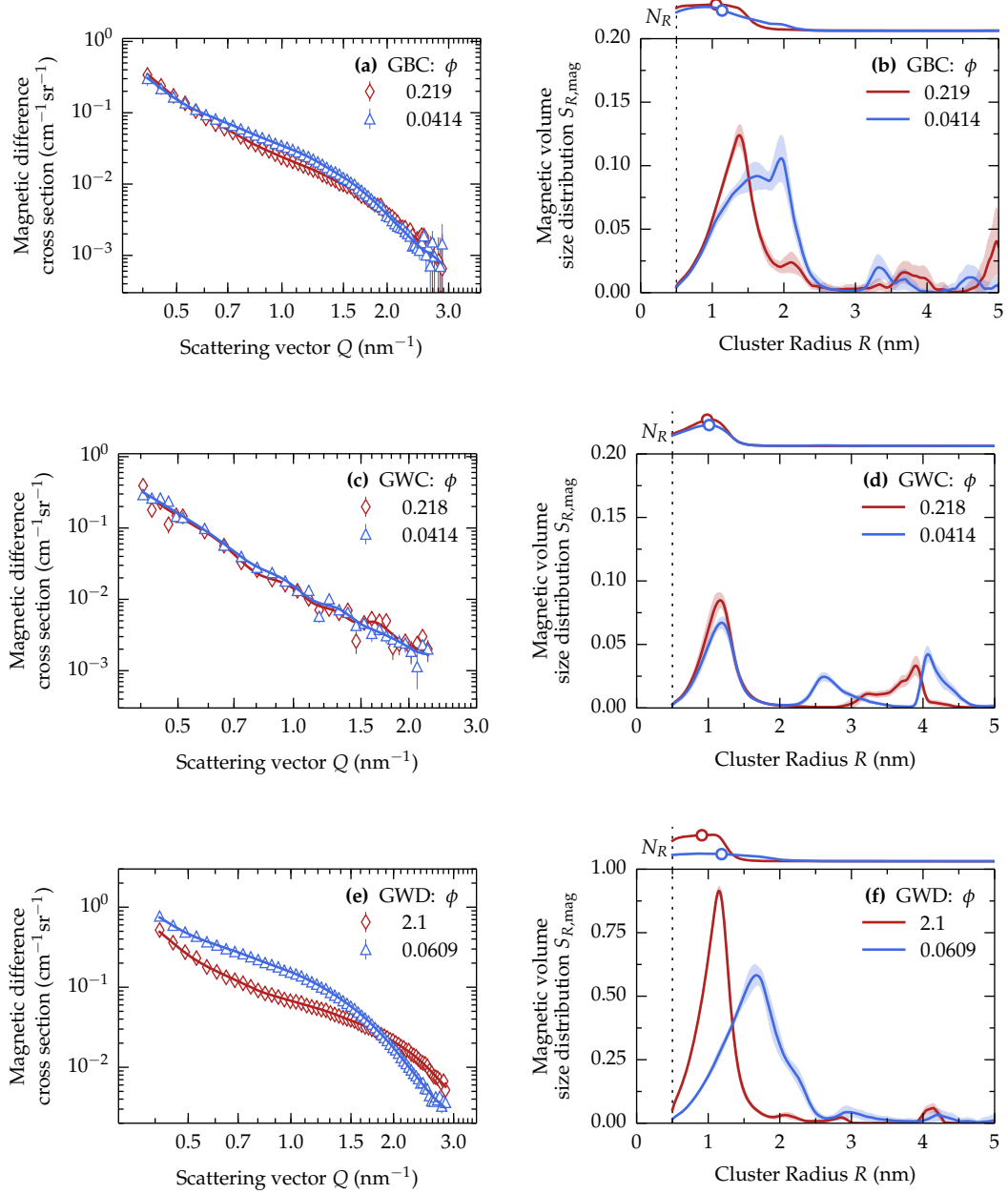


Figure 17: SANS results for materials GBC, GWC and GWD in high- and low-flux condition. Neutron flux ϕ in 10^{12} n/cm²/s. Plots (a), (c) and (e) show the measured magnetic difference-scattering curves (empty marker symbols) and the corresponding fitted scattering curves (solid lines). Plots (b), (d) and (f) show the reconstructed cluster-volume distribution in units of $S_{R,\text{mag}}$. The number-size distribution N_R (solid lines) and its mean cluster radius \bar{R} (circle markers) are indicated on top of each plot.

stability. Possible heterogeneities in the material and systematic measuring errors are not taken into account for the uncertainty estimation.

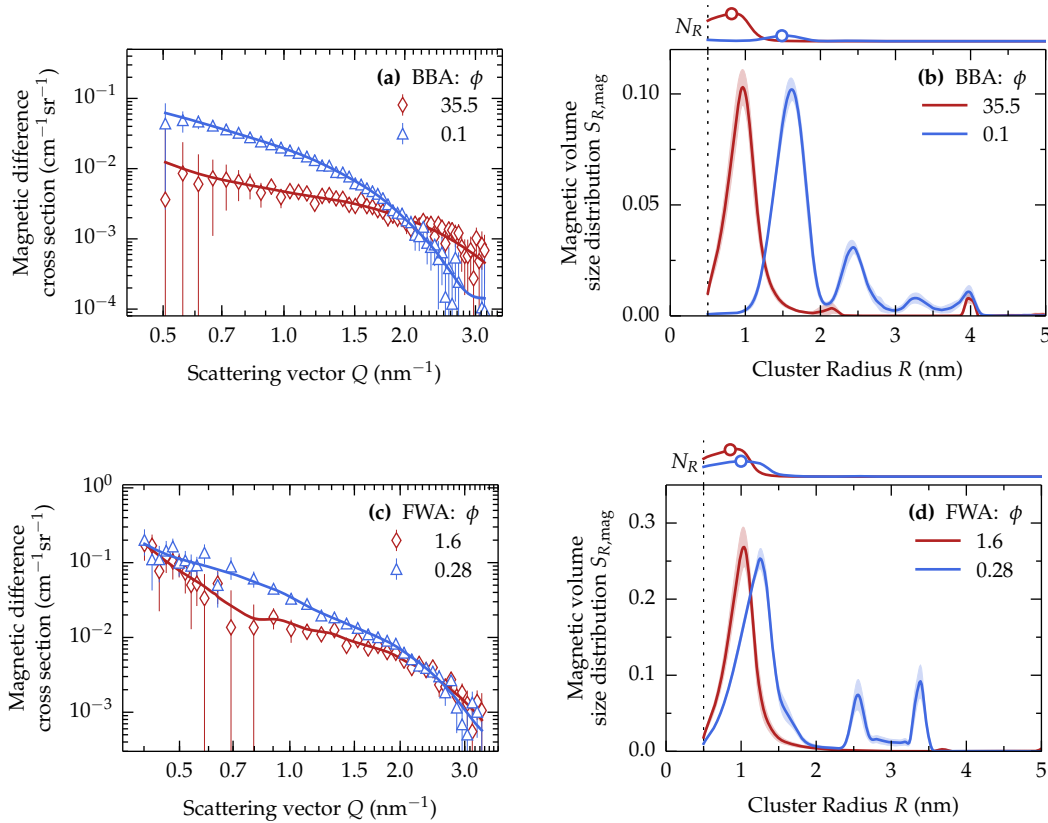


Figure 18: SANS results for materials BBA and FWA in high- and low-flux condition. Plots (a) and (c) show the measured magnetic difference-scattering curves (empty marker symbols) and the corresponding fitted scattering curves (solid lines). Plots (b) and (d) show the reconstructed cluster-volume distribution in units of $S_{R,\text{mag}}$. The number-size distribution N_R (solid lines) and its mean cluster radius \bar{R} (circle markers) are indicated on top.

The values from Table 5 are plotted in Fig. 19 as a function of neutron flux. Pairs of the same material, irradiated to the same fluences level, but different flux level, are connected by straight lines for visual guidance.

The slopes between each high- and low-flux cluster parameter from Fig. 19 are displayed in Fig. 20 with the corresponding uncertainties. No underlying model is assumed here. However, this allows a first estimate of the strengths of parameter shifts between the flux pairs.

Concerning the flux dependence of the measured cluster properties, the following observations are made from Table 5 and Figs. 19 and 20:

- Considering each single flux pair, the high-flux irradiation leads to the formation of clusters with smaller mean radii, \bar{R} , than the low-flux irradiation.
- For all materials, the cluster-number density, N , is higher for the high-flux irradiations. This trend is more pronounced for the high-Cu steels. Considering the uncertainties in Fig. 20b, it is evident that for some materials the effect is

Table 5: Parameters of irradiation-induced clusters and hardness increase of the flux-effect samples. Flux and fluence values are given for $E > 1$ MeV. The flux factor is the ratio between the low- and high-flux value of one flux pair. Cluster volume fraction f_v and number density N are both given assuming non-magnetic scatterers embedded in a homogeneous Fe matrix.

Material	ϕt (10^{19} n/cm 2)	ϕ (10^{12} n/cm 2 /s)	Flux factor	f_v (vol.%)	N (10^{16} cm $^{-3}$)	\bar{R} (nm)	A ratio	Δ HV10
GBC	3.03	0.219	5.3	0.172 ± 0.023	14 ± 1	1.07 ± 0.04	2.5 ± 0.3	23 ± 6
	2.99	0.0414		0.182 ± 0.020	13 ± 1	1.15 ± 0.03	2.5 ± 0.4	34 ± 5
GWC	3.02	0.218	5.3	0.123 ± 0.045	10 ± 3	1.01 ± 0.07	2.3 ± 0.5	34 ± 9
	2.99	0.0414		0.115 ± 0.041	8 ± 2	1.04 ± 0.09	1.9 ± 0.3	30 ± 8
GWD	2.21	2.1	34.5	0.579 ± 0.081	121 ± 12	0.91 ± 0.03	2.0 ± 0.4	89 ± 13
	2.23	0.0609		0.683 ± 0.063	57 ± 3	1.19 ± 0.03	2.1 ± 0.5	71 ± 13
BBA	6.38	35.5	355.0	0.052 ± 0.018	18 ± 5	0.82 ± 0.05	3.2 ± 0.9	24 ± 7
	6.41	0.1		0.074 ± 0.019	4 ± 1	1.49 ± 0.02	3.3 ± 0.6	23 ± 7
FWA	4.0	1.6	5.7	0.163 ± 0.053	40 ± 11	0.86 ± 0.05	2.2 ± 0.5	55 ± 15
	4.2	0.28		0.202 ± 0.009	30 ± 1	1.00 ± 0.01	2.2 ± 0.6	67 ± 17

smaller than the estimated uncertainty. However, the overall trend of increasing number density with increasing flux does apply for all materials.

- The volume fraction, f_v , exhibits a weak dependence on flux: The volume fraction at higher fluxes tend to be smaller than the volume fraction at lower fluxes. Although the trend seems to apply for most materials, the error bars are consistently larger than the effect for each individual material.
- There is no general trend for the flux dependence of the A ratio. This suggests that the composition of the clusters is similar for the low- and high-flux irradiation. In particular this finding guarantees that the measured flux dependencies of volume fraction and number density are not biased by a flux dependence of the cluster composition in combination with the assumption of non-magnetic clusters. The two materials with the lowest Cu content show a stronger change in A ratio, but it is smaller than the estimated error margins for the corresponding data point.
- The irradiation-induced increase of Vickers hardness does not exhibit any general trend. Taking into account the uncertainties of the measurements, the strength of the effect is consistent with flux-independent hardening.

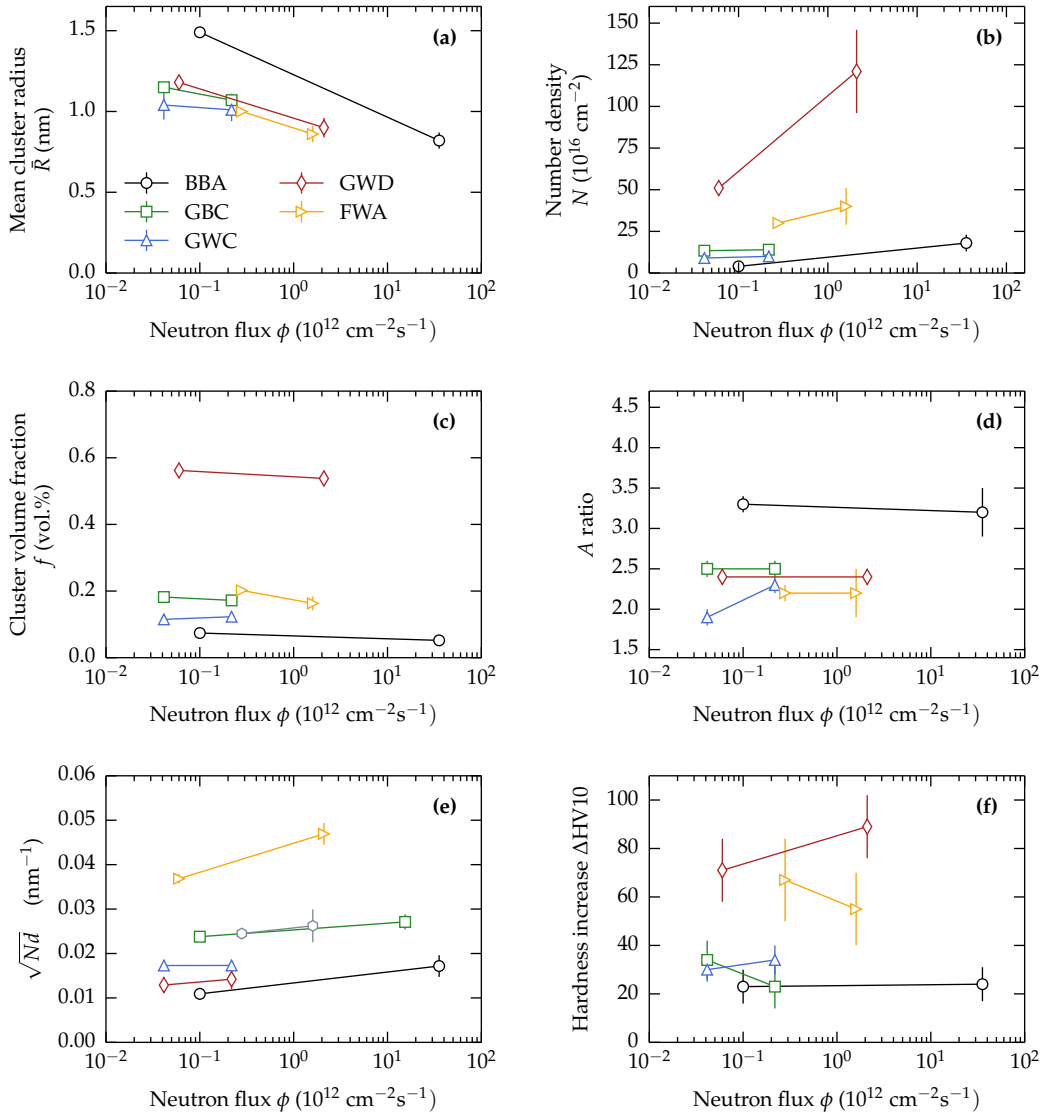


Figure 19: Characteristics of irradiation-induced clusters and hardness increase ΔHV_{10} as a function of the neutron flux ϕ for pairs of samples irradiated up to the same level of fluence. For visual guidance, the flux pairs are connected with solid lines, without assuming an underlying model.

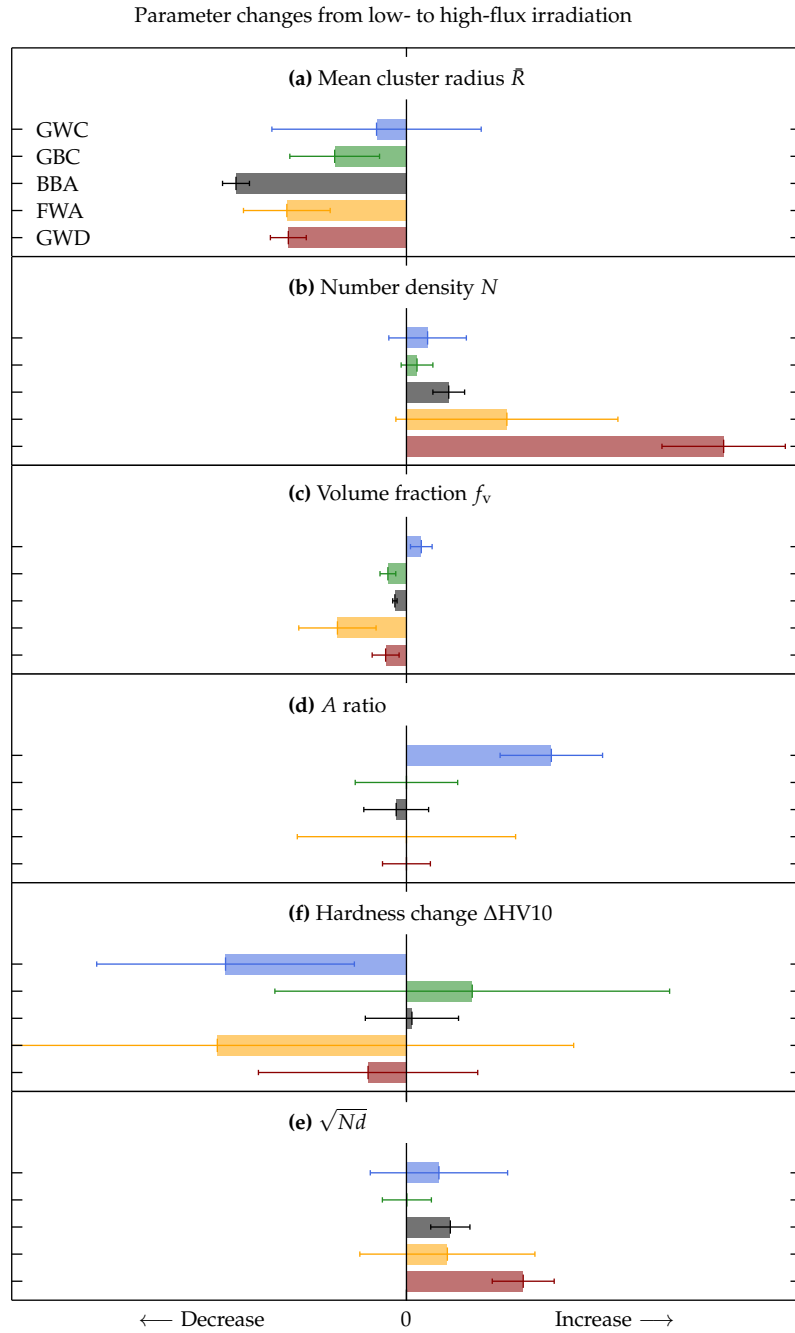


Figure 20: Changes of cluster parameters and ΔHV_{10} upon increased neutron flux: The bar lengths are determined from the semi-log slopes in Fig. 19 and are given in arbitrary units. The errors are calculated by standard error propagation from the values in Table 5. The materials are sorted by Cu content, ranging from GWC with the lowest, to GWD with the highest Cu content.

4.2 LATE-BLOOMING EFFECT (SANS)

For investigations on the late-blooming effect, the low-Cu reference steels JPB and JPC were irradiated at two reactors: The first irradiation campaign was performed at the RH prototype reactor. It comprised three fluence levels, which were accumulated at a comparatively low neutron flux and an irradiation temperature of 255 °C. The second irradiation campaign was performed at the BR2 material-test reactor at fluxes about one magnitude higher compared to the RH irradiations. This irradiation campaign was performed at a temperature of 290 °C, which is commonly used in western NPPs.

The investigation is focused on the fluence dependence of the parameters of the irradiation-induced cluster population. At both facilities, i.e. RH and BR2, each material was exposed to three level of fluences, from here on referred to as low, medium and high fluence.

Results of SANS experiments on the medium- and high-fluence samples of materials JPB-RH and JPC-RH were already reported before [8, 50]. The tentative observation of a possible LBE [8] motivated a deeper investigation as performed within the present thesis. A number of additional measurements were performed as specified below.

- SANS experiments on the low-fluence conditions of JPB-RH and JPC-RH,
- SANS experiments on selected post-irradiation-annealed conditions of JPB-RH and JPC-RH,
- SANS experiments on low-, medium- and high-fluence conditions of JPB-BR2 and JPC-BR2,
- APT measurements on selected conditions,
- Vickers hardness tests on the full set of conditions.

Moreover, the SANS data reported in [8, 50] were reanalyzed using the code described in Section 2.2.2 to improve accuracy, derive scatter-bands and guarantee consistent results.

Parts of the new analyses have been published [78] in a study on annealing effects of the same materials. The measurements on the low-fluence samples of the RH irradiation are added to the available data set.

The magnetic difference-scattering curves of the materials JPB and JPC irradiated at RH are shown on the left side of Fig. 21. The scattering curves of the BR2-irradiated materials are plotted on the left side of Fig. 22. In both figures the magnetic scattering curve of the unirradiated reference sample has been subtracted from the scattering curves of the irradiated samples. The neutron irradiation gives rise to an increase of the scattering-cross section over the whole range of the measured Q spectrum, indicating the presence of newly formed scatterers in the material matrix. To gain information on the properties of this population, the scattering-cross sections

are fitted by means of the MCF and transformed into size domain. The transformation is represented by the volume-weighted cluster size distribution shown on the right sides of both Figs. 21 and 22. The corresponding number-size distribution is indicated on top of the plots, where the mean cluster radius, \bar{R} , is highlighted by an empty circle marker. The parameters of the cluster population are calculated by the integration over the radius increment of the size distributions. The cluster parameters and the hardness increase, ΔHV_{10} , which were measured on the very same samples after the SANS measurements, are listed in Table 6. The cluster-volume fraction, f_v , is shown in Fig. 23 as a function of neutron fluence, ϕt .

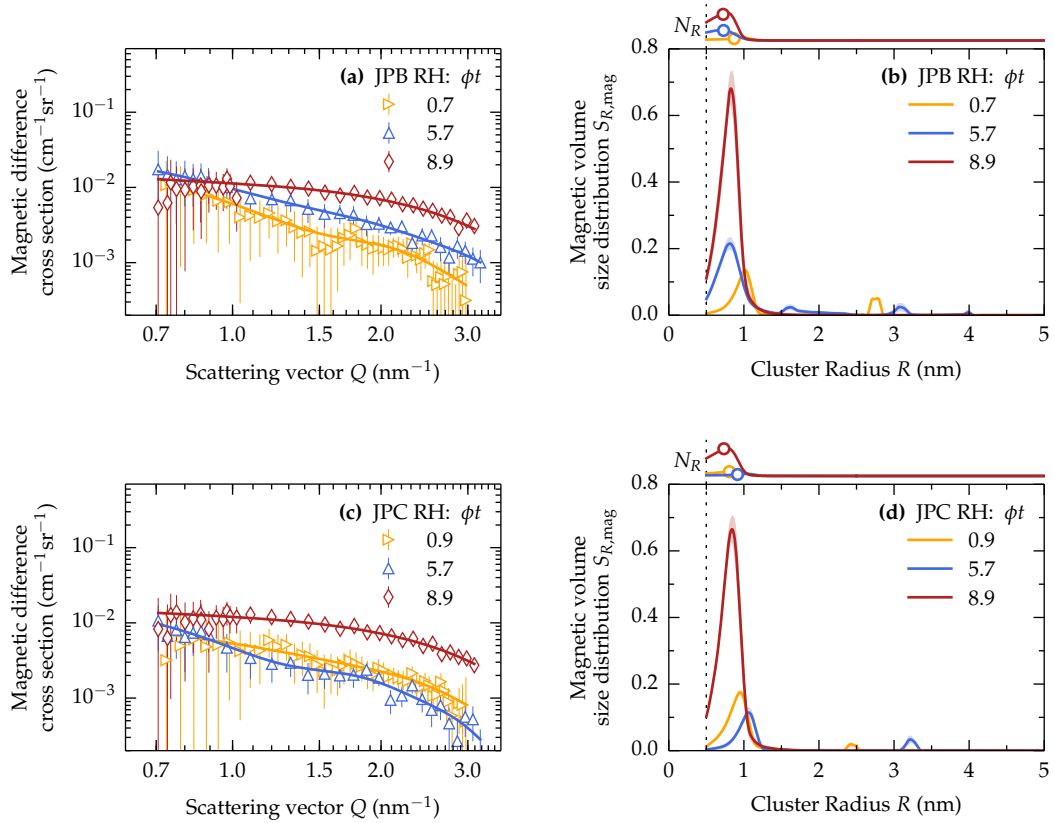


Figure 21: SANS results of materials JPB and JPC for the RH irradiation ($T_{\text{irr}} = 255 \text{ }^\circ\text{C}$) condition. Plots (a) and (c) show the measured magnetic difference-scattering curves (empty marker symbols) and the fits (solid lines). The corresponding cluster-volume distributions are shown in plot (b) and (d) in units of $S_{R,\text{mag}}$. The number-size distribution N_R (solid lines) and its mean cluster radius \bar{R} (circle markers) are indicated on top of each plot.

Concerning the parameters of the irradiation-induced cluster population, the following observations are made:

- The mean cluster radius \bar{R} does not show a general dependence on fluence or flux. The radii vary non-systematically between $\bar{R} = 0.72 \dots 0.91 \text{ nm}$ for all materials and irradiation conditions.

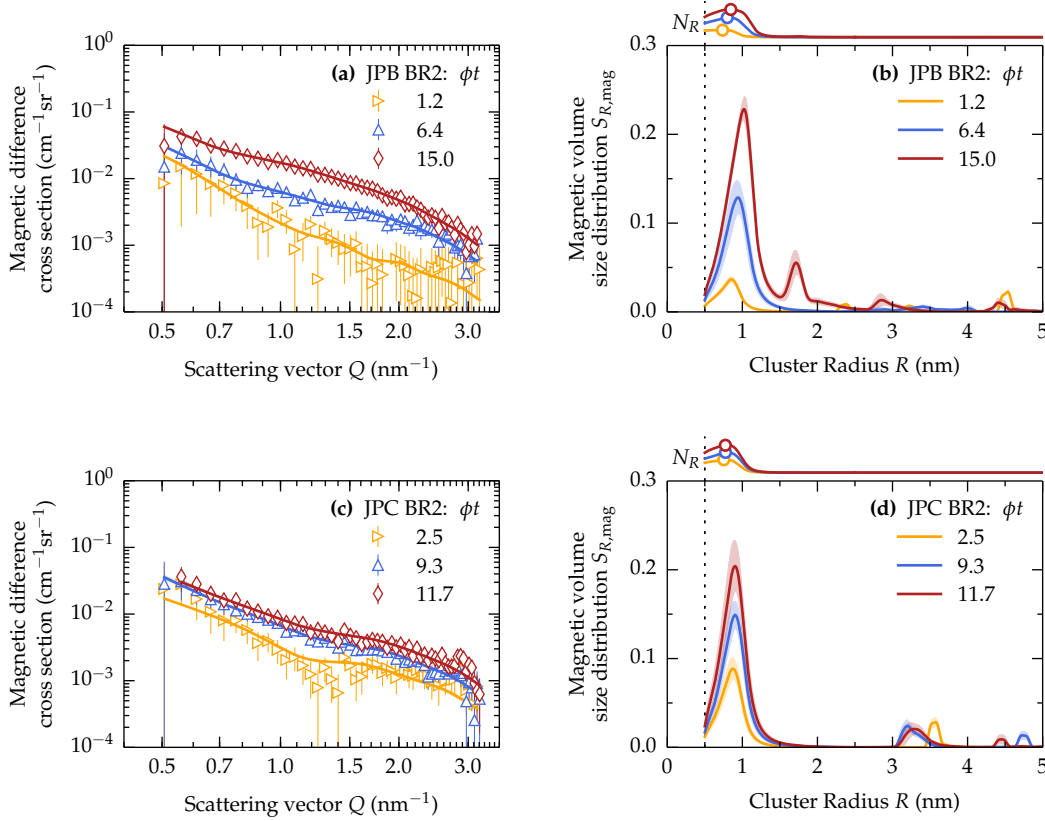


Figure 22: SANS results of materials JPB and JPC for the BR2 irradiation ($T_{\text{irr}} = 290 \text{ }^\circ\text{C}$) condition. Plots (a) and (c) show the measured magnetic difference-scattering curves (empty marker symbols) and the fits (solid lines). The corresponding cluster-volume distributions are shown in plot (b) and (d) in units of $S_{R,\text{mag}}$. Its number-size distribution N_R (solid lines) and its mean cluster radius \bar{R} (circle markers) are indicated on top of each plot.

- No clear dependence of the A ratio on the irradiation parameters or material composition is evident. This suggests that the clusters are of similar chemical composition for JPB and JPC for both irradiation campaigns.
- The RH irradiations were performed at a temperature 35 K lower and at fluxes an order of magnitude less on average than the BR2 irradiations. This is reflected in significantly higher cluster-volume fractions and number densities for the RH samples at similar levels of neutron fluence. Experimental results, allowing the effects of flux and temperature to be separated, are not available.
- The estimated uncertainties are larger for the BR2 irradiation than for the RH irradiation. This may be due to the higher neutron flux during the BR2 irradiation. A faster formation can lead to non-equilibrium interfaces between cluster and matrix. The application of a spherical form factor, Eq. (12), can thus lead to a lower stability of the fits and larger error margins of the cluster parameters.

- For the RH irradiated samples the fluence dependence of the cluster-volume fraction, f_v , exhibits a change of slope (CoS), i.e. the slope increases with increasing fluence. This effect is more pronounced for the material JPC. The hardness measurements reflect the findings of the SANS investigation.
- The clusters of the BR2 samples show a smooth, gradually increasing volume fraction with increasing fluence. A similar behavior is visible for the hardness increase. This is the fluence dependence usually observed, where power-law-like evolution with an exponent less or equal 1 is observed (see Fig. 2).

Table 6: The parameters of the irradiation-induced clusters and hardness increase for material JPB and JPC under RH and BR2 irradiation conditions.

Material	ϕt (10^{19} n/cm 2)	ϕ (10^{12} n/cm 2 /s)	f_v (vol.%)	N (10^{16} cm $^{-3}$)	\bar{R} (nm)	A ratio	Δ HV10
JPB RH	0.737	0.1077	0.038 ± 0.004	12 ± 1	0.87 ± 0.02	2.6 ± 0.7	26 ± 8
	5.702	2.224	0.096 ± 0.014	49 ± 4	0.73 ± 0.03	2.2 ± 0.4	45 ± 9
	8.941	3.487	0.216 ± 0.030	124 ± 8	0.72 ± 0.03	2.0 ± 0.2	67 ± 7
JPC RH	0.867	0.1267	0.060 ± 0.006	24 ± 2	0.81 ± 0.02	4.8 ± 2.2	25 ± 6
	5.702	2.224	0.033 ± 0.011	9 ± 1	0.91 ± 0.10	1.9 ± 0.4	36 ± 6
	8.941	3.487	0.221 ± 0.011	121 ± 3	0.73 ± 0.01	2.2 ± 0.3	61 ± 5
JPB BR2	1.15	6.4	0.015 ± 0.004	7 ± 2	0.74 ± 0.03	1.5 ± 0.4	3 ± 8
	6.38	35.4	0.057 ± 0.037	23 ± 13	0.80 ± 0.08	2.3 ± 1.2	18 ± 9
	15.03	83.4	0.120 ± 0.015	38 ± 4	0.85 ± 0.02	2.4 ± 0.2	33 ± 8
JPC BR2	2.53	14	0.054 ± 0.028	17 ± 8	0.75 ± 0.06	2.6 ± 1.1	12 ± 6
	9.31	51.6	0.083 ± 0.033	27 ± 10	0.78 ± 0.05	2.4 ± 1.0	21 ± 8
	11.67	64.7	0.103 ± 0.040	38 ± 9	0.77 ± 0.08	2.2 ± 0.8	27 ± 8

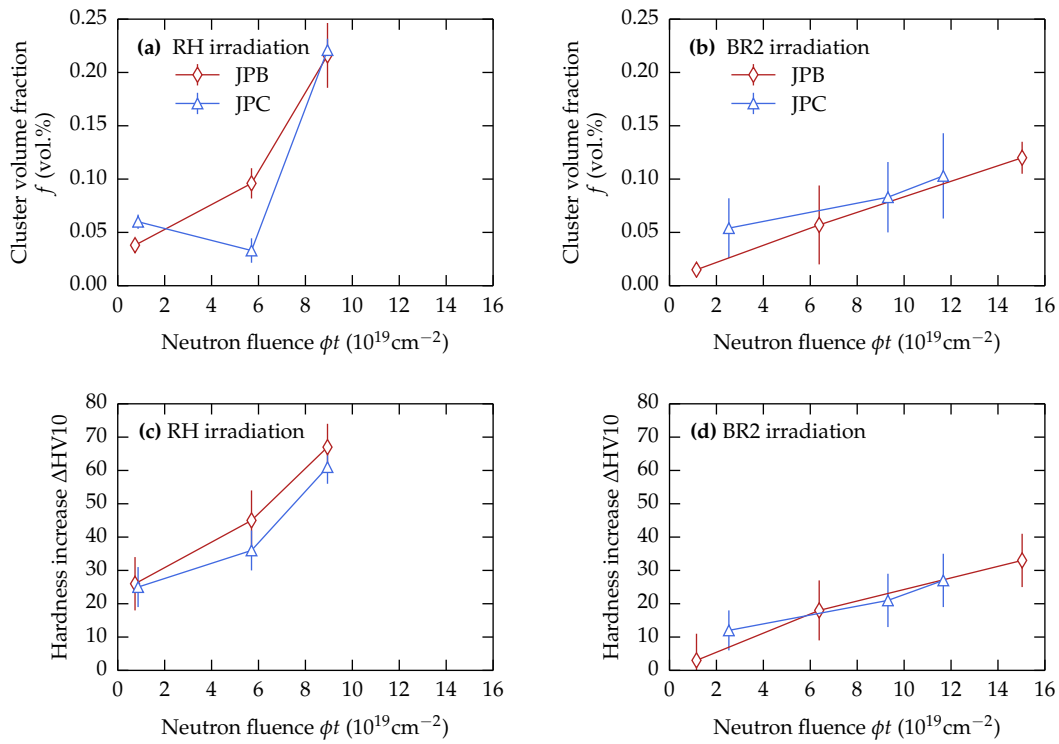


Figure 23: Irradiation-induced cluster-volume fraction f_v and hardness increase of materials JPB and JPC as a function of neutron fluence ϕt for both RH (a, c) and BR2 (b, d) irradiation. For visual guidance, samples of the same material are connected by straight lines.

4.3 LATE-BLOOMING EFFECT (APT)

Material JPC RH exhibits the most pronounced CoS. Therefore, samples of the unirradiated, the medium- and the high-fluence condition are selected for complementary APT investigations.

Four samples of the unirradiated reference condition of JPC material are investigated with the ECoWATAP and the LaWATAP devices. Several atomic layers on top and at the bottom of the recorded volume are removed prior to data analysis to avoid bias of composition due to oxidation- and tip-breaking effects. The three-dimensional reconstruction of an exemplary chosen sample volume, which is recorded with the ECoWATAP, is shown in Fig. 24. The elements, which tend to form clusters upon neutron irradiation, i.e. Mn, Ni, Si, Cu and P, are shown separately. Only 1 % of the Fe fraction is shown for illustration purposes.

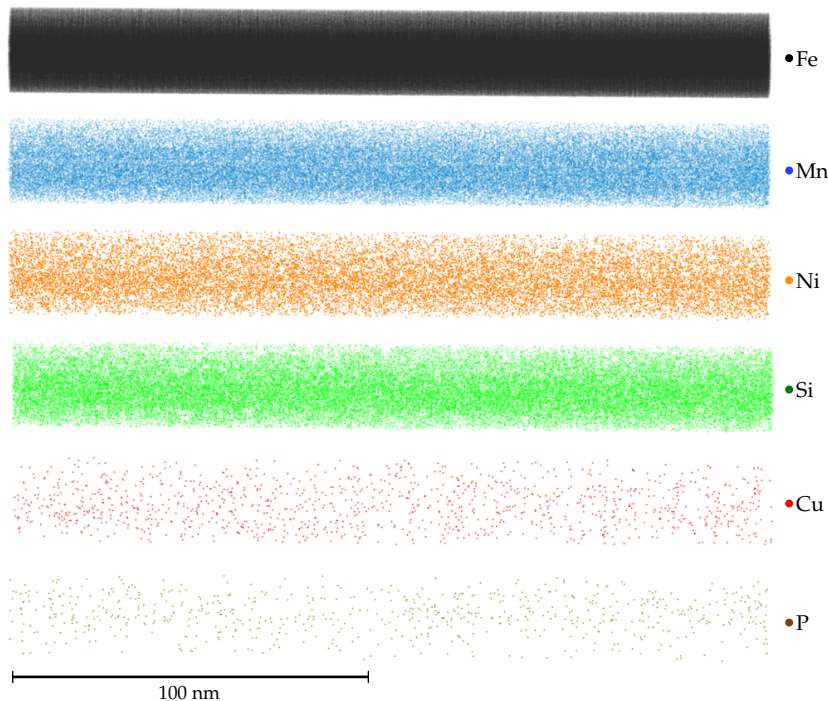


Figure 24: Three-dimensional element map of the non-irradiated reference material. Visually, the solute elements are distributed randomly in the sample volume, i.e. no clustering of elements appears. This is confirmed by a χ^2 test and the application of the iso-concentration algorithm for cluster detection.

Upon visual inspection of Fig. 24 the atoms of all elements appear to be randomly distributed in the sample volume. This impression is quantitatively underpinned by a statistical χ^2 test [27, 28]. Here, the frequency distribution of solute elements is compared to a perfectly random binomial frequency distribution. This gives an estimate of the randomness of the solute element distribution of atoms: The null hypothesis, that the solute elements are randomly distributed in the material, is met with a probability of $> 95\%$ in all non-irradiated reference measurements. How-

ever, since the χ^2 test can depend on the total size of the investigated sample volume [28], each reference measurement is additionally checked with the iso-concentration cluster-detection algorithm using the same parameter-set, which is also used for the irradiated samples. The cluster-detection algorithm reveals a total number of 11 clusters in the entirety of the reference samples (15 million ions in total). Considering that some clusters might already be randomly present prior to irradiation, their number density would be lower than $0.7 \cdot 10^{16} \text{ cm}^{-3}$. This corresponds to a lower detection limit of the cluster-volume fraction, f_v , of 0.004 vol.% at a typical cluster radius of 0.95 nm. Note that for SANS the lower detection limit is given with a similar value of about 0.005 vol.%.

The average chemical composition of all the reference samples is shown in the top row of Table 7. The uncertainties are calculated according to the square-root of number of atoms detected for each element (Poisson statistics).

Table 7: Chemical composition of material JPC RH in units of wt.%, for the unirradiated reference, the medium- and high-fluence condition derived from APT. The composition of the irradiated sample volumes are given separately for the whole bulk volume and the sub-volumes of clusters and matrix. The uncertainties, listed in the lines denoted with \pm , are derived from Poisson statistics.

Volume selection	Neutron fluence	Mn	Ni	Si	P	Cu	Mo	Cr	Al	C	Fe
Reference		1.031	0.562	0.311	0.0039	0.0069	0.341	0.145	0.0087	0.0013	97.59
	\pm	0.003	0.002	0.001	0.0001	0.0002	0.002	0.001	0.0002	0.0001	0.03
Bulk	Mid	1.614	0.509	0.319	0.0030	0.0070	0.361	0.167	0.0051	0.0055	97.01
		\pm	0.003	0.002	0.001	0.0001	0.0002	0.002	0.001	0.0001	0.0001
	High	1.339	0.626	0.318	0.0016	0.0068	0.243	0.125	0.0045	0.0070	97.33
		\pm	0.004	0.003	0.001	0.0001	0.0003	0.002	0.001	0.0002	0.0001
Clusters	Mid	8.958	6.643	2.226	0.1149	0.3813	1.530	0.384	0.0438	0.0195	79.70
		\pm	0.318	0.285	0.115	0.0286	0.0678	0.179	0.061	0.0165	0.0074
	High	8.083	7.938	2.120	0.0155	0.1331	0.420	0.223	0.0307	0.0137	81.02
		\pm	0.136	0.141	0.050	0.0047	0.0186	0.042	0.021	0.0058	0.0027
Matrix	Mid	1.625	0.504	0.317	0.0029	0.0069	0.362	0.167	0.0049	0.0053	97.01
		\pm	0.003	0.002	0.001	0.0001	0.0002	0.002	0.001	0.0001	0.0001
	High	1.268	0.601	0.295	0.0014	0.0061	0.242	0.120	0.0043	0.0073	97.46
		\pm	0.004	0.002	0.001	0.0001	0.0003	0.002	0.001	0.0001	0.0001

The APT reference measurements show a chemical composition similar to the one measured by means of ICP-MS, listed in Table 1. However, there are deviations in excess to the given uncertainties. These differences are to be expected: First, the uncertainties represent only errors from Poisson statistics, i.e. no experimental uncertainties are incorporated. Second, the material may exhibit heterogeneities at length scale larger than the typical dimensions of the probed APT samples. For instance, the lower Mn-level of the APT measurement can be accounted for with part of bulk-Mn being trapped in coarse $\text{Mn}_{0.6}\text{Fe}_{2.4}\text{C}$ carbides [20, 79].

In the following, the results regarding the irradiated samples are introduced. Two reconstructed sample volumes from the medium-fluence and the high-fluence samples are shown exemplarily in Figs. 25 and 26, respectively.

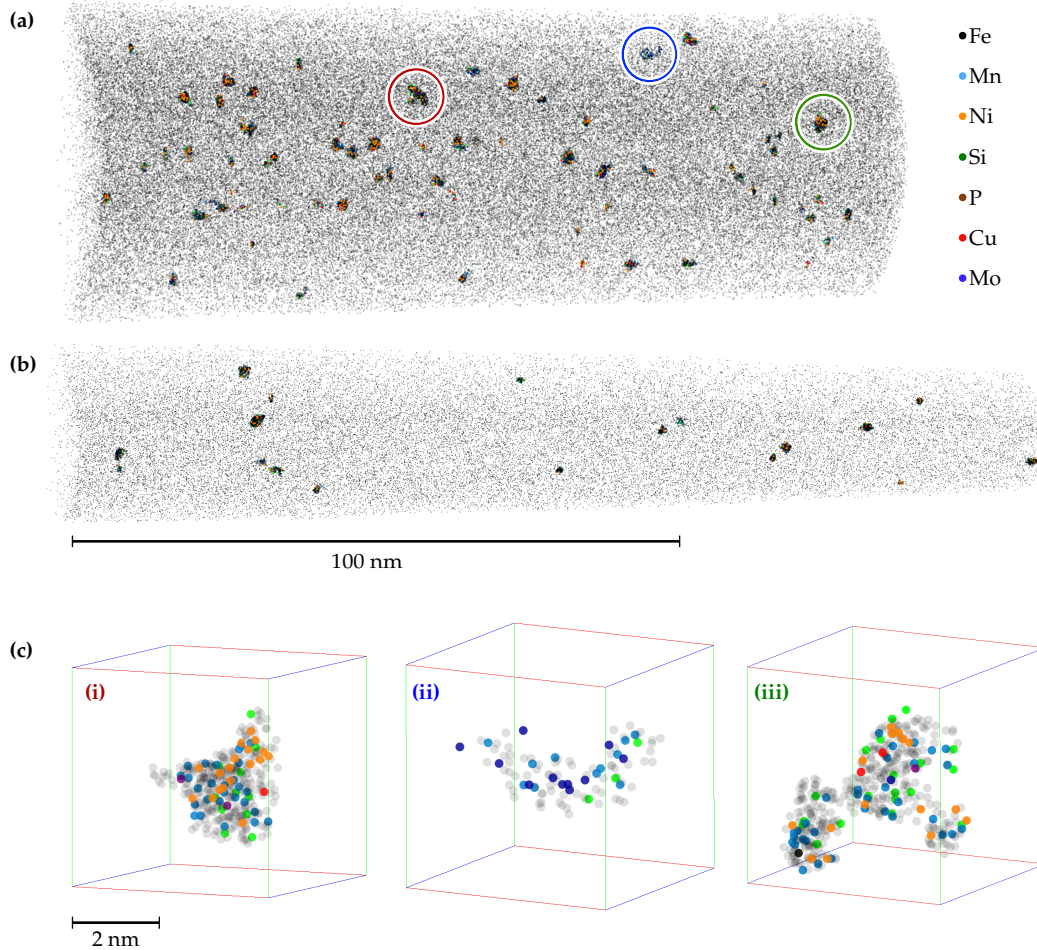


Figure 25: Reconstructed APT-sample volumes of the medium-fluence condition. The elements are color-coded according to the legend on the right. The measurements were performed with the LaWATAP device, (a), and the EcoWATAP device, (b). A magnified view of three clusters is shown in (c). The largest fraction of clusters is composed of mainly Mn, Ni, Si and partly with Cu. The clusters differ in shape: Mostly, they have a smooth shape and are compact, others, such as (ii) and (iii), are more ramified and/or half-torus shaped.

In both figures, the Fe atoms from the matrix are displayed semi-transparently for a clearer representation of the clusters. The clusters are identified by means of the iso-concentration algorithm introduced in Section 2.3.2. The concentration threshold of cluster elements, i.e. the sum of the concentrations of Mn, Ni, Si, P and Cu atoms is set to a value of $\rho_{CL} = 8.01$ at.% such that the difference between binomial frequency distribution and the frequency distribution of CL atoms yield a number of atoms equal to the one in clusters [80].

Clusters from the edge of the measured volume are manually removed to prevent bias in composition due to edge effects. The removed clusters are counted as half for the calculation of cluster-number density and volume fraction.

Numerous clusters are identified in both the medium-fluence and the high-fluence samples, as seen in Figs. 25 and 26 (a) and (b). A magnified view of three exemplary chosen clusters is shown in Fig. 25c: The majority of clusters are compact and spherical shaped with a smooth surface, as seen in (i). They are mainly enriched with Mn, Ni, Si and in some cases with Cu, P or Mo. Part of the clusters of the medium-fluence samples show a loose structure and appear to be more ramified. Their shape is similar to half a torus, which is shown in (ii) and (iii). While the larger part of the torus-like clusters (iii) are also enriched in Mn, Ni and Si, some of them, as the cluster depicted in (ii), do not contain any Ni atoms. These Ni-free clusters are mainly enriched in Mn and Si and, in some cases, Mo.

The samples from the high-fluence irradiation show a significantly higher number density, which is already apparent upon visual inspection of Figs. 25 and 26 (a) and (b). The magnification of some clusters, shown in Fig. 26 (c), reveals that they tend to have a smoother surface compared to the medium-fluence clusters. This might be due to the longer irradiation of the high-fluence samples which may lead to spherical clusters with a lower surface energy. Additionally, the volumes show the presence of several half-torus shaped clusters, as seen in (iii).

The chemical composition of the medium- and high-fluence samples are listed in Table 7, given separately for the complete bulk, the clusters and the matrix volume. It is important to note that the largest element fraction in clusters appears to be Fe, with a concentration of ≈ 80 at.% for both medium- and high-fluence clusters. It is numerously argued [81–83] that APT tends to overestimate the Fe content in clusters. However, the reasons for this apparent bias is an issue not well understood and still matter of debate. For different kinds of irradiated steels [82, 84], the origin for the overestimation of Fe in clusters has been accounted to ion-trajectory overlap and/or preferential evaporation, leading to a protrusion of matrix Fe to the position of cluster atoms on the detector. However, no such effect is reported from the atom-probe community for Mn-Ni rich clusters found in low-Cu RPV steels. Part of the reason is the unknown evaporation fields of chemically complex clusters forming in RPV steels. Nevertheless, based on the findings from SANS [82, 83], TEM [85] experiments and thermodynamic considerations [7], it is reasonable to assume an overestimation of the Fe fraction determined by APT. We are therefore not going to consider the Fe content any further in the present work.

To estimate the increase of concentration of each element in the clusters, it is convenient to introduce enrichment factors, calculated from the ratio of the element concentration in the clusters and in the bulk material. The enrichment factors for both irradiations are listed in Table 8.

The enrichment of Mn, Ni and Si are almost identical between the medium- and the high-irradiation. The elements with a lower concentration, i.e. P, Cu and Mo, show a higher enrichment in the clusters of the medium fluence samples. However,

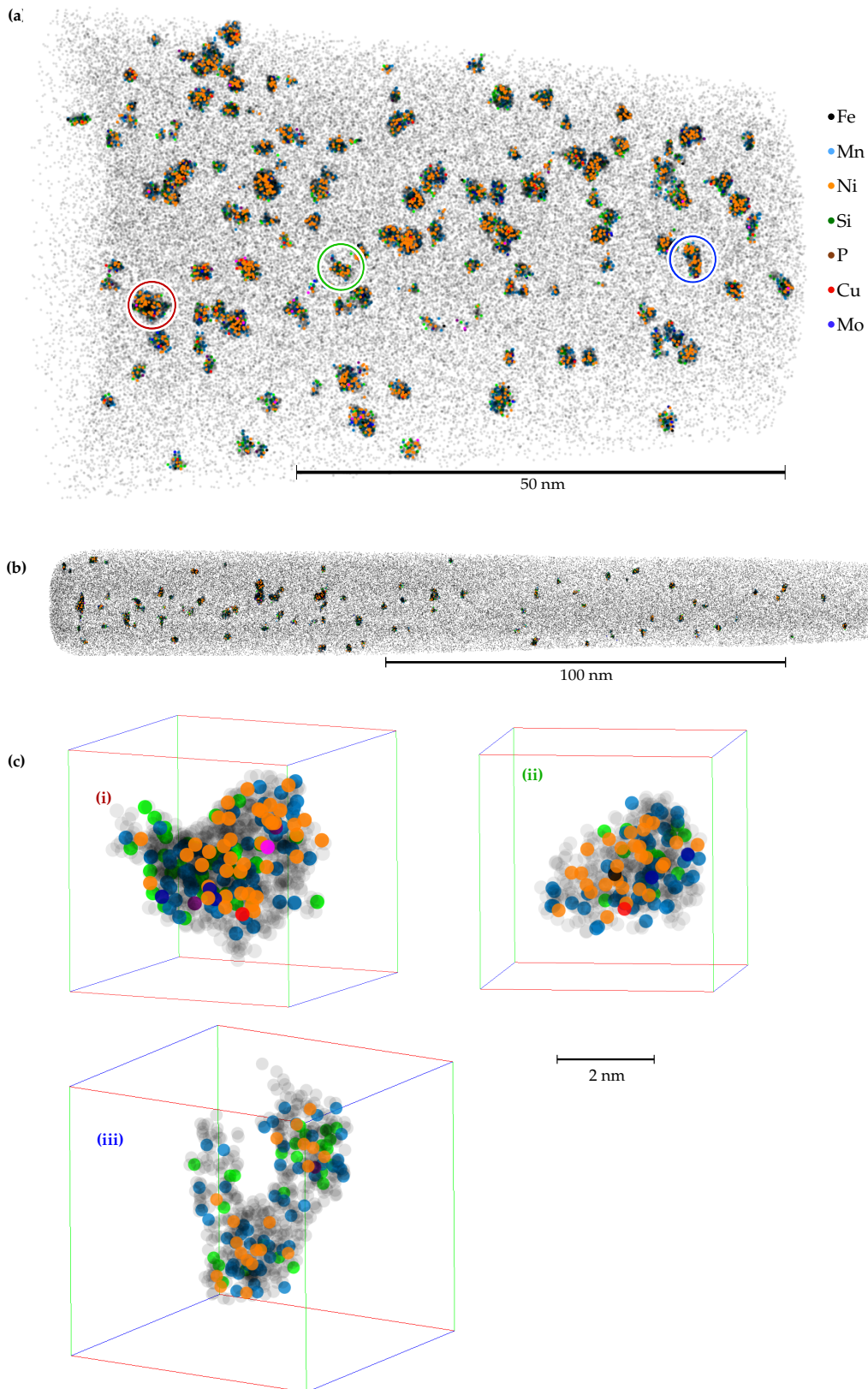


Figure 26: Reconstructed APT-sample volumes of the high-fluence condition. The elements are color-coded according to the legend on the right. The measurements were performed with the LaWATAP device, (a), and the FlexTAP device, (b). A magnified view of three clusters is shown in (c). The clusters are composed of mainly Mn, Ni, Si. Cu is a minor constituent.

Table 8: Enrichment factors of each element in the clusters: The factors are calculated from the ratio of cluster-element concentration and the bulk-element concentration.

Fluence	Mn	Ni	Si	P	Cu	Mo
Medium	5.6 ± 0.2	13.0 ± 0.6	7.0 ± 0.4	38 ± 10	54 ± 10	4.2 ± 0.5
High	6.0 ± 0.1	12.7 ± 0.2	6.7 ± 0.2	10 ± 3	20 ± 3	1.7 ± 0.2

it is important to note that the low absolute concentration of these elements, as seen in Table 7, significantly increases the error margins of the factors.

The cluster-size distributions are plotted in Fig. 27. The clusters of the high-fluence samples show a significantly higher number density and volume fraction than the ones of medium-fluence samples. Moreover, the mean cluster radius is slightly larger for the high-fluence samples. The lower number of clusters recorded for the medium fluence samples leads to a less smooth size distribution compared to the one from high-fluence samples. Nevertheless, the shape of the size distributions obtained by APT are in good agreement with the size distributions from SANS, Fig. 21d. The positions of the peaks are similar, although the APT size distribution appears to be wider and of larger fluctuations, most likely due to the much lower sample volume investigated by APT.

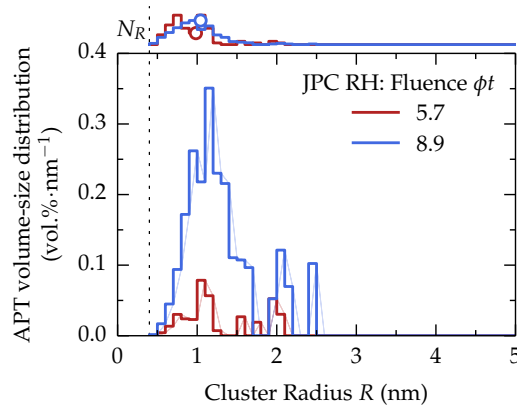


Figure 27: APT Cluster-size distribution of JPC RH for the medium- and the high-fluence condition. Both cluster populations are of similar-sized clusters, however, the high-fluence condition shows a higher cluster-number density and volume fraction.

The parameters of the cluster population, which are derived from the size distributions in Fig. 27 by integrating over the radius increment, are listed in Table 9 with the corresponding results from the SANS measurements. The mean cluster radii, \bar{R} , from APT are slightly larger than the one determined by SANS. The number density shows the opposite trend. The cluster-volume fraction is, however, strikingly similar between both methods. The given A ratio for the APT measurements is calculated from the composition of clusters and the corresponding scattering-length densities. No significant trend from medium- and high-irradiation or between APT and SANS is found for the A ratios.

Table 9: The parameters of the cluster population of material JPC RH determined by APT and SANS: f_v , volume fraction, N , number density, \bar{R} , mean radius. The A ratio of the APT measurement is calculated with the chemical composition of the clusters and the corresponding scattering-length densities.

Method	ϕt (10^{19} n/cm 2)	ϕ (10^{12} n/cm 2 /s)	f_v (vol.%)	N (10^{16} cm $^{-3}$)	\bar{R} (nm)	A ratio
APT	0.867	0.1267	–	–	–	–
	5.702	2.224	0.047 ± 0.015	14 ± 2	0.93 ± 0.09	1.7
	8.941	3.487	0.227 ± 0.050	56 ± 4	0.99 ± 0.07	1.8
SANS	0.737	0.1077	0.060 ± 0.006	24 ± 2	0.81 ± 0.02	4.8 ± 2.2
	5.702	2.224	0.033 ± 0.011	9 ± 1	0.91 ± 0.10	1.9 ± 0.4
	8.941	3.487	0.221 ± 0.011	121 ± 3	0.73 ± 0.01	2.2 ± 0.3

The fluence dependence of the cluster-volume fraction determined by APT and by SANS is depicted in Fig. 28. The CoS of the cluster-volume fraction found by means of SANS is confirmed by the APT measurements. The differences between the cluster volume fraction from APT and SANS is well within the given uncertainties.

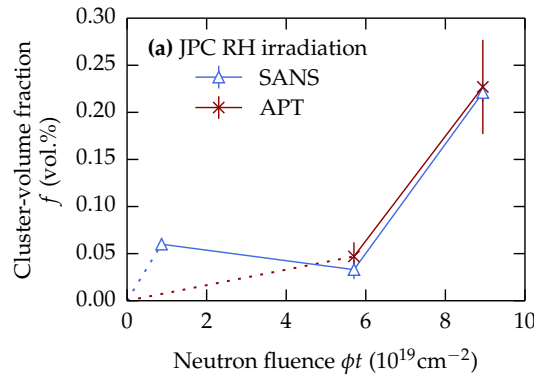


Figure 28: Evolution of the cluster-volume fraction with neutron fluence of material JPC RH determined by means of SANS and APT. The cluster-volume fractions determined by both techniques are strikingly similar.

The cluster composition renormalized to zero Fe fraction is shown in Fig. 29 (a) and (b) as a function of the size of the clusters for the medium- and the high-fluence samples, respectively. The medium-fluence samples show a larger fluctuation of composition with size than the high-fluence condition. This is due to a lower number of clusters, i.e. less statistics, in the case of the medium-fluence samples. The main cluster constituents are Mn, Ni and Si, with a ratio of about 3:2:1 and 2:2:1 for the medium- and high-fluence samples, respectively. For the medium-fluence samples the Mo content increases slightly at the expense of the Ni content with increasing cluster radius. The contribution of Cu to the clusters appears to be bigger on average for the medium-irradiation sample.

The main cluster constituents are Mn, Ni and Si. There is an ongoing debate in the literature whether the clusters found in irradiated low-Cu RPV steels are actually stable thermodynamic phases. One of the most prominent candidates is the ternary

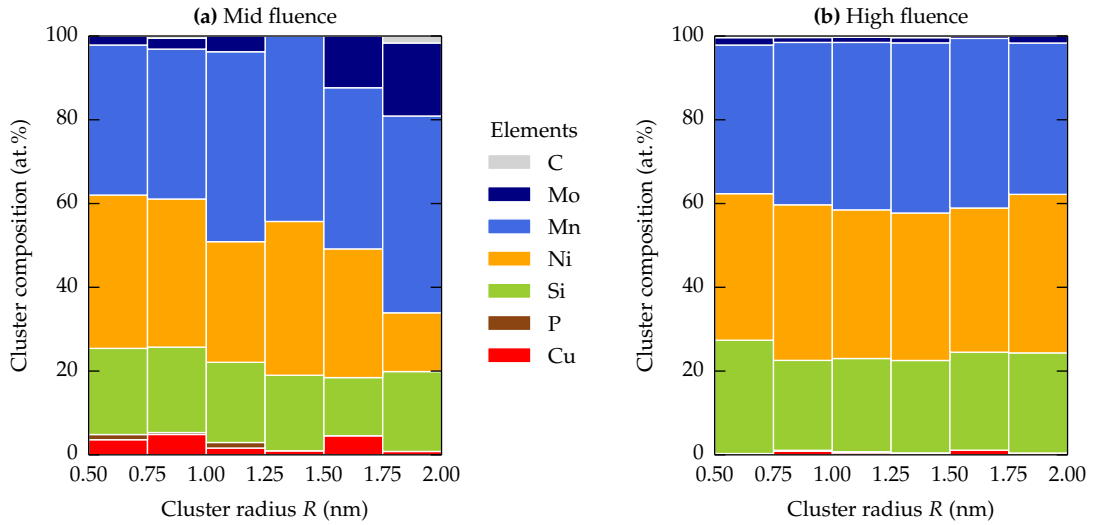


Figure 29: Cluster composition for material JPC RH for (a) medium- and the (b) high-fluence samples as a function of radius between 0.5 and 2.0 nm. The high-fluence condition shows an overall constant MnNiSi ratio of 2:2:1 with size. While the ratio is similar for small clusters of the medium-fluence condition, the average Mo level increases at the expense of a lower average Ni content. Cu seems to play a more important role for the medium fluence condition.

G phase [86], $\text{Mn}_6\text{Ni}_{16}\text{Si}_7$. To investigate the composition of the present clusters in the corresponding phase diagram the composition of the clusters are renormalized such that $\text{Mn} + \text{Ni} + \text{Si} = 100\%$ and plotted in Fig. 30. Each disk represents one cluster and the size of the disks corresponds to the size of the clusters. The G phase renormalized to 100 amounts to $\text{Mn}_{21}\text{Ni}_{55}\text{Si}_{24}$. There is no significant excess of clusters present in this particular phase region. In fact, the cluster compositions show a large scatter of about 20% for each of the elements. Moreover, no systematic variation of composition and size is evident from this representation. Note that Ni-free clusters are significantly more numerous than Si-free or Mn-free clusters.

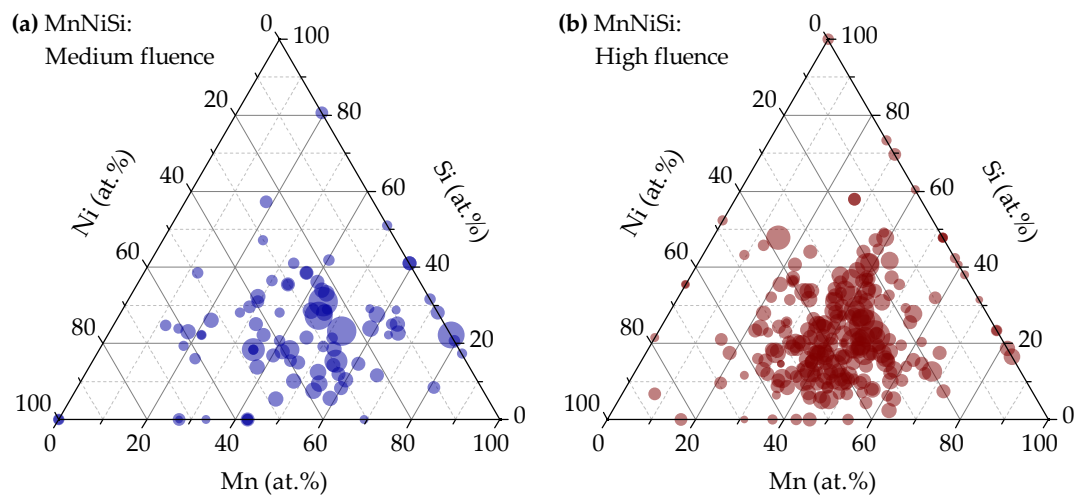


Figure 30: Ternary plot of the cluster composition considering only the Mn, Ni and Si concentrations. (a), clusters of medium-fluence samples and (b), clusters of the high-fluence samples. Each cluster is represented by a disc with a radius proportional to the cluster radius.

DISCUSSION

5.1 FLUX EFFECTS

5.1.1 *Approach*

It was highlighted in Section 4.1 that certain characteristics of the cluster population show a significant dependency on the neutron flux. In particular, it was observed that the cluster radius tends to be smaller for the higher flux with all the other material and irradiation parameters kept constant within one flux pair. Following the idea that the mechanical properties are determined by the nanostructure of the material (at all length scales), one would also expect a flux dependence of the mechanical properties. However, no significant flux effect on the hardness was observed in the results presented in Section 4.1. The underlying causes for this discrepancy are elaborated in this section.

The strategy followed here, also published in [87], is to apply dedicated models of nanostructure evolution and hardening to the set of observations and to compare the trends with the experimental findings of this work. While this is straightforward within each pair of samples irradiated at different flux up to the same fluence, the situation is obscured from pair to pair by superimposed dependencies on other factors such as fluence and composition. In order to exploit the whole set of flux pairs available, it is, therefore, necessary to first separate the flux effect from other influence factors such as fluence and composition. This will be done in Section 5.1.2 by means of normalization of the cluster parameters to the low-flux condition. Two cluster evolution models will be introduced in Section 5.1.3 and linked with hardening models presented in Section 5.1.4. We are then prepared to compare the model observations with the experimental findings and to draw conclusions about the mechanisms and consequences of flux effects.

5.1.2 *Normalization of cluster parameters*

Differences in neutron flux result in different properties of the irradiation-induced cluster population: Within one flux pair, higher neutron fluxes lead to more clusters, which are smaller in size. The volume fraction does not change or decreases only slightly, depending on the flux pair.

The effect of the neutron flux on the parameters of the cluster population is in some cases stronger, as for \bar{R} , in some cases weaker, as for f_v , than effects originating from other factors, such as

- the neutron fluence, ϕt ,

- the irradiation temperature, T_{irr} ,
- the fractions of residual and alloying elements in the bulk material, $f(\text{Cu, Mn, Ni, Si, P, } \dots)$,
- the manufacturing procedure and heat treatment, resulting in differences in phase morphologies and grain sizes, etc.

All these factors are coupled and have an intricate impact on the nanostructure emerging upon irradiation. A full elaboration of the interplay of this multitude of material and irradiation parameters is beyond the scope of this work. Such broad-based studies are rather subject to collaborative international research projects to date.

For the present purpose, it is meaningful to eliminate the pair-to-pair variation of neutron fluence, irradiation temperature, composition and nanostructure by way of pairwise normalization of the cluster parameters to the respective low-flux value. In doing so, the insight that the low-flux conditions belong to the flux-independent sink-dominated regime (to be introduced later) is utilized. This procedure ensures comparability of the trends covered by the whole set of experimental data with the model trends.

The normalized cluster radii and volume fractions are plotted as a function of neutron flux in Fig. 31. In the low-flux region of about $\phi = 0.05 \dots 0.25 \cdot 10^{12} \text{ n cm}^{-2} \text{ s}^{-1}$, no significant flux dependency of the normalized cluster radii is visible in Fig. 31a. For higher fluxes, a decrease in radius becomes prominent. This is most pronounced for material BBA, which was irradiated with highest neutron flux in the present data set. A decrease in cluster size of about 50 % from the low- to the high-flux regime is observed.

A similar, but less pronounced trend is visible for the normalized cluster-volume fraction in Fig. 31b: The effect of flux is weak or insignificant in the low-flux regime of up to $\phi \approx 0.25 \cdot 10^{12} \text{ n cm}^{-2} \text{ s}^{-1}$ and increases in strength for higher fluxes.

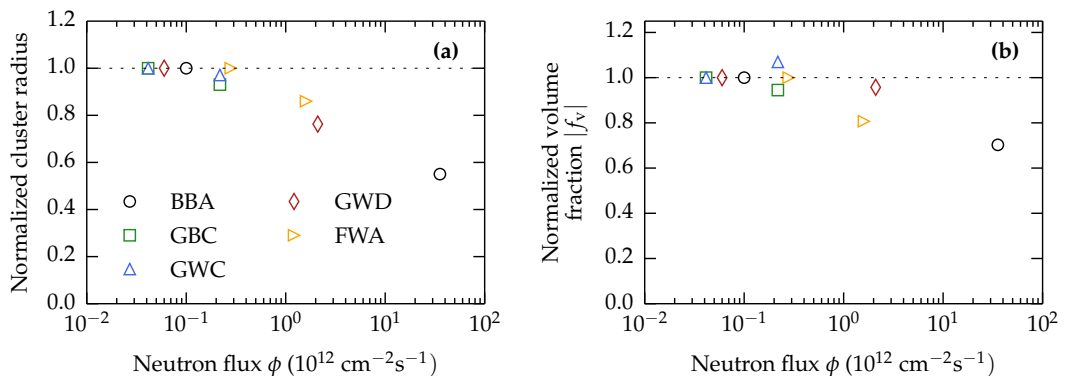


Figure 31: Normalized cluster characteristics as a function of the neutron flux, showing (a) the radius and (b) the volume fraction. For each pair, the low-flux value is taken as reference and shifted to the base line. The high-flux value is multiplied by the same factor.

In the following section two cluster-evolution models, based on deterministic growth and coarsening, will be introduced and compared with the experimental data. The comparison is focused on the flux dependence of the normalized mean cluster radius, $|\bar{R}(\phi)|$ and the corresponding volume fraction $|f_v(\phi)|$. The normalized cluster-number density, $|N(\phi)|$, relates to the radius and volume fraction as a function of flux such that

$$|N(\phi)| = \frac{3f_v(\phi)}{4\pi\bar{R}(\phi)^3}. \quad (48)$$

Therefore, $|N(\phi)|$ does not need to be addressed separately within the consideration of the models.

5.1.3 Models of cluster evolution

5.1.3.1 Deterministic growth

Odette suggested [11, 88] a model addressing the evolution of irradiation-induced clusters as a function of neutron flux and fluence. The model is based on the diffusion-limited growth of spherical precipitates and the application of a Johnson-Mehl-Avrami-Kolmogorov (JMAK)-type approach [40, 89–94] to the evolution of Cu-enriched clusters. According to this model, the diffusion coefficient of the clustering solute is replaced by its radiation-enhanced diffusion (RED) coefficient, D^* . The volume fraction of clusters, f_v , increases as a function of time,

$$f_v(t) \approx f_{\max} \left(1 - \exp \left[-k_1 (D^* t)^{3/2} \right] \right), \quad (49)$$

where the maximum volume fraction, f_{\max} , is reached asymptotically at large t , when all the matrix Cu above the solubility limit in Fe is consumed by Cu-enriched clusters. The parameter k_1 is a factor of the dimension of a concentration [88]. Similarly, the mean cluster radius increases with time [94–96] according to

$$\bar{R}(t) \propto (D^* t)^{1/2}. \quad (50)$$

The RED coefficient, D^* , is expressed for vacancy-assisted diffusion in the simplest approximation [14] as

$$D^* = \frac{C_{v,ss}}{C_{v,eq}} D_{th}. \quad (51)$$

The parameters $C_{v,ss}$ and $C_{v,eq}$ are the steady-state vacancy concentration in the solid under irradiation and the equilibrium vacancy concentration under the absence of irradiation, respectively. D_{th} is the diffusion constant of monomers in the matrix. Each parameter in Eq. (51) depends on the temperature.

The steady-state vacancy concentration as a function of neutron flux is obtained from a system of two coupled partial differential equations [97] for both vacancies (v) and interstitials (i), $m = i, v$, with

$$\nabla \cdot \left(D_m \nabla C_m + \frac{D_m C_m}{k_B T} \nabla U_m + G_m - 4\pi r_0 (D_i + D_v) C_v C_i - K_m C_m \right) = \frac{\partial C_m}{\partial t} . \quad (52)$$

U_m are the interaction energies between the point defect and sink, k_B is the Boltzmann constant, and K_m represents the reaction-rate constant of the type of monomer. The radius of the recombination radius is denoted by r_0 . In the space independent steady-state approximation, Eq. (52) becomes

$$G_m - \frac{4\pi r_0}{V_{\text{at}}} (D_v + D_i) \cdot C_v C_i - K_m C_m = 0 , \quad (53)$$

where V_{at} is the atomic volume of bcc-Fe. Both Eqs. (52) and (53) include the monomer concentrations C_v and C_i . The generation term, G_m , is identical for vacancies and interstitials and proportional to the neutron flux. Combining Eq. (53) for the case of interstitials, $m = i$, and the case of vacancies, $m = v$, yields the steady-state vacancy concentration

$$C_{v,ss} = (\sqrt{2} + 1) C_t \left(\sqrt{1 + \frac{\phi}{\phi_t}} - 1 \right) . \quad (54)$$

The parameter ϕ_t marks the transition between the sink-dominated lower-flux regime and the recombination-dominated higher-flux regime [88, 98], where C_t is the steady-state vacancy concentration at the transition flux ϕ_t . Finally, the combination of Eqs. (49) to (54) and the substitution of time by the ratio of fluence and flux yields the flux dependence of both the mean radius and the cluster-volume fraction

$$\bar{R}(\phi) \propto \left(\frac{2\phi_t}{\phi} \sqrt{1 + \frac{\phi}{\phi_t}} - 1 \right)^{1/2} \quad \text{and} \quad (55)$$

$$f_v(\phi) \propto 1 - \exp \left(-k_2 \left[\frac{2\phi_t}{\phi} \sqrt{1 + \frac{\phi}{\phi_t}} - 1 \right] \right)^{3/2} . \quad (56)$$

The right-hand side of Eqs. (55) and (56) are normalized such that the values of radius and volume fraction approach 1 in the low-flux regime, where radius and volume fraction are asymptotically independent of flux.

It is interesting to note, that in both Eqs. (55) and (56), the evolution of clusters with flux depends on a parameter proportional to net-mean RED distance, $\langle \delta^* \rangle \propto \sqrt{D^* t}$. For fluxes $\phi \gg \phi_t$, the parameter $\langle \delta^* \rangle$ decreases with $\phi^{-1/2}$. The flux-dependence of

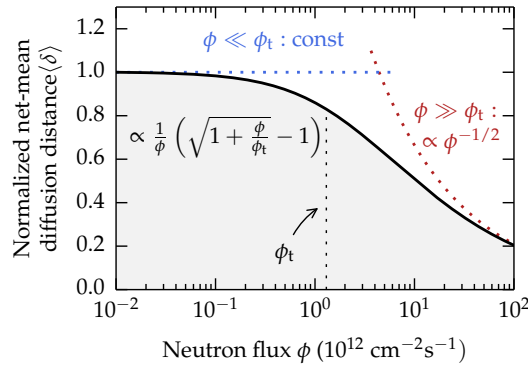


Figure 32: Evolution of the net mean RED distance $\langle \delta^* \rangle^2$ with neutron flux, ϕ , according to rate-theory considerations in [98] and Eqs. (53) to (55), solid black line. The blue and red dotted curves represent the asymptotic behavior for fluxes $\phi \ll \phi_t$ and $\phi \gg \phi_t$, respectively, where ϕ_t is the transition flux.

$\langle \delta^* \rangle$ and the asymptotic behavior in the sink-dominated as well as the recombination-dominated regime are plotted for a transition flux of $\phi_t = 1.30 \cdot 10^{12} \text{ n cm}^{-2} \text{ s}^{-1}$ in Fig. 32.

In a simplified framework, the formation and evolution of (Cu-enriched) clusters consist of three stages: nucleation, deterministic growth and coarsening. The relationships introduced above are related to the growth stage. However, it is not a priori obvious in particular situations, to what extent the coarsening stage is already operative. Moreover, there is a continuous transition from growth to coarsening [99] and both coarsening and growth may be coupled with one another [100] or operate independently in distinct subsystems, e.g. the Cu subsystem and the Ni subsystem, of the whole system.

5.1.3.2 Coarsening

Coarsening, also referred to as Ostwald ripening, is treated with the Lifshitz-Slyozov-Wagner (LSW) theory [101, 102]. The reference to Ostwald ripening might be debatable in the context of a driven system [103] – here a system under neutron irradiation. However, although some of the assumptions underlying the LSW theory might not be fulfilled, the finding of a weakly flux-dependent or, in individual cases, flux-independent volume fraction formally justifies the prospective application of the expressions derived for particle coarsening to the cluster radii observed here. This is particularly reasonable for binary Fe-Cu alloys [51], for low-Ni/High-Cu RPV steels [104] and for the Cu-subsystem in arbitrary Ni- and Cu-bearing RPV steels [105].

According to the LSW theory, the asymptotic growth rate of the mean particle radius, \bar{R} , and the long-term temporal change of the volume fraction, f_v , of clusters for diffusion-limited growth are characterized [106] by

$$\bar{R}(t) \propto (D^*t)^{1/3} \quad \text{and} \quad (57)$$

$$f_v(t) = \text{const} , \quad (58)$$

which, as a function of flux, transforms into

$$\bar{R}(\phi) \propto \left(\frac{2\phi_t}{\phi} \sqrt{1 + \frac{\phi}{\phi_t} - 1} \right)^{1/3} \quad \text{and} \quad (59)$$

$$f_v(\phi) = \text{const} . \quad (60)$$

Eq. (59) is normalized to approach a value of 1 for the case of $\phi \rightarrow 0$.

5.1.3.3 Model comparison

In the following, the two models introduced above, i.e. deterministic growth and coarsening, will be compared with the normalized cluster radii and volume fractions experimentally obtained within this work (Fig. 31). Additionally, results from the published literature [107, 108] are added to the data set to improve statistics. The additional data were gained by means of APT, which was shown to produce results largely consistent with SANS results except for the Fe fraction in clusters [82]. Contrary to the present study, no error margins are given in references [107, 108]. One data point was removed from the additional data set as an obvious outlier.

Fig. 33 shows the cluster radii and volume fractions from this work and references [107, 108], normalized according to Section 5.1.2. The models for deterministic growth, Eqs. (55) and (56), as well as coarsening, Eqs. (59) and (60), are fitted to the normalized cluster-radii and cluster-volume fractions.

Assuming coarsening according to Eq. (59) as the underlying cluster-evolution model, a transition flux of $\phi_t = (0.51 \pm 0.10) \cdot 10^{12} \text{ n cm}^{-2} \text{ s}^{-1}$ is determined from the fit (Fig. 33a, dotted line) to the normalized cluster radii, which includes data from both the present investigation and from literature [107, 108]. This value of ϕ_t compares well with the estimates of the transitions fluxes of $0.3 \cdot 10^{12} \text{ n cm}^{-2} \text{ s}^{-1}$ and $0.7 \cdot 10^{12} \text{ n cm}^{-2} \text{ s}^{-1}$ reported in [98, 109].

For deterministic growth, represented by the solid lines in Fig. 33a, a transition flux of $\phi_t = (1.30 \pm 0.20) \cdot 10^{12} \text{ n cm}^{-2} \text{ s}^{-1}$ is found for the fit of the normalized cluster radii to Eq. (55). This value is still reasonably close to the values reported in [98, 109]. Unfortunately, the difference in the quality of the fit for the deterministic growth and coarsening is too small to favor one model over the other.

The situation is different for the volume fraction, Fig. 33b. For coarsening, a flux-independent cluster-volume fraction is predicted. For deterministic growth, a value of $k_2 = (2.40 \pm 0.50)$ for the dimensionless parameter in Eq. (56) with a fixed transition flux of $\phi_t = 1.30 \cdot 10^{12} \text{ n cm}^{-2} \text{ s}^{-1}$ gives the best fit and a valid representation of the experimental data within the error margins. It is, therefore, reasonable to assume that deterministic growth is indeed an appropriate model to describe the nanostructural evolution of the cluster population with varying flux at constant fluence. Ostwald ripening can be excluded to be the dominant mechanism of cluster evolution. It remains to be discussed if and how the evolution of the cluster population can represent the findings of mechanical property changes.

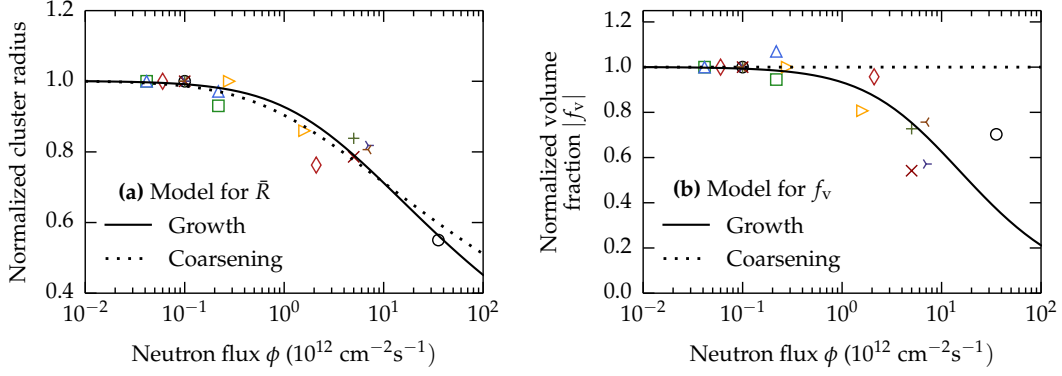


Figure 33: Normalized cluster characteristics as function of the neutron flux. For each pair, the low-flux value is taken as references and shifted to the base line. (a) The cluster radii were fitted with Eqs. (55) and (59) for deterministic growth and coarsening. Similarly, the volume fractions were fitted with Eqs. (56) and (60). Data from [107, 108] is indicated by the open markers.

5.1.4 Models of hardening

The defect-solute clusters (i. e. CRCs, MNCs and hybrid forms depending on the alloy composition) characterized by means of SANS give rise to hardening and embrittlement. Several models were proposed in the literature and expressions were derived to relate hardening with the characteristics the cluster population. These include the dispersed-barrier (DB) hardening model [110] in the simplest version, Eq. (61), and in the advanced version according to Bacon, Kocks and Scattergood (BKS) [111], Eq. (62), the Russel-Brown (RB) model [11, 112], Eq. (63), and the Friedel-Kroupa-Hirsch (FKH) (64) model [113–115].

$$\text{DB: } \Delta\sigma_y = \alpha M G b \sqrt{N d} \quad (61)$$

$$\text{BKS: } \Delta\sigma_y = \beta \frac{M G b}{2\pi L} \left[\ln \left(\frac{L}{b} \right) \right]^{-1/2} \left[\ln \left(\frac{d'}{d} \right) + 0.7 \right]^{3/2} \quad (62)$$

$$\text{with } L = \frac{1}{\sqrt{N d}} \quad \text{and} \quad d' = \frac{L d}{L + d}$$

$$\text{RB: } \Delta\sigma_y = \frac{\gamma M G b}{L} \left\{ 1 - \left[1.0935 - 0.0579 \ln \left(\frac{d}{b} \right) \right]^2 \right\}^{3/4} \quad (63)$$

$$\text{with } L = \frac{\sqrt{\pi}}{2} \frac{d}{\sqrt{f_v}} \quad \text{or} \quad L = \frac{1}{\sqrt{N d}}$$

$$\text{FKH: } \Delta\sigma_y = \delta M G b N^{2/3} \cdot d \quad \text{with} \quad \delta = 1/8 \quad (64)$$

Here, $M = 3.06$ is the Taylor factor [115], $G = 83$ GPa the shear modulus and $b = 0.248$ nm the Burgers vector [112]. In Eq. (61), $\alpha = \cos(\theta/2)$ is the classical obstacle strength with the critical cusp angle, θ , of the dislocation segments pinned by an obstacle. In Eq. (62), $\cos(\theta/2)$ is already included via the second square bracket. However, a dimensionless correction factor β is formally introduced. Details can be found in the associated references. For Eqs. (63) and (64) the parameterizations according to references [111, 112], respectively, are used. These are appropriate for Cu precipitates in Fe. The diameter of the obstacles, d , will be equated below with $2\bar{R}$.

It is interesting to note that the curly bracket expression in Eq. (63) can formally be interpreted as a size-dependent obstacle strength, α , according to Eq. (61). However, the obstacle strengths according to Eqs. (61) and (62) are independent of the cluster size but are included in square-bracket terms.

A simple proportionality with the square-root of the cluster-volume fraction, without any dependency on cluster size, is often reported in the literature, e.g. [13, 51]. However, this “rule of mixture” is dimensionally incorrect for dislocation dynamics and will therefore not be included in this comparison.

Two strategies are used consecutively to evaluate the hardening expressions according to Eqs. (61) to (64) with respect to their applicability in the present cases:

HARDENING EVOLUTION WITH FLUX: The first approach is to express the right-hand sides of Eqs. (61) to (64) as functions of the flux based on the equations derived and parameters fitted for deterministic growth. Coarsening is excluded in this comparison since it is in conflict with the measured volume fractions, as seen in Fig. 33. The resulting flux dependencies of hardening are plotted in Fig. 34. The yield-stress increase is normalized such as to approach unity for the flux-independent sink-dominated low-flux regime. The grey-shaded area highlights the regions of investigated neutron fluxes and measured hardness changes.

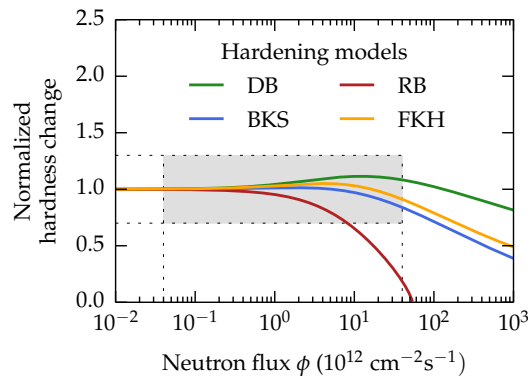


Figure 34: Comparison of the flux dependence of hardening models for deterministic growth. The grey-shaded area indicates the observed ranges in neutron flux and hardness change.

The curves of the hardening models plotted in Fig. 34 indicate that

- Each of the models predicts a flux dependence of hardening. An extension of the covered flux range towards higher fluxes and/or a reduction of the scatter of hardness would allow flux effects on hardening to be resolved.
- RB hardening shows a flux dependency of hardening larger than the observed scatter band of the hardness changes. Therefore, it can be excluded in the further considerations.
- Three hardening models, namely DB, BKS and FKH, show a flux dependence well within the measured range of hardening data.
- Both the BKS- and FKH-hardening models are nearly indistinguishable.

It is unambiguous that flux effects on the nanostructure do exist. Then again, these changes do not propagate to significant changes in the mechanical properties. From the viewpoint of the proposed models, this is comprehensible as the changes in cluster radius and number density partly cancel each other out in Eqs. (61) to (64) and thus, diminish an impact on the mechanical properties in the covered flux range. Moreover, the models DB, BKS and FKH predict a weak and non-monotonic dependence on flux, which makes it difficult to resolve a trend of the measured hardness change. For the same reason, it is also difficult to identify the most favorable hardening model among DB, BKS and FKH. However, a trial based on the correlation of predicted and measured hardness change will be undertaken below.

YIELD STRESS COMPARISON: The second approach is based on the correlation of measured yield-stress increase and the experimentally derived values of the hardening expression on the right-hand side of Eqs. (61) to (64). This approach will be used to rule out inappropriate hardening expressions for the present application. The advantage of this methodology is that, although flux variations and flux-related cluster-size variations are included in the data sets, flux itself drops out from the analysis. In this context, it is important to recall that the cluster size is mainly governed by flux. Therefore, this data set is potentially well suited to discriminate between hardening expressions containing cluster size as a parameter.

Unfortunately, the yield-stress increase is not available for all materials investigated in this work (see Table 3). Moreover, tensile and SANS samples are often from different locations in the material and were exposed to slightly different conditions in the irradiation experiment. In order to minimize scatter due to material inhomogeneity and minor differences in the irradiation conditions, it is, therefore, decided to perform the present analysis on the basis of the Vickers hardness increase, measured using the SANS samples after completion of the respective SANS experiments. According to Tabor [116] the Vickers hardness of elastic ideally plastic materials expressed in SI units is approximately three times the yield stress. This relationship was tested for irradiated RPV steels where both Vickers hardness and yield-stress increase data were available.

The comparison of the yield-stress increases calculated from hardness measurements versus the yield-stress increases calculated from the hardening models based on measured cluster parameters is shown in Fig. 35.

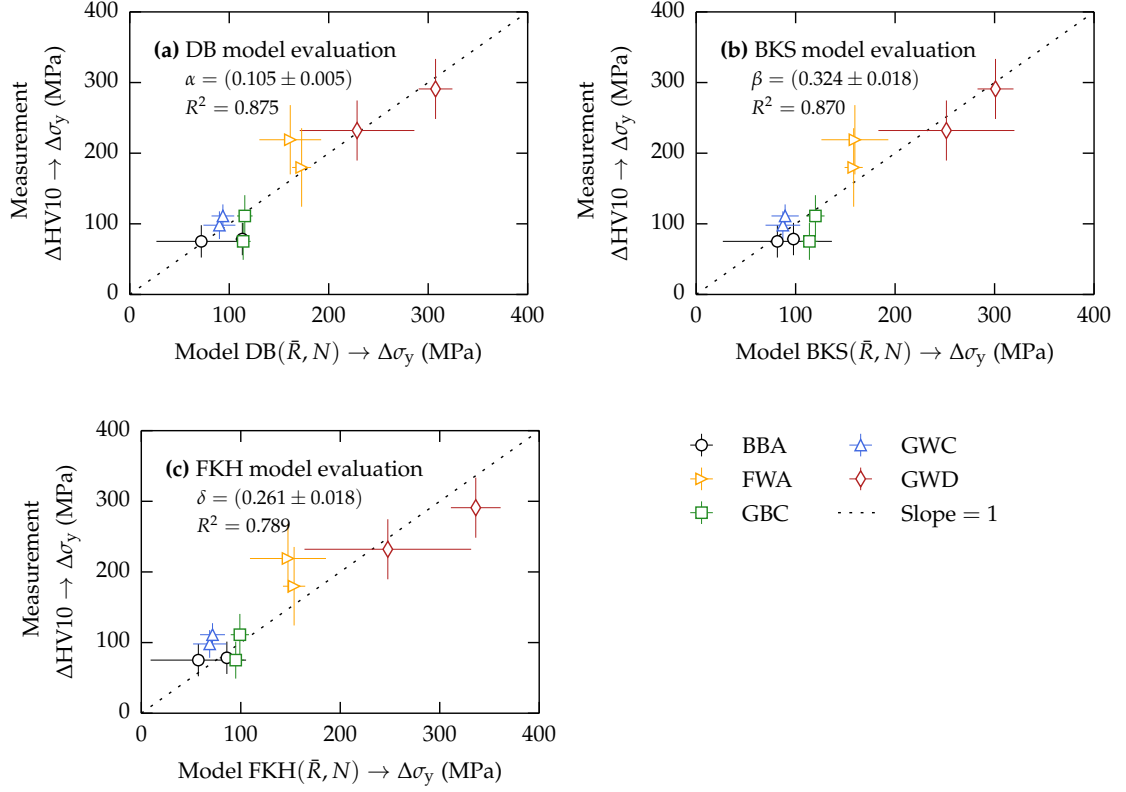


Figure 35: Comparison of yield-stress increase determined from the conversion of hardness-experiment data, y -axis, versus yield-stress increase predicted by the different hardening models, x -axis: (a) Dispersed barrier hardening model according to Eq. (61); (b) BKS model according to Eq. (62); (c) FKH model according to Eq. (64). Identity is indicated by the dashed line with slope = 1.

The error bars of the model data shown on the x -axes are determined based on the uncertainties of the cluster parameters and Gaussian error propagation applied to Eqs. (61), (62) and (64). Statistical significance tests were formally applied to the estimated coefficients of correlation regardless of the limitations imposed by the model simplifications and the data sets. It turns out that each of the correlations shown in Fig. 35 is statistically significant at the 0.05 level of significance (null hypothesis $\rho = 0$). The differences of the coefficients of correlation, R^2 , for each pair of models are statistically insignificant at the 0.05 level (null hypothesis $\rho_1 = \rho_2$). The latter means that we cannot favor any one of the models over any other on the basis of a higher coefficient of correlation. However, it is reasonable to suggest the application of the DB hardening model for the following reasons:

- The pre-factor α fitted in Fig. 35a is in good agreement with reported values of the obstacle strength for both low- and high-Cu RPV steels [13].

- The pre-factor fitted in Fig. 35b is meaningless in the framework of the BKS model. Meaning that it should be equal to 1 as the obstacle strength is already included in the second square-bracket term of Eq. (62).
- The pre-factor fitted in Fig. 35c is significantly different from the factor 1/8 predicted by the original FKH model, Eq. (64).
- The DB hardening model is also favored because of its simplicity and high coefficient of correlation (not to be confused with the statement of its absolute validity or the invalidity of other models).

CONCLUSION: Flux effects on neutron-irradiated high- and low-Cu RPV steels have been investigated by means of SANS and hardening measurements. A significant effect on the mean cluster radii was revealed, i.e. higher fluxes generally lead to smaller clusters. The effects on the number density and volume fraction of clusters are less pronounced but still present. Peculiarly, at first glance the changes found on the nanostructural level do not seem to reflect in systematic changes of the mechanical properties.

Two models of cluster evolution were introduced and compared with the cluster properties acquired from SANS. The model comparison indicated that the irradiation-induced clusters evolve according to deterministic growth in combination with radiation-enhanced diffusion.

In addition, four dedicated hardening models were tested against experimental hardening data. One of the hardening models, namely Russel-Brown, can be excluded, because it would give rise to a measurable trend of the hardness change as a function of flux, which was not observed.

The remaining three hardening models, DB, BKS and FKH, fit statistically equally well to the mechanical property changes. However, as the DB hardening model is the most simple physically based model, which can adequately predict the hardening increase from the cluster properties of all materials as a whole, it is suggested for application for the present purpose. The flat profile of hardening changes predicted by the DB model in the present flux range (Fig. 34) in conjunction with the uncertainties (Fig. 35) agrees well with the finding of a non-visible flux effect on the mechanical properties. A possible approach to resolve flux effects on hardening is based on an extension of the covered flux range by at least an order of magnitude.

5.2 LATE-BLOOMING EFFECT

5.2.1 Overview

The SANS results presented in Section 4.2 show that the volume fraction of the RH-irradiated low-Cu steels JPB and JPC exhibits an unexpected change of slope (CoS). Indeed, the slope of the cluster volume fraction increases with increasing fluence, whereas a smooth, power-law-like evolution with an exponent less or equal 1 is usually observed. Similarly, a CoS was found for the yield-stress and hardness increase.

It cannot be decided, due to the small number of accessible levels of neutron fluence, to which extent the observed CoS reflects a gradual or abrupt change. The emphasis is placed on a pronounced increase of slope here. The SANS and hardness results show that this effect is most pronounced for material JPC-RH. This particular material/irradiation condition is therefore selected for additional APT measurements. The following findings are obtained by means of APT:

- The volume fraction of the clusters exhibits a fluence dependence strikingly similar to the volume fraction derived from the SANS results.
- The element analysis of the clusters shows an enrichment of Mn, Ni and Si and partly with Cu. Mo also plays a role in some clusters.
- The participation of Cu is underpinned by its high enrichment factors (see Table 8). The enrichment is particularly high for the medium fluence condition and decreases significantly from medium to high fluence.

It remains to be discussed what kind of effects, whether caused by experimental limitations or by distinct cluster-formation mechanisms, can lead to the CoS observed for the present low-Cu materials. Several scenarios are to be outlined below, which potentially explain the observed CoS in the evolution of clusters and mechanical properties. This is followed by an evaluation of the scenarios based on the present experimental findings and recent literature.

- (i) **MATERIAL HETEROGENEITY:** Macroscopic heterogeneity of the solute-element distribution, e.g. locally Cu-enriched and Cu-depleted zones, lead to significant fluctuations in irradiation susceptibility [9]. If a high-fluence sample is coincidentally taken from a region of higher irradiation susceptibility and a low-fluence sample from a region of lower irradiation susceptibility, then the results obtained for these two samples may fake an apparent CoS.
- (ii) **HOMOGENEOUS NUCLEATION:** Odette predicted [7, 17] by means of Monte Carlo calculations the delayed homogeneous nucleation of Mn, Ni and Si to stable phases. The simulations were based purely on thermodynamic parameterizations, and no direct interaction between irradiation-induced point defects (PD) was included. In this framework [7, 17], the PD excess solely leads to

an enhancement [11] of solute migration. Only after an incubation period, the solute migration gives rise to a rapid formation of thermodynamically stable phases in miscibility gaps in the phase diagram [117] and, therefore, causing a CoS in the cluster evolution.

- (iii) **LOWER DETECTION LIMIT:** A certain portion of the nanometer-sized clusters formed in RPV steels after irradiation might be smaller than the lower detection limit of the applied characterization technique. In a possible scenario depicted schematically in Fig. 36, the largest portion of the cluster population of the low-fluence condition is below the detection limit (approx. 0.5 to 0.6 nm for both SANS and APT). With increasing fluence new clusters are forming, and clusters already present eventually grow to sizes larger than the detection limit, leading to an apparent increase in the detected cluster-number density, as well as the volume fraction. Thus, according to this scenario, the CoS observed by means of SANS or APT does not reflect the actual cluster evolution, but rather arises solely from experimental limitations.

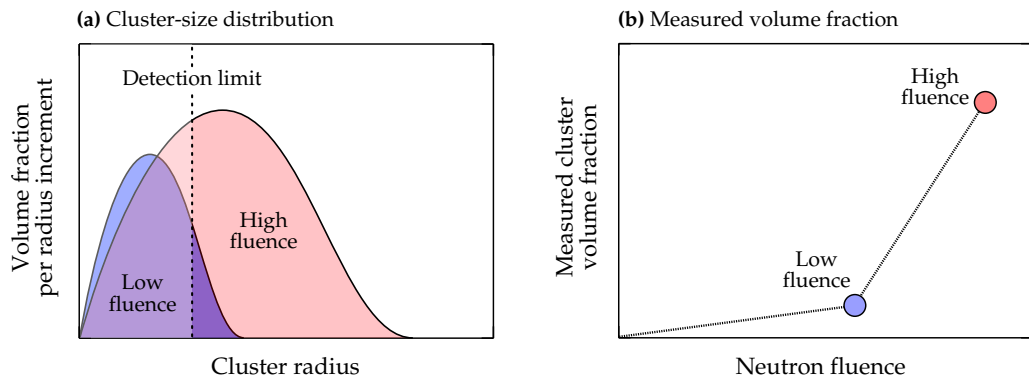


Figure 36: The effect of the lower detection limit on the measured volume fraction of two cluster populations from low and high fluence. At low fluences, large portions of clusters are below the detection limit and do not contribute to the measured volume fraction. The major portion of clusters from the high fluence are above the detection limit. This leads to an apparent increase of slope of the measured volume fraction as a function of neutron fluence.

- (iv) **HETEROGENEOUS NUCLEATION VIA COPPER-VAC MECHANISM:** Even though the materials investigated in the present context are low-Cu steels, Cu is still available in the bulk at concentrations higher than the solubility limit at typical operation temperatures [3, 4]. This Cu can diffuse via a Cu-vac mechanism and tends to contribute to the formation of Cu-vac clusters in an early stage [4, 118]. These Cu-vac clusters can then act as nuclei for the delayed formation of MNCs. A rationalization of the delay according to [119] is based on the insight that a minimum number of Cu atoms is needed before the attachment of Ni atoms becomes energetically favorable.
- (v) **HETEROGENEOUS NUCLEATION VIA MANGANESE-SIA MECHANISM:** The APT results show that Cu is not present in every cluster. Without the presence

of Cu, it is necessary that a different kind of precursor is present for nucleation and cluster formation. Ngayam-Happy [19] introduced a formation mechanism based on the segregation of solute elements to irradiation-induced SIA clusters. In the context of the APT results given in Section 3.2.2, the presence of such a mechanism is plausible.

Material heterogeneities in RPV steels (scenario i) is an issue most prominent in welding seams [120]. Strong temperature gradients and a high impurity-intake during the joining process can lead to an uneven distribution of solute elements in the material matrix. However, this is not an issue with the present materials JPB and JPC. Both materials are pure base metals, which were manufactured under laboratory conditions, and the local variation of the chemical composition is low (see Table 1 and 7). Moreover, the CoS for these materials has been confirmed by four independent methods over a range of different sample sets. It is, therefore, unlikely that random fluctuations in chemical composition and irradiation susceptibility lead to such kind of systematic trend.

The topic of irradiation-enhanced homogeneous nucleation in low-Cu steels (scenario ii) is still a matter of debate. In recent MC simulations [21], it is argued that the miscibility gap of phases formed via homogeneous nucleation is too small to account for the concentration of clusters experimentally observed. Furthermore, there are several experimental findings that highlight the predominant role of Mn during early cluster formation [51, 121–123]. This cannot be rationalized on the basis of a solely thermodynamically driven [20] process. Rather, it is implied that a purely irradiation-enhanced process, i.e. homogeneous nucleation, is neither found [4], nor necessary [21] for the formation of clusters in low-Cu RPV steels. The present findings from APT, i.e. the high scatter of the MnNiSi cluster composition shown in Fig. 30, support this conclusion since no distinct phases are identified. Therefore, homogeneous nucleation is not considered here any further.

The lower detection limits (scenario iii) can rationalize the observed CoS for the RH irradiation under certain conditions, as schematically illustrated in Fig. 36. However, this scenario is in conflict with the SANS results of the high-flux BR2 irradiations, which exhibit no CoS. Indeed, the investigations on flux effects, Section 4.1, indicate that higher fluxes lead to smaller, yet more clusters at the same level of fluence. If the lower detection limit is considered to be the origin of the observed CoS for the RH irradiation, the CoS would be even more pronounced for the BR2 irradiations. However, this was not observed for BR2 samples, see Fig. 23b. It is, therefore, concluded that the lower detection limit cannot be the origin for the CoS.

So far, we excluded scenarios (i) to (iii). The two remaining scenarios (iv) and (v), both involving heterogeneous nucleation, are not in conflict with the present experimental findings and are also consistent with the recent literature. It is reasonable to assume that both mechanisms operate in parallel since the APT results show Cu in some, but not all clusters. In the following two sections both scenarios (iv) and (v) are considered in more detail with regard to a dual-path cluster formation mechanism, depicted schematically in Fig. 37. We will then come back to the issue of the

CoS and decide on the basis of a sub-selection of clusters measured with APT which of the presented mechanisms are responsible for the observed CoS.

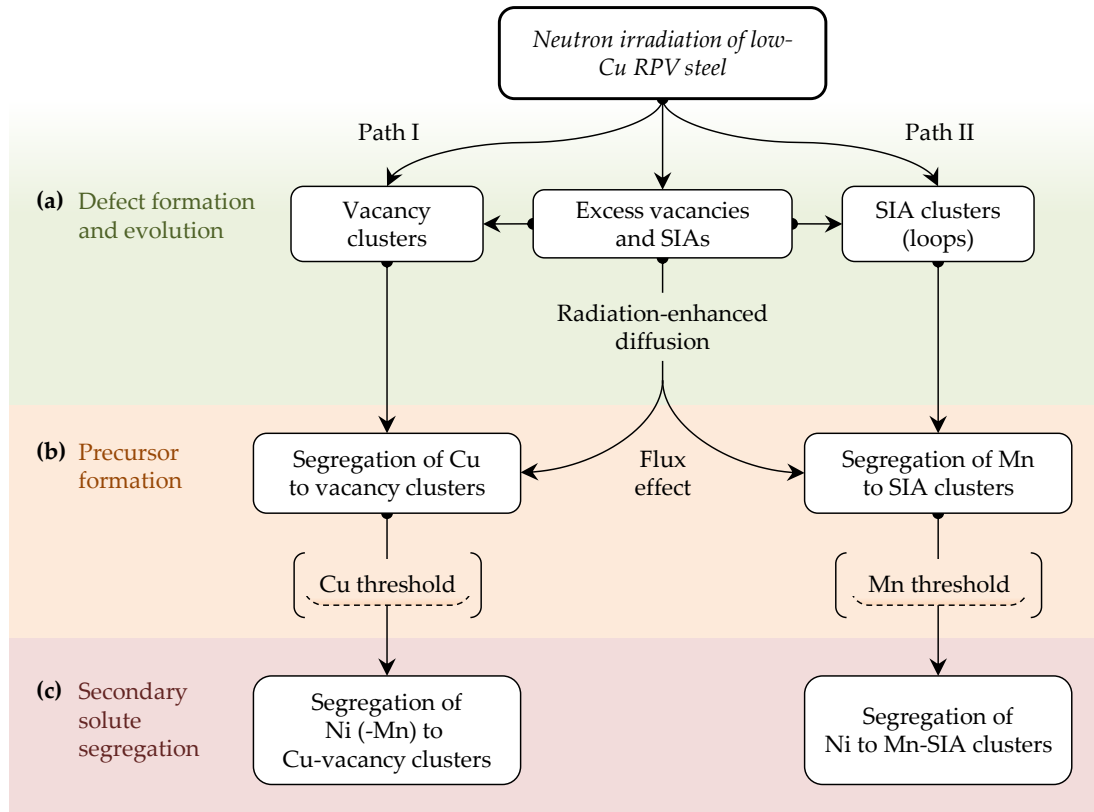


Figure 37: Schematic overview of irradiation-induced cluster evolution in low-Cu RPV steel in three stages (a-c). Two paths of cluster formation and evolution occur in parallel: Path I, based on Cu-vac precursors and Path II, based on Mn-SIA precursors.

According to the top of Fig. 37, neutron irradiation of low-Cu RPV steel leads to an excess of free vacancies and self-interstitial atoms (SIA) in the material matrix. Spherical vacancy clusters and planar self-interstitial atom clusters (SIACs) are forming either instantly at the cascade stage or evolve over a time span via point-defect migration [124, 125]. The available excess of vacancies and interstitials in the Fe matrix leads to an enhancement of diffusion of the solute elements. Here, the paths split according to the type of point defect considered. The left side of the scheme, Path I, heterogeneous nucleation via Cu-vacancy mechanism, is to be introduced in more detail in the section below. This is followed by a section on Path II, related to the corresponding self-interstitial based formation mechanism in conjunction with Mn.

5.2.2 Heterogeneous nucleation via Cu-vac mechanism

THE ROLE OF COPPER AND VACANCIES: The finding of high Cu-enrichment factors motivates a more elaborate discussion of the role of Cu during the cluster formation in low-Cu steels. It is generally accepted that in high-Cu (> 0.1 wt.%) steels the

formation of Cu-rich clusters is mainly thermodynamically driven via the supersaturation of Cu in the bulk [17, 41]. The excess of vacancies in the material introduced in the cascade stage gives rise to an enhancement of the otherwise slowly advancing, thermodynamically driven formation of Cu-rich clusters. The present materials JPB and JPC, however, bear one of the lowest Cu-level attainable in steels, of about 0.01 wt.%. Although a Cu level this low is still above the solubility limit given with about < 0.005 wt.% [3, 4], a pure thermodynamically driving force is not strong enough to explain Cu-clustering in low-Cu steels.

It is well established that Cu and vacancies form stable complexes. However, it is still a matter of debate whether these complexes form via the attachment of solute-Cu to already available vacancy clusters [4] (from PKA stage), or if Cu is dragged by migration of single vacancies [19, 126], or a combination thereof. Although Cu is not a major constituent of the clusters (Table 7), it has still a triggering or catalytic role for the clustering of other solutes, such as Ni.

NUCLEI FORMATION: The binding energies and structure of Cu-vacancy complexes and solute Ni in Fe were studied [127, 128] with a combined Monte-Carlo and molecular-dynamic (MC-MD) approach by Al-Motasem. The analysis of the simulated clusters revealed that clusters in a pure FeCu system [127] form a core-shell structure, comprising a vacancy-core, covered with a shell of Cu atoms. This is in agreement with the Cu-vacancy arrangement identified [129] by means of Doppler-broadening PAS in RPV steels, which contained a similarly low amount of Cu as the materials in the present investigation. Further calculations on a ternary FeCuNi system [128] indicate that Ni tends to co-segregate to spherical Cu-vacancy complexes, from now on referred to as Cu-vac nucleus. It was found that, according to the binding energies, Ni atoms never directly attach to the vacancy interface of the Cu-vacancy nucleus, but only to the outside layer of Cu atoms.

An inner-Cu and outer-Ni shell have not been distinctly identified by means of APT. This is largely expected due to strong trajectory overlaps [130] during Cu evaporation in the Fe matrix [131], which is even amplified due to the non-zero vacancy fractions [129] in Cu-containing clusters. Although indications for an inner-Cu and outer-Ni arrangement in clusters have been published [132, 133], these were mainly based on differences in the center of mass of Cu and Mn/Ni atoms in clusters. Also in the present APT data no distinct inner-Cu and outer-Ni structure was observed. However, this is expected due to the very low amount of Cu found in the clusters, containing less than 7 Cu atoms per cluster after APT detector-efficiency correction.

INCUBATION MECHANISM: In a subsequent rate theory (RT) study, the results of the MC-MD calculations [127, 128] were utilized to introduce a model of the Ni uptake in Cu-bearing steels [119]. To this end, the authors evaluated the binding energies between Ni-Ni and Ni-Cu as a function of the size of the nucleus. The two functions from the analytical fits to the MC-MD data points (Ni-Ni and Ni-Cu) intersect at a particular nucleus size. According to these calculations, the Ni

uptake is not triggered until the nucleus size is larger than the size indicated by the intersection point, which may be the origin of the CoS.

5.2.3 Heterogeneous nucleation via Mn-SIA mechanism

LOOP FORMATION: Cu-free MNCs constitute the largest portion of the cluster population observed via APT in the material JPC-RH, see Table 10. The formation scheme of Cu-free clusters, Path II, is depicted on the right side of Fig. 37. In step (a) of Path II, loops form in the Fe matrix upon neutron irradiation during the cascade phase and via self-interstitial migration and agglomeration. For pure α -Fe, it was shown [125] by means of cluster dynamics simulations that the loop number density quickly increases with fluence and reaches a saturation-like behavior already at low fluences of about $1 \cdot 10^{19} \text{ n cm}^{-2}$. A similar fluence dependence of the loop-number density has been found experimentally in pure α -Fe by means of TEM measurements [124, 134]. These findings indicate that no incubation period for loop formation is present, at least in the fluence range of interest. Therefore, it is reasonable to assume that loops themselves cannot be the origin of the observed CoS.

SOLUTE SEGREGATION: According to Path II, step (b), loops act as nucleation sites for solute segregation. Indeed, the half-torus shape of certain clusters in Figs. 25c and 26c indicate that the clusters originate from loops. A toroidal cluster and the suspected corresponding dislocation loop with a diameter of about 3.5 nm is shown in Fig. 38 from two different viewing angles.

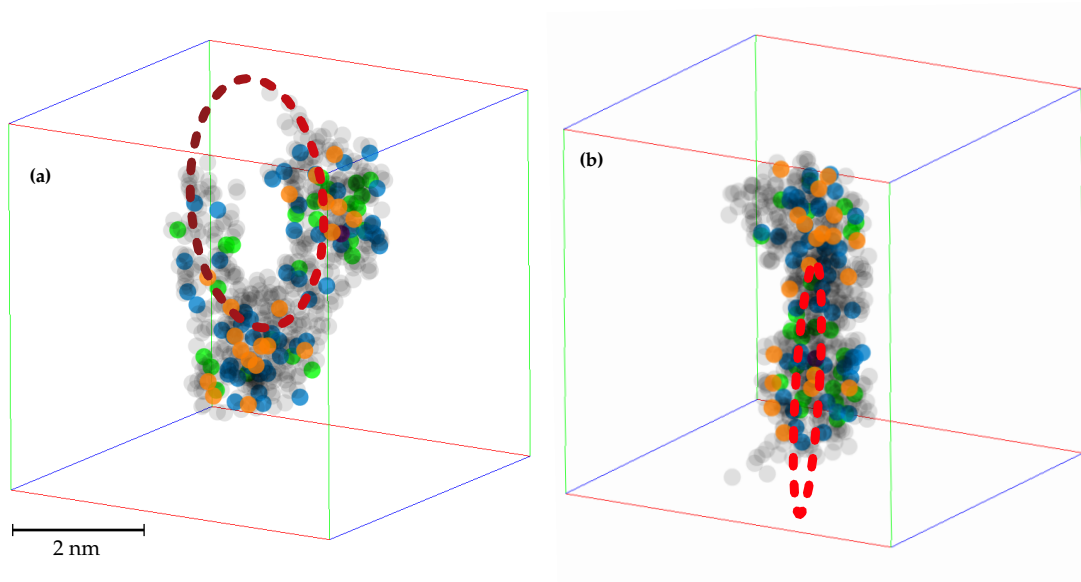


Figure 38: APT element distribution of a Cu-free MNCs from JPC-RH at high neutron fluence, from Fig. 26c. (a), front view of the cluster and (b), rotated view of the same cluster. The half-torus shape indicates that the cluster formed via segregation of solute elements to a loop, approximately 3.5 nm in diameter. The suspected loop is indicated by the red dotted line.

The interrelation of Mn and loops, which act as nucleation sites to the former, was shown in a combined APT/TEM study [23] of an ion-irradiated undersaturated FeMn alloy. In this study, heterogeneously distributed flat Mn clusters were found in the investigated volume. Supplementary results from TEM measurements and RT calculations lead the authors to the conclusion that loops are the most likely candidate for heterogeneous nucleation of solute Mn. A similar observation for an irradiated binary FeNi system has not been reported. In addition, first-principle simulations [135, 136] showed that Mn migrates via a self-interstitial mechanism in Fe. From this point of view, it is not surprising that Mn shows a high affinity to loops [19] and that the Mn migration is strongly enhanced by the irradiation-induced SIA flux in the matrix, dragging solute Mn atoms.

In the present work, there are indications that Mn indeed has a predominant role compared to other solute elements. This can be deduced from the APT results of the medium fluence condition. The cluster composition of these samples, renormalized such that $\text{Mn} + \text{Ni} + \text{Si} = 100\%$, see Fig. 30, shows that the number of clusters containing Mn, without containing Ni is more than four times higher than vice versa. This indicates the higher tendency of MNCs to form via a Mn-triggered formation mechanism. Similar observations on the early role of Mn during MNC formation have been reported for a FeMnNi model alloy:

- The early role of Mn during the formation of Cu-free clusters has been observed [51] by means of SANS measurements on a neutron-irradiated FeMnNi-model alloy. In this study, the predominant role of Mn during early cluster formation was derived from the A ratio of clusters at lower fluences. Vacancy clusters in Fe are characterized by an A ratio of 1.4. Elements with a positive value of scattering length raise the A ratio with respect to 1.4. Elements with a negative scattering length, such as Mn, lower the A ratio. The A ratio from clusters in the low-fluence condition was found [51] to be significantly lower than 1.4, indicating a dominant fraction of Mn atoms in the clusters.
- APT measurements [121] on the same model alloy confirmed the predominant role of Mn. While at the lowest fluence, clustering was identified only indirectly by means of statistical element correlations, the medium- and high-fluence condition comprised distinct clusters, composed of either Mn-Ni or Mn only. I.e. no pure Ni clusters were found.

INCUBATION MECHANISM: In the previous section, a possible explanation for an incubation period during heterogeneous nucleation via Cu-vacancies was given. No such explanation for the case of Cu-free MNCs, which addresses a delayed formation of clusters, seems to be available from the literature. However, it is reasonable to assume that a mechanism similar to the one predicted for Cu-vacancies may exist with respect to the Mn-SIA formation mechanism, namely that a minimum number of Mn atoms is necessary for the attachment of Ni atoms. Indeed, the observations of the present work support this idea.

5.2.4 Origin of the change of slope

On the basis of the two-path mechanism introduced above, it is helpful to use Cu as a criterion to subdivide the cluster population measured by means of APT in two fractions: (I), clusters that do contain Cu atoms and (II), clusters that are Cu free. According to this classification, the characteristics of clusters in JPC-RH determined by APT are listed in Table 10. The mean cluster radius and number density of Cu-containing and Cu-free clusters from Table 10 are plotted in Fig. 39 as a function of the neutron fluence.

Table 10: APT cluster characterization of JPC-RH. The total cluster populations are split into two parts: (I), Cu-containing clusters, and (II), Cu-free clusters. For the medium-fluence ($5.7 \cdot 10^{19} \text{ n cm}^{-2}$), the volume fractions and number density of clusters are similar between (I) and (II). At the high-fluence condition ($8.9 \cdot 10^{19} \text{ n cm}^{-2}$), the Cu-free clusters have 2 – 7 times higher concentration than the Cu-containing clusters.

ϕt (10^{19} n/cm^2)	(I) Cu-containing clusters			(II) Cu-free clusters		
	f_v (vol.%)	N (10^{16} cm^{-3})	\bar{R} (nm)	f_v (vol.%)	N (10^{16} cm^{-3})	\bar{R} (nm)
5.7	0.021 ± 0.008	4.6 ± 0.9	1.03 ± 0.08	0.026 ± 0.008	9.4 ± 1.2	0.88 ± 0.05
8.9	0.041 ± 0.012	6.7 ± 1.3	1.13 ± 0.08	0.183 ± 0.050	49.3 ± 3.4	0.96 ± 0.05

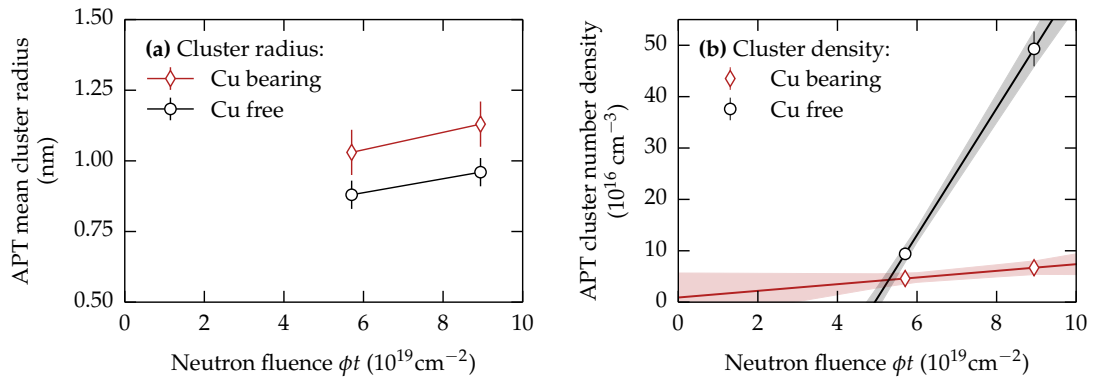


Figure 39: APT cluster-volume fraction of material JPC-RH categorized according to the Cu content: While Cu-containing MNCs show a linear-like volume increase with the fluence, the Cu-free fraction undergoes a steep increase between the medium- and high-fluence condition. According to this classification, the observed change of slope in the total cluster fraction originates for the most part from Cu-free clusters.

We can see in Fig. 39a that the mean radii of Cu-containing clusters are about 10 % larger than the radii of Cu-free clusters. The size difference between Cu-free and Cu-containing clusters is similar for both fluence levels. It is important to note that the size difference cannot arise from the additional Cu atoms in the clusters. Only 1 to 4 atoms of Cu are detected in the Cu-containing clusters. This amounts to a maximum of 7 Cu atoms after efficiency correction. In fact, about 96 additional solute atoms are required to attain a growth from 0.9 to 1.0 nm in radius. The significant difference in

size between the two cluster populations indicates the presence of at least two cluster-formation mechanisms, operating at different rates and/or with different incubation times, which is in agreement with the proposed model (Fig. 37).

The evolution of the number density with fluence of both cluster populations is presented in Fig. 39b. The Cu-containing clusters exhibit a slowly increasing or, within uncertainties, saturation-like behavior. Only few or no new Cu-containing clusters are formed at the investigated fluences. Due to the flat profile, the existence of a threshold fluence predicted (see Section 5.2.2, last paragraph) for Cu containing clusters can therefore not be confirmed for the present case. A threshold might either be nonexistent or simply not visible due to the lack of data at the lowest fluences.

In contrast, the number density of Cu-free clusters exhibits a strong increase from medium to high fluence and, according to this classification, Cu-free clusters are the origin of the CoS observed by means of SANS, APT and mechanical property measurements. Since Cu-free clusters are smaller than Cu-containing clusters for both fluences, it is reasonable to assume that they have formed after crossing a certain threshold fluence at which the segregation of Ni is triggered. This threshold can be estimated under the assumption of a linearly increasing [137] number density with fluence. For the present material and irradiation condition, this threshold is about $4.9 \cdot 10^{19} \text{ n cm}^{-2}$ for the Cu-free clusters, as shown in Fig. 39b. This is in agreement with a different study [13], in which a threshold fluence of about $3.5 \cdot 10^{19} \text{ n cm}^{-2}$ has been estimated from SANS measurements of several low-Cu steels. However, no distinction between Cu-free and Cu-containing clusters is possible on the basis of SANS data.

The experimental findings and literature review on Cu-containing clusters lead to the following conclusions:

- The observation of Cu-Ni-enriched clusters shows that heterogeneous nucleation via Path I is operative in the present case. It amounts to 1/2 and 1/8 of the total cluster-number density for the medium and high fluence, respectively. The number density as a function of fluence is consistent with a linear dependence.
- The larger size of the Cu-containing clusters as compared to the Cu-free clusters indicates that Cu-containing clusters tend to form earlier.
- There is a potential explanation for a threshold for the onset of Ni segregation, which is based on the minimum number of Cu atoms needed to trigger Ni attachment to Cu-vacancy clusters. This kind of threshold is not observed in the present case.
- The absence of a visible threshold is attributed to the weakness of the effect in combination with experimental limitations (fluence range, measuring accuracy).

The findings on Cu-free clusters forming via heterogeneous nucleation to Mn-SIAs are summarized as follows:

- Cu-free Mn-Ni-containing clusters account for the greatest fraction observed for both medium and high fluence. The predominance of Cu-free clusters is particularly pronounced in the high fluence condition. The CoS originates mainly from Cu-free clusters, as seen in Fig. 39b.
- The appearance of half-torus shaped Cu-free clusters indicates an interrelation between dislocation loops and solute atoms, i.e. solute segregation.
- The finding of a significant amount of Ni-free Mn-containing clusters indicates a predominant role of Mn during the cluster formation. This is in agreement with recent findings from the literature.
- A threshold-like mechanism is assumed to operate: The Mn-SIA nuclei have to exceed a certain size to make the uptake of Ni energetically favorable.

5.2.5 RH irradiation versus BR2 irradiation

As opposed to the findings for the RH irradiated materials, the BR2 irradiations of the same steels exhibit no CoS in neither cluster-volume fraction observed by SANS, nor in the mechanical properties, measured by yield stress and hardness increase. This remains to be examined. The two most significant differences between the RH and the BR2 irradiation campaign are the neutron flux and irradiation temperature, both being higher for the BR2 irradiation (see Table 2 on irradiation conditions).

DIFFERENCE IN NEUTRON FLUX: On the basis of the findings on flux effects it will be examined if and how the flux differences might be responsible for a different irradiation response (CoS vs. continuous evolution) between both irradiation campaigns. According to heterogeneous nucleation, via Mn-SIA nuclei, Ni atoms only segregate to a Mn nucleus if the latter exceeds a size threshold. Within the framework established in Section 5.1, it is possible to estimate the relative size difference of the Mn-SIA nuclei from the RH and the BR2 irradiations:

The average neutron fluxes of the BR2 and RH irradiation are 1.9 and $41.7 \cdot 10^{12} \text{ n cm}^{-2} \text{ s}^{-1}$, respectively. Due to flux effects discussed in Section 5.1, the clusters from the BR2 irradiation are expected to be smaller at equal levels of fluences. This effect can be estimated by applying Eq. (55) and the transition flux of $\phi_t = (1.30 \pm 0.20) \cdot 10^{12} \text{ n cm}^{-2} \text{ s}^{-1}$ (both taken from Section 5.1.3.1 on deterministic growth). Under the assumption that Mn nuclei evolve similarly to whole clusters, it is estimated that Mn nuclei from the BR2 irradiation are about 40% smaller at the same neutron fluence than the ones from the RH irradiation. This would shift the CoS to occur at higher values of neutron fluence.

We already assumed that the Mn-nuclei evolve via a deterministic growth process. This means that its radii evolve according to Eq. (50), which can be written as a fluence-dependent growth $\bar{R} \propto (\phi t)^{1/2}$. The CoS for the RH-irradiated materials was observed between a fluence range of 5.7 and $8.9 \cdot 10^{19} \text{ n cm}^{-2}$. To outweigh the smaller Mn-nuclei of the BR2 irradiation and to observe a CoS, the material needs

to be irradiated to fluence levels about 2.6 times higher than the investigated fluence range. This means that a CoS for the high-flux BR2 irradiation is potentially present in a fluence range between 14.9 and $23.3 \cdot 10^{19} \text{ n cm}^{-2}$. For material JPB-BR2, this is just in the vicinity of the highest fluence level available, $15.0 \cdot 10^{19} \text{ n cm}^{-2}$. For material JPC-BR2, the maximum fluence available, $11.7 \cdot 10^{19} \text{ n cm}^{-2}$, is well below the level where the CoS might occur.

Based on the considerations on flux effects and the possible existence of a Mn-nuclei-size threshold for Ni segregation, the CoS cannot be observed for the available fluence ranges of the BR2 irradiations. Further irradiations at the BR2 facility of materials JPB and JPC to fluences $> 15 \cdot 10^{19} \text{ n cm}^{-2}$ would be necessary to test the estimations given in the paragraph above.

IRRADIATION TEMPERATURE: The influence of the irradiation temperature on the nanostructure has been investigated by rate theory simulations for pure Fe [138], ferritic-martensitic alloys [139] and a combined TEM/PAS study on RPV steels [140]. In addition, it is known that the effects of irradiation temperature and neutron flux are coupled [141]. However, a mechanistic understanding of the influence of the irradiation temperature on the parameters of the cluster population has not been established for neutron irradiated RPV steels. A detailed study on the effects of irradiation temperature and its interrelation with flux effects must be beyond the scope of this work since only two irradiation temperatures were available.

Intuitively it is clear that the irradiation temperature influences the evolution of the mechanical properties and the nanostructure with fluence. Indeed, a lower irradiation temperature T_{irr} leads to a higher irradiation damage [142] at equal neutron fluences. An empirical approach commonly used to describe the influence on the yield-stress increase, $\Delta\sigma_y$, is given by Jones [143]. He introduced a correction factor F_T , which compensates for different irradiation temperatures T_{irr} . The correction is described by a linear dependency

$$\Delta\sigma_y \propto F_T \cdot \sqrt{\phi t}, \quad \text{where} \quad F_T = A - B \cdot T_{\text{irr}} \quad (65)$$

where the parameters A and B are given [143, 144] with 1.85 ± 0.30 and 4.59 ± 0.07 , respectively, depending on the type of material and database selected for parameter fitting. It is interesting to note that material JPC was one of the materials included in the set of materials used for fitting [144]. The fluence dependency of $\Delta\sigma_y$ is incorporated by a simple square-root law. According to Eq. (65), the 255 °C irradiation at RH leads to a yield-stress increase about 30 % higher than the 290 °C BR2 irradiation. This is in reasonable agreement with the results measured for both irradiation campaigns.

However, for the present materials the irradiation temperature was kept constant within one campaign, in both the BR2 and the RH irradiation. Assuming that there is no change in irradiation temperature from one fluence level to another, and given that the linear correlation from Eq. (65) is applicable to the present materials, the irradiation temperature cannot be the cause underlying the appearance /

non-appearance of a CoS. The application of Eq. (65) to the present data would in fact only shift the yield-stress increase by an equal amount for one material and irradiation campaign. A CoS cannot be introduced or compensated.

Potential reasons for the occurrence or non-occurrence of a CoS of the irradiation response have been discussed on the basis of the differences between the BR2 and the RH irradiation. The main points are summarized as follows:

- The high-flux irradiation of BR2 leads to smaller Mn-SIA nuclei than for the RH irradiation at equal levels of fluence. Under the assumption that the Mn-SIA nuclei evolve with fluence according to deterministic growth, it is estimated that the fluences for the BR2 irradiations are not sufficient for the triggering of an accelerated Ni uptake. For this to occur, fluence levels of $> 15 \cdot 10^{19} \text{ n cm}^{-2}$ are necessary.
- The irradiation temperature T_{irr} does affect the irradiation response of the material. Lower T_{irr} yields a higher irradiation sensitivity of the material, i.e. higher hardening and cluster volume fraction. The empirical correlation, Eq. (65), is applicable to the present cases. Within this simple correlation, the irradiation temperature cannot be the origin of the observed / not observed CoS for the RH and BR2 irradiation, respectively.
- It is likely that both, temperature and flux, have an impact on the irradiation-induced nanostructure and that these effects are coupled. However, this issue is beyond the scope of the present work and cannot be fully resolved due to the lack of samples with systematically varied irradiation temperatures.

CONCLUSIONS

Neutron irradiation of reactor-pressure vessel steel leads to the formation of nanometer-sized defect-solute clusters, which impede the free dislocation movement in the lattice and ultimately lead to an increase of hardening and embrittlement of the material.

This thesis has dealt with the characterization of nanoscale defect-solute clusters formed upon neutron irradiation in reactor-pressure vessel steels. Special focus has been placed on the implications of long-term irradiation and on how the nanostructure evolution differs from the one occurring under accelerated conditions. Two major topics were considered in this context:

- (i) **FLUX EFFECTS:** The neutron flux under which the samples are irradiated influences the characteristics of the cluster population. The differences in the irradiation response of the steel between high- and low-flux irradiations are summarized under the term *flux effects*. The key questions raised in this regard are:
 - a) What are the main effects of flux on the characteristics of the clusters formed upon neutron irradiation?
 - b) Which are the mechanisms of cluster formation?
 - c) How do the observed differences in cluster characteristics reflect themselves in the mechanical properties of the materials?
- (ii) **LATE-BLOOMING EFFECT:** A special irradiation effect as a function of neutron fluence was reported [15] based on thermodynamical simulations: Under certain long-term irradiation conditions a delayed formation of solute clusters was anticipated for low-Cu materials. The delay manifests itself in a change of slope (CoS) of cluster-volume fraction and cluster-number density as a function of fluence. This effect, also called *late-blooming effect*, causes particular safety concerns, since it might not be observable under accelerated irradiation conditions. This prompts the following questions:
 - a) What is the origin of the CoS in the irradiation response?
 - b) Does the CoS in volume fraction of the irradiation-induced clusters reflect itself in a CoS of the mechanical properties?

To address the issues of flux effects and late-blooming effect, a number of neutron-irradiated RPV steels of different composition were analyzed by means of SANS and hardness testing. In addition, APT experiments were performed on one particular material, which showed the most pronounced CoS.

In order to resolve small but crucial differences in the size distribution of the irradiation-induced clusters by means of SANS, it was necessary to improve the data treatment. In this respect, the implemented Monte-Carlo fitting routine comprises the following specific features:

- a robust estimate of the size distribution without any prior assumption about the shape,
- per definition physically meaningful (positive) results,
- avoidance of any kind of subjectivity,
- derivation of a measure of statistical confidence.

Flux effects were studied on five RPV base and weld steels, comprising different levels of Cu. The sample sets were irradiated under high-flux and low-flux conditions up to the same level of fluence. This approach allows the dominating effect of fluence to be eliminated and the secondary irradiation effects of neutron flux on the characteristics of the cluster population to be revealed. Indeed, the SANS results showed that clusters formed under high-flux irradiation are significantly smaller and tend to be more numerous compared to the low-flux irradiation at the same fluence. The volume fraction of clusters is lower in the high-flux regime.

To interpret these trends, two cluster-evolution models, namely deterministic growth and coarsening were compared with the acquired SANS data. The cluster sizes and volume fractions as a function of flux indicated a flux-independent (sink-dominated) regime and a flux-dependent (recombination-dominated) regime. In the flux-dependent regime, the results are consistent with deterministic growth, while coarsening is ruled out. The transition flux between the sink-dominated and the recombination-dominated regimes was estimated to be $\phi_t = 1.3 \cdot 10^{12} \text{ n cm}^{-2} \text{ s}^{-1}$, which reasonably agrees with the value predicted on the basis of rate theory calculations.

The characterizations of the clusters by means of SANS were accompanied by hardness measurements of the same samples. Contrary to intuition, the hardness does not show a significant dependence on flux, even though the cluster-size distributions show a significant flux dependence.

This disparity was examined by coupling analytic expressions of deterministic growth with a number of hardening models and comparing the model-based predictions with the measured hardening data. It turned out that the RB-hardening model can be ruled out for the present data-set. The remaining three models, namely DB-, BKS- and FKH-hardening, predict no or a weak flux effect on hardening. Because the effect of size and number density partly cancel out one another, this is consistent with the absence of a significant experimental flux effect on hardening.

Both BKS- and FKH-hardening contain fixed expressions for the obstacle strength, which significantly differ from the experimental results. For DB-hardening, the obstacle strength is a free fit parameter. Even though no selection of one hardening

model over the other is possible on the basis of coefficients of correlation, it is advisable to treat the obstacle strength as a fitting parameter, as it is originally the case for DB-hardening model.

The second part of the thesis is focused on the investigation of the late-blooming effect observed in two low-Cu steels. The materials were irradiated at two different reactors to similar levels of fluences: Low-flux irradiations at 255 °C in one case (RH), and high-flux irradiations at 290 °C in the other case (BR2).

Both materials irradiated at the RH-reactor exhibit a change of slope (CoS), namely an increase, in the cluster-volume fraction determined by SANS. A similar effect was observed by means of hardness and tensile tests. Material JPC-RH showed the most pronounced change of slope and was thus inspected by means of APT to gather supplementary information about the nature of the clusters and the origin of the change of slope.

The cluster radii and volume fractions obtained by APT and SANS are similar. Moreover, the APT results show that the clusters in JPC-RH are mainly enriched with Mn, Ni and Si and that two classes of such MNCs can be distinguished: Cu-containing clusters and Cu-free clusters. On average, the Cu-containing MNCs are about 10 % larger than Cu-free MNCs and tend to be spherically shaped. In contrast, the Cu-free MNCs showed a ramified structure and, in several cases, a half-torus shape was observed. There are no indications of distinct equilibrium ternary Mn-Ni-Si phases.

These findings enabled the evaluation of several candidates of cluster-formation mechanisms, which were reported in recent literature to be the origin of the change of slope. In the present case, a two-path cluster-formation mechanism appears to be the most promising candidate to explain the appearance of the CoS and to be consistent with experimental observations. According to this scenario, the Cu-containing clusters form via a Cu-vacancy mechanism. A threshold fluence, which could explain the change of slope is not observed for the Cu-containing clusters. However, a threshold neutron fluence appears to be necessary to trigger the formation of Cu-free MNCs. The findings indicate, that irradiation-induced self-interstitial clusters are first enriched with Mn and that these Mn-enriched self-interstitial atom clusters act as nuclei for the formation of MNCs. Furthermore, a minimum nucleus size needs to be exceeded to trigger the uptake of Ni and other solutes and a change of slope in irradiation response becomes apparent.

The BR2 irradiations do not show a change of slope in irradiation response. The two-path cluster-formation mechanism in connection with the findings on flux effects rationalizes the different irradiation response between the RH- and the BR2-irradiation campaigns of materials JPB and JPC: At similar levels of neutron fluence, the high-flux irradiation of BR2, as an expression of flux effects, yields smaller Mn-SIA clusters than the RH irradiation. Therefore, the uptake of additional solute elements, such as Ni, is delayed to higher fluences, possibly not reached in the BR2 irradiations. Hence, the CoS is not observed for the BR2 irradiated materials.

It is the author's opinion that a more exhaustive understanding of flux effects and the late-blooming effect can only be achieved by means of multiscale modeling. Nevertheless, for the modeling approach to be truly observation fed, the availability of additional experimental data on the chemistry and nano-structure of the cluster population is essential in particular with regard to low-Cu RPV steels, which are neutron-irradiated under rarely available low-flux and high-fluence conditions. This can only be achieved within the collaboration of international institutions.

BIBLIOGRAPHY

- [1] IAEA. *Nuclear Power Reactors in the World - 2014 Edition*. Reference Data Series No. 2 IAEA-RDS-2/34. Vienna: International Atomic Energy Agency, 2014. ISBN: 978-92-0-104914-8.
- [2] B. L. Bramfitt and A. O. Benscoter. *Metallographer's Guide: Practices and Procedures for Irons and Steels*. Materials Park, OH: ASM International, 2001. 354 pp. ISBN: 978-0-87170-748-2.
- [3] F. Christien and A. Barbu. „Modelling of copper precipitation in iron during thermal aging and irradiation.“ *J. Nucl. Mater.* 324.2-3 (2004), pp. 90–96.
- [4] B. Radiguet, A. Barbu, and P. Pareige. „Understanding of copper precipitation under electron or ion irradiations in FeCu_{0.1} wt.% ferritic alloy by combination of experiments and modelling.“ *J. Nucl. Mater.* 360.2 (2007), pp. 104–117. DOI: 10.1016/j.jnucmat.2006.09.007.
- [5] P. G. Tipping. *Understanding and Mitigating Ageing in Nuclear Power Plants: Materials and Operational Aspects of Plant Life Management*. Woodhead Publishing, 2010. 944 pp. ISBN: 1-84569-511-9.
- [6] N. Soneda. *Irradiation Embrittlement of Reactor Pressure Vessels*. Waltham, MA: Woodhead Publishing, 2014. 409 pp. ISBN: 978-1-84569-967-3.
- [7] G. R. Odette and B. D. Wirth. „A computational microscopy study of nanostructural evolution in irradiated pressure vessel steels.“ *J. Nucl. Mater.* 251 (1997), pp. 157–171. DOI: 10.1016/S0022-3115(97)00267-5.
- [8] F. Bergner, A. Ulbricht, and H.-W. Viehrig. „Acceleration of irradiation hardening of low-copper reactor pressure vessel steel observed by means of SANS and tensile testing.“ *Phil. Mag. Let.* 89.12 (2009), pp. 795–805. DOI: 10.1080/09500830903304117.
- [9] E. Altstadt, E. Keim, H. Hein, M. Serrano, F. Bergner, H.-W. Viehrig, A. Ballesteros, R. Chaouadi, and K. Wilford. „FP7 Project LONGLIFE: Overview of results and implications.“ *Nuclear Engineering and Design* 278 (2014), pp. 753–757. DOI: 10.1016/j.nucengdes.2014.09.003.
- [10] R. Stoller. „1.11 - Primary Radiation Damage Formation.“ In: *Comprehensive Nuclear Materials*. Ed. by Rudy J.M. Konings. Oxford: Elsevier, 2012, pp. 293–332. ISBN: 978-0-08-056033-5.
- [11] G. R. Odette and G. E. Lucas. „Recent progress in understanding reactor pressure vessel steel embrittlement.“ *Radiat. Eff. Defect. S.* 144.1 (1998), pp. 189–231. DOI: 10.1080/10420159808229676.
- [12] IAEA Report. *Integrity of Reactor Pressure Vessels in Nuclear Power Plants: Assessment of Irradiation Embrittlement Effects in Reactor Pressure Vessel Steels*. NP-T-3.11. Vienna, 2009.

- [13] A. Wagner, A. Ulbricht, F. Bergner, and E. Altstadt. „Influence of the copper impurity level on the irradiation response of reactor pressure vessel steels investigated by SANS.“ *Nucl. Instrum. Meth. B* 280 (2012), pp. 98–102. DOI: 10.1016/j.nimb.2012.03.008.
- [14] G. R. Odette. „On the dominant mechanism of irradiation embrittlement of reactor pressure vessel steels.“ *Scripta Metallurgica* 17.10 (1983), pp. 1183–1188. DOI: 10.1016/0036-9748(83)90280-6.
- [15] G. R. Odette. „Radiation induced microstructural evolution in reactor pressure vessel steels.“ *Mater. Res. Soc. Symp. Proc.* 373 (1995), pp. 137–148.
- [16] P. A. Beaven, F. Frisius, R. Kampmann, and R. Wagner. „Analysis of defect microstructures in irradiated ferritic alloys.“ *At. Transp. Defects Met. Neutron Scatt. C Janot W Petry Richter T Springer Eds Springer Proc. Phys. Vol 10 Springer Berl.* (1985), pp. 228–234.
- [17] C. L. Liu, G. R. Odette, B. D. Wirth, and G. E. Lucas. „A lattice Monte Carlo simulation of nanophase compositions and structures in irradiated pressure vessel Fe-Cu-Ni-Mn-Si steels.“ *Materials Science and Engineering: A. Microstructure Evolution in Bulk Phases F* 238.1 (1997), pp. 202–209. DOI: 10.1016/S0921-5093(97)00450-4.
- [18] H. Lukas, S. G. Fries, and B. Sundman. *Computational Thermodynamics: The Calphad Method*. Cambridge, New York: Cambridge University Press, 2007. 324 pp. ISBN: 978-0-521-86811-2.
- [19] R. Ngayam-Happy, C. Becquart, C. Domain, and L. Malerba. „Formation and evolution of MnNi clusters in neutron irradiated dilute Fe alloys modelled by a first principle-based AKMC method.“ *J. Nucl. Mater.* 426.1–3 (2012), pp. 198–207. DOI: 10.1016/j.jnucmat.2012.03.033.
- [20] P. B. Wells, T. Yamamoto, B. Miller, T. Milot, J. Cole, Y. Wu, and G. R. Odette. „Evolution of manganese–nickel–silicon-dominated phases in highly irradiated reactor pressure vessel steels.“ *Acta Materialia* 80 (2014), pp. 205–219. DOI: 10.1016/j.actamat.2014.07.040.
- [21] G. Bonny, D. Terentyev, A. Bakaev, E. E. Zhurkin, M. Hou, D. Van Neck, and L. Malerba. „On the thermal stability of late blooming phases in reactor pressure vessel steels: An atomistic study.“ *J. Nucl. Mater.* 442.1–3 (2013), pp. 282–291. DOI: 10.1016/j.jnucmat.2013.08.018.
- [22] G. Bonny, D. Terentyev, E. E. Zhurkin, and L. Malerba. „Monte Carlo study of decorated dislocation loops in FeNiMnCu model alloys.“ *J. Nucl. Mater.* 452.1–3 (2014), pp. 486–492. DOI: 10.1016/j.jnucmat.2014.05.051.
- [23] E. Meslin, B. Radiguet, and M. Loyer-Prost. „Radiation-induced precipitation in a ferritic model alloy: An experimental and theoretical study.“ *Acta Mater.* 61.16 (2013), pp. 6246–6254. DOI: 10.1016/j.actamat.2013.07.008.
- [24] A. Ballesteros and E. Altstadt. „RPV Long Term Operation: Open Issues.“ *Strength Mater.* 45.4 (2013), pp. 392–396. DOI: 10.1007/s11223-013-9471-0.

- [25] P. Lindner, F. Leclercq, and P. Damay. „Analysis of water scattering used for calibration of small-angle neutron scattering (SANS) measurements.“ *Physica B* 291.1-2 (2000), pp. 152–158. DOI: 10.1016/S0921-4526(99)01397-6.
- [26] D. S. Sivia. *Elementary Scattering Theory: For X-ray and Neutron Users*. 1 ed. Oxford; New York: Oxford University Press, 2011. 216 pp. ISBN: 978-0-19-922868-3.
- [27] M. K. Miller. *Atom Probe Tomography: Analysis at the Atomic Level*. 1st ed. Springer US, 2000. 250 pp. ISBN: 0-306-46415-2.
- [28] B. Gault, M. P. Moody, and J. M. Cairney. *Atom Probe Microscopy: Atomic Resolution Microscopy and Microanalysis in Three Dimensions*. 1st ed. Springer, 2012. 396 pp. ISBN: 1-4614-3435-1.
- [29] R. Krause-Rehberg and H. Leipner. „Positron annihilation in semiconductors: defect studies.“ In: *Encyclopaedia of Physics*. Vol. 127. Springer Verlag, 1999.
- [30] G. Brauer and K. Popp. „Neutron Embrittlement of Reactor Pressure Vessel Steels: A Challenge to Positron Annihilation and Other Methods.“ *phys. stat. sol. (a)* 102.1 (1987), pp. 79–90. DOI: 10.1002/pssa.2211020106.
- [31] C. L. Gil, A. P. De Lima, N. A. De Campos, J. V. Fernandes, G. Kögel, P. Sperr, W. Triftshäuser, and D. Pachur. „Neutron-irradiated reactor pressure vessel steels investigated by positron annihilation.“ *J. Nucl. Mater.* 161.1 (1989), pp. 1–12. DOI: 10.1016/0022-3115(89)90456-X.
- [32] G. Brauer, L. Liskay, B. Molnar, and R. Krause. „Microstructural aspects of neutron embrittlement of reactor pressure vessel steels - A view from positron annihilation spectroscopy.“ *Nuclear Engineering and Design* 127.1 (1991), pp. 47–68. DOI: 10.1016/0029-5493(91)90039-K.
- [33] R. Pareja, N. D. Diego, R. M. D. L. Cruz, and J. D. Río. „Postirradiation Recovery of a Reactor Pressure Vessel Steel Investigated by Positron Annihilation and Microhardness Measurements.“ *NT* 104.1 (1993), pp. 52–63.
- [34] R. Krause-Rehberg, W. Anwand, G. Brauer, M. Butterling, T. Cowan, A. Hartmann, M. Jungmann, A. Krille, R. Schwengner, and A. Wagner. „Progress of the EPOS project: Gamma-induced Positron Spectroscopy (GiPS).“ *Phys. Status Solidi C* 6.11 (2009), pp. 2451–2455. DOI: 10.1002/pssc.200982076.
- [35] M. Butterling, W. Anwand, T. Cowan, A. Hartmann, M. Jungmann, R. Krause-Rehberg, A. Krille, and A. Wagner. „Gamma-induced Positron Spectroscopy (GiPS) at a superconducting electron linear accelerator.“ *Nucl. Instrum. Methods Phys. Res. Sect. B Beam Interact. Mater. At.* 269.22 (2011), pp. 2623–2629.
- [36] J. W. Edington. *Practical electron microscopy in materials science*. Van Nostrand Reinhold Co., 1976. 364 pp. ISBN: 978-0-442-22230-7.
- [37] M. L. Jenkins and M. A. Kirk. *Characterisation of Radiation Damage by Transmission Electron Microscopy*. Taylor & Francis, 2000. 248 pp. ISBN: 978-0-7503-0748-2.

- [38] V. F. Sears. „Neutron scattering lengths and cross sections.“ *Neutron News* 3.3 (1992), pp. 26–37. DOI: 10.1080/10448639208218770.
- [39] A. Deschamps and F. De Geuser. „On the validity of simple precipitate size measurements by small-angle scattering in metallic systems.“ *J Appl Crystallogr* 44.2 (2011), pp. 1–10.
- [40] R. Cahn, K. Hono, and P. Haasen, eds. *Physical Metallurgy*. 4th. North Holland, 1996. ISBN: 0-444-89875-1.
- [41] M. Mathon, A. Barbu, F. Dunstetter, F. Maury, N. Lorenzelli, and C. de Novion. „Experimental study and modelling of copper precipitation under electron irradiation in dilute FeCu binary alloys.“ *J. Nucl. Mater.* 245.2–3 (1997), pp. 224–237. DOI: 10.1016/S0022-3115(97)00010-X.
- [42] J. A. Potton, G. J. Daniell, and B. D. Rainford. „A new method for the determination of particle size distributions from small-angle neutron scattering measurements.“ *J. Appl. Crystallogr.* 21.6 (1988), pp. 891–897. DOI: 10.1107/S0021889888004595.
- [43] J. A. Potton, G. J. Daniell, and B. D. Rainford. „Particle size distributions from SANS data using the maximum entropy method.“ *J. Appl. Crystallogr.* 21.6 (1988), pp. 663–668. DOI: 10.1107/S0021889888004819.
- [44] D. S. Sivia. „From dice to data analysis: Maximum entropy and Bayesian methods.“ *GNNW* 4.2 (1993), pp. 21–25. DOI: 10.1080/10448639308218940.
- [45] D. Tatchev and R. Kranold. „Maximum-entropy method as a routine tool for determination of particle size distributions by small-angle scattering.“ *J. Appl. Crystallogr.* 37.1 (2004), pp. 32–39. DOI: 10.1107/S0021889803023069.
- [46] O. Glatter. „A new method for the evaluation of small-angle scattering data.“ *J. Appl. Cryst.* 10.5 (1977), pp. 415–421.
- [47] O. Glatter. „Determination of particle-size distribution functions from small-angle scattering data by means of the indirect transformation method.“ *J. Appl. Crystallogr.* 13.1 (1980), pp. 7–11.
- [48] S. Hansen and J. S. Pedersen. „A comparison of three different methods for analysing small-angle scattering data.“ *J. Appl. Cryst.* 24.5 (1991), pp. 541–548.
- [49] D. I. Svergun. „Determination of the regularization parameter in indirect-transform methods using perceptual criteria.“ *J Appl Crystallogr* 25.4 (1992), pp. 495–503. DOI: 10.1107/S0021889892001663.
- [50] A. Ulbricht. „Untersuchungen an neutronenbestrahlten Reaktordruckbehälterstählen mit Neutronen-Kleinwinkelstreuung.“ Germany: Technischen Universität Bergakademie Freiberg, 2006.
- [51] F. Bergner, M. Lambrecht, A. Ulbricht, and A. Almazouzi. „Comparative small-angle neutron scattering study of neutron-irradiated Fe, Fe-based alloys and a pressure vessel steel.“ *J. Nucl. Mater.* 399.2-3 (2010), pp. 129–136.

- [52] H. Krauthäuser and G. Nimtz. „Real space distributions from SAS data using the novel structure interference method.“ *J. Mol. Struct.* 383.1–3 (1996), pp. 315–318. DOI: 10.1016/S0022-2860(96)09304-0.
- [53] S. Martelli and P. E. Di Nunzio. „Particle Size Distribution of Nanospheres by Monte Carlo Fitting of Small Angle X-Ray Scattering Curves.“ *Part. Part. Syst. Char.* 19.4 (2002), pp. 247–255. DOI: 10.1002/1521-4117(200208)19:4<247::AID-PPSC247>3.0.CO;2-8.
- [54] I. Hilger, F. Bergner, A. Ulbricht, A. Wagner, T. Weißgärber, B. Kieback, C. Heintze, and C. D. Dewhurst. „Investigation of Spark Plasma Sintered Oxide-Dispersion Strengthened Steels by Means of Small-Angle Neutron Scattering.“ *J. Alloys Compd.* 685 (2016), pp. 927–935. DOI: 10.1016/j.jallcom.2016.06.238.
- [55] A. Wagner, A. Ulbricht, and F. Bergner. „Robust Monte-Carlo fitting of small-angle neutron scattering curves for determining cluster-size distributions.“ *Schriften Forschungszentrums Jüil. 2012 Reihe Schlüsseltechnologien*. Proceedings of the 12th German Neutron Scattering Conference (2012), p. 146.
- [56] C. Sub-Committee. *Manufacturing History and Mechanical Properties of Japanese Materials Provided for the International Atomic Energy Agency*. IAEA Report. Japan, 1986.
- [57] E. Altstadt, F. Bergner, and H. Hein. „Irradiation Damage and Embrittlement in RPV Steels Under the Aspect of Long Term Operation: Overview of the FP7 Project LONGLIFE.“ In: *18th International Conference on Nuclear Engineering*. American Society of Mechanical Engineers, 2010, pp. 255–263.
- [58] A. Ballesteros, E. Altstadt, F. Gillemot, H. Hein, J. Wagemans, J. Rouden, J. Barthelmes, K. Wilford, M. Serrano, M. Brumovsky, R. Chaouadi, and S. Ortner. „Monitoring radiation embrittlement during life extension periods.“ *Nuclear Engineering and Design* 267 (2014), pp. 197–206. DOI: 10.1016/j.nucengdes.2013.11.068.
- [59] A. Gundermann, H. Hein, W. Hofmann, E. Keim, H. Schnabel, and T. Seibert. *Determination of Fracture Mechanics Values on Irradiated Specimens of German PWR Plants (CARISMA)*. Reactor Safety Research - Project 1501284. Areva GmbH, 2008.
- [60] J. Barthelmes, C. Eiselt, H. Hein, W. Hofmann, M. Kaiser, E. Keim, F. Obermeier, and H. Schnabel. *Extension of the Data Base of Fracture Mechanical Characteristics of Irradiated German RPV Materials – Application of the Master Curve Approach for Neutron Fluences in the Upper Bound (CARINA)*. Reactor Safety Research - Project 1501357. Areva GmbH, 2012.
- [61] A. Ulbricht, J. Böhmert, and H. W. Viehrig. „Microstructural and mechanical characterization of radiation effects in model reactor pressure vessel steels.“ *J. ASTM International* 2, JAI12385 (2005). DOI: 10.1520/JAI12385.
- [62] Areva GmbH. *Internal Report*. PTCM-G/2011/de/0043. 2011.

- [63] Areva GmbH. *Internal Report*. NTM-G/2006/de/0242. 2006.
- [64] LONGLIFE. *Deliverable D3.1, Revision 2 "Documentation and data of materials for microstructural analysis"*. 2012.
- [65] H. Worch, W. Pompe, and W. Schatt. *Werkstoffwissenschaft*. 10th Edition. Weinheim: Wiley-VCH Verlag GmbH & Co. KGaA, 2011. 592 pp. ISBN: 978-3-527-32323-4.
- [66] W. Pepperhoff and M. Acet. *Constitution and Magnetism of Iron and its Alloys*. Ed. 2001. Berlin ; New York: Springer, 2001. ISBN: 978-3-540-42433-8.
- [67] K. Popp, H.-P. Schüßler, and H.-W. Viehrig. *Bestrahlungsexperimente zur Untersuchung der Neutronenversprödung von Reaktordruckbehälterstählen*. Report ZfK-679. Zentralinstitut für Kernforschung Rossendorf, 1989.
- [68] H.-U. Barz, B. Böhmer, J. Kohnheiser, and I. Stephan. *Ermittlung der Neutronendosis von bestrahlten WWER-Reaktordruckbehältermaterialien*. Report FZR-87. Forschungszentrum Rossendorf, Institut für Sicherheitsforschung, Germany, 1995.
- [69] R. Chaouadi. *Irradiation effects on the tensile properties of LONGLIFE materials irradiated in the BR2 (SCK-6, FZD-1a and FZD-1b)*. SCK•CEN ER-191. 2012.
- [70] R. Chaouadi and R. Gérard. „Neutron flux and annealing effects on irradiation hardening of RPV materials.“ *J. Nucl. Mater.* 418.1-3 (2011), pp. 137–142. DOI: 10.1016/j.jnucmat.2011.06.012.
- [71] R. Chaouadi. *Personal communication*. Mol, Belgium: SCK, 2012.
- [72] P. Strunz, J. Šaroun, U. Keiderling, A. Wiedenmann, and R. Przenioslo. „General formula for determination of cross-section from measured SANS intensities.“ *J Appl Crystallogr* 33.3 (2000), pp. 829–833. DOI: 10.1107/S0021889899013382.
- [73] U. Keiderling. „The new 'BerSANS-PC' software for reduction and treatment of small angle neutron scattering data.“ *Appl. Phys. A* 74 (2002), pp. 1455–1457. DOI: 10.1007/s003390201561.
- [74] C. D. Dewhurst. *GRASP: Graphical Reduction and Analysis SANS Program*. Grenoble, France: ILL, 2003, pp. 116–119.
- [75] G. Porod. „Die Röntgenkleinwinkelstreuung von dichtgepackten kolloiden Systemen. I. Teil.“ *Colloid Polym. Sci.* 124.2 (1951), pp. 83–114.
- [76] G. Porod. „Die Röntgenkleinwinkelstreuung von dichtgepackten kolloiden Systemen. II. Teil.“ *Colloid Polym. Sci.* 125.2 (1952), pp. 108–122.
- [77] G. Rouen. *Fiches du laboratoire*. Rouen, France: Groupe de Physique des Matériaux, 2014.
- [78] A. Wagner, F. Bergner, A. Ulbricht, and C. Dewhurst. „Small-angle neutron scattering of low-Cu RPV steels neutron-irradiated at 255 °C and post-irradiation annealed at 290 °C.“ *J. Nucl. Mater.* 441.1–3 (2013), pp. 487–492. DOI: 10.1016/j.jnucmat.2013.06.032.

- [79] C. F. Kuang, J. Li, S. G. Zhang, J. Wang, H. F. Liu, and A. A. Volinsky. „Effects of quenching and tempering on the microstructure and bake hardening behavior of ferrite and dual phase steels.“ *Materials Science and Engineering: A* 613 (2014), pp. 178–183. DOI: 10.1016/j.msea.2014.06.100.
- [80] C. Hatzoglou. „Personal communication: Choosing parameters for iso-concentration clustering.“ University of Rouen, 2013.
- [81] M. Schober, E. Eidenberger, P. Staron, and H. Leitner. „Critical Consideration of Precipitate Analysis of Fe-1 at.% Cu Using Atom Probe and Small-Angle Neutron Scattering.“ *Microsc. Microanal.* 17.01 (2011), pp. 26–33. DOI: 10.1017/S1431927610093955.
- [82] F. Bergner, C. Pareige, V. Kuksenko, L. Malerba, P. Pareige, A. Ulbricht, and A. Wagner. „Critical assessment of Cr-rich precipitates in neutron-irradiated Fe-12 at.%Cr: Comparison of SANS and APT.“ *J. Nucl. Mater.* 442.1–3 (2013), pp. 463–469. DOI: 10.1016/j.jnucmat.2013.05.023.
- [83] J. M. Hyde, M. G. Burke, G. D. W. Smith, P. Styman, H. Swan, and K. Wilford. „Uncertainties and assumptions associated with APT and SANS characterisation of irradiation damage in RPV steels.“ *J. Nucl. Mater.* 449.1–3 (2014), pp. 308–314. DOI: 10.1016/j.jnucmat.2013.07.029.
- [84] J.-L. Boutard, V. Badjeck, L. Barguet, C. Barouh, A. Bhattacharya, Y. Colignon, C. Hatzoglou, M. Loyer-Prost, A. L. Rouffié, N. Sallez, H. Salmon-Legagneur, and T. Schuler. „Oxide dispersion strengthened ferritic steels: a basic research joint program in France.“ *J. Nucl. Mater.* Proceedings of the 16th International Conference on Fusion Reactor Materials (ICFRM-16), Beijing, China, 20th - 26th October, 2013 455.1–3 (2014), pp. 605–611. DOI: 10.1016/j.jnucmat.2014.08.059.
- [85] J. J. H. Lim. „Personal communication: HR-TEM observations of Mn-Ni-rich clusters.“ 2013.
- [86] K. P. Gupta. „The Mn-Ni-Si (Manganese-Nickel-Silicon) system.“ *JPED* 27.5 (2006), pp. 529–534. DOI: 10.1007/BF02736466.
- [87] A. Wagner, F. Bergner, R. Chaouadi, H. Hein, M. Hernández-Mayoral, M. Serano, A. Ulbricht, and E. Altstadt. „Effect of neutron flux on the characteristics of irradiation-induced nanostructures and hardening in pressure vessel steels.“ *Acta Mater.* 104 (2016), pp. 131–142. DOI: 10.1016/j.actamat.2015.11.027.
- [88] G. R. Odette and T. Yamamoto. *Advanced Models of LWR Pressure Vessel Embrittlement for Low Flux-Highfluence Conditions*. ID14517/09-834. Battelle Energy Alliance, LLC, 2013.
- [89] A. N. Kolmogorov. „Static theory of metals crystallization.“ *Bull. Acad. Sci. USSR Phys. Ser.* 1 (1937), pp. 355–359.
- [90] M. Avrami. „Kinetics of Phase Change. I General Theory.“ *J. Chem. Phys.* 7.12 (1939), pp. 1103–1112. DOI: 10.1063/1.1750380.

- [91] W. Johnson and K. Mehl. „Reaction Kinetics in Processes of Nucleation and Growth.“ *Trans. Am. Inst. Min. Metall. Pet. Eng.* 195 (1939), pp. 416–458.
- [92] M. Avrami. „Kinetics of Phase Change. II Transformation-Time Relations for Random Distribution of Nuclei.“ *J. Chem. Phys.* 8.2 (1940), pp. 212–224. DOI: 10.1063/1.1750631.
- [93] M. Avrami. „Granulation, Phase Change, and Microstructure Kinetics of Phase Change. III.“ *J. Chem. Phys.* 9.2 (1941), pp. 177–184. DOI: 10.1063/1.1750872.
- [94] J. Christian. „Phase Transformations.“ In: *Physical Metallurgy*. Ed. by R. W. Cahn. Amsterdam; New York: North-Holland Pub. Co.; Wiley, 1965, pp. 443–539.
- [95] H. Reiss, J. R. Patel, and K. A. Jackson. „Approximate analytical solutions of diffusional boundary-value problems by the method of finite zone continuity.“ *J. Appl. Phys.* 48.12 (1977), pp. 5274–5278. DOI: 10.1063/1.323557.
- [96] K. A. Jackson. *Kinetic Processes*. Weinheim, Germany; Chichester, England: Wiley-VCH, 2004. 453 pp. ISBN: 3-527-30694-3.
- [97] L. K. Mansur. „Void Swelling in Metals and Alloys Under Irradiation: An Assessment of the Theory.“ *Nucl. Technol.* 40.1 (1978), pp. 5–34.
- [98] F. Bergner, A. Ulbricht, H. Hein, and M. Kammel. „Flux dependence of cluster formation in neutron-irradiated weld material.“ *J. Phys. Condens. Mater.* 20 (2008), pp. 104262–104267.
- [99] L. Ratke and C. Beckermann. „Concurrent growth and coarsening of spheres.“ *Acta Materialia* 49.19 (2001), pp. 4041–4054. DOI: 10.1016/S1359-6454(01)00286-5.
- [100] M. J. Starink. „On the meaning of the impingement parameter in kinetic equations for nucleation and growth reactions.“ *Journal of Materials Science* 36.18 (2001), pp. 4433–4441. DOI: 10.1023/A:1017974517877.
- [101] I. M. Lifshitz and V. V. Slyozov. „The kinetics of precipitation from supersaturated solid solutions.“ *Journal of Physics and Chemistry of Solids* 19.1–2 (1961), pp. 35–50. DOI: 10.1016/0022-3697(61)90054-3.
- [102] C. Wagner. „Theorie der Alterung von Niederschlägen durch Umlösen (Ostwald-Reifung).“ *Zeitschrift für Elektrochemie, Berichte der Bunsengesellschaft für physikal. Chemie* 65.7–8 (1961), pp. 581–591. DOI: 10.1002/bbpc.19610650704.
- [103] P. Bellon, F. Soisson, and G. Martin. „Steady-states and microstructural evolutions in driven systems.“ *J. Phys. IV* 03 (C7 1993), pp. C7–1977–C7–1979. DOI: 10.1051/jp4:19937316.
- [104] A. Ulbricht and J. Böhmert. „Small angle neutron scattering analysis of the radiation susceptibility of reactor pressure vessel steels.“ *Physica B: Condensed Matter*. Proceedings of the Third European Conference on Neutron Scattering 350.1–3, Supplement (2004), E483–E486. DOI: 10.1016/j.physb.2004.03.126.

- [105] U. Birkenheuer, A. Ulbricht, F. Bergner, and A. Gokhman. „On the formation of mixed vacancy-copper clusters in neutron-irradiated Fe-Cu alloys.“ *J. Phys.: Conf. Ser.* 247.1 (2010), p. 012011. DOI: 10.1088/1742-6596/247/1/012011.
- [106] J. H. Yao, K. R. Elder, H. Guo, and M. Grant. „Theory and simulation of Ostwald ripening.“ *Phys. Rev. B* 47.21 (1993), pp. 14110–14125. DOI: 10.1103/PhysRevB.47.14110.
- [107] K. Dohi, K. Nishida, A. Nomoto, N. Soneda, H. Matsuzawa, and M. Tomimatsu. „Effect of Additional Irradiation at Different Fluxes on RPV Embrittlement.“ *Proc. ASME, PVP Div. Conf.* (2009), pp. 403–409. DOI: 10.1115/PVP2009-77658.
- [108] N. Soneda, K. Dohi, K. Nishida, A. Nomoto, M. Iwasaki, S. Tsuno, T. Akiyama, S. Watanabe, and T. Ohta. „Flux effect on neutron irradiation embrittlement of reactor pressure vessel steels irradiated to high fluences.“ *Fontevraud 7 - Contrib. Mater. Investig. Improve Saf. Perform. LWRs Avignon Fr.* (2010).
- [109] G. Odette, T. Yamamoto, and D. Klingensmith. „On the effect of dose rate on irradiation hardening of RPV steels.“ *Phil. Mag.* 85.4-7 (2005), pp. 779–797. DOI: 10.1080/14786430412331319910.
- [110] A. Seeger. „Theory of radiation damage and radiation hardening.“ *Second Int. Conf. Peac. Uses At. Energy Geneva Vol. 6* (1958), pp. 250–273.
- [111] D. J. Bacon, U. F. Kocks, and R. O. Scattergood. „The effect of dislocation self-interaction on the orowan stress.“ *Philos. Mag.* 28.6 (1973), pp. 1241–1263. DOI: 10.1080/14786437308227997.
- [112] K. C. Russell and L. M. Brown. „A dispersion strengthening model based on differing elastic moduli applied to the iron-copper system.“ *Acta Metallurgica* 20.7 (1972), pp. 969–974. DOI: 10.1016/0001-6160(72)90091-0.
- [113] J. Friedel. „CXXX. On the linear work hardening mate of face-centred cubic single crystals.“ *Philos. Mag. Ser. 7* 46.382 (1955), pp. 1169–1186. DOI: 10.1080/14786441108520630.
- [114] F. Kroupa and P. B. Hirsch. „Elastic interaction between prismatic dislocation loops and straight dislocations.“ *Discuss. Faraday Soc.* 38 (1964), pp. 49–55.
- [115] S. J. Zinkle and Y. Matsukawa. „Observation and analysis of defect cluster production and interactions with dislocations.“ *J. Nucl. Mater. Proceedings of the 11th International Conference on Fusion Reactor Materials (ICFRM-11)* 329–333, Part A (2004), pp. 88–96. DOI: 10.1016/j.jnucmat.2004.04.298.
- [116] D. Tabor. „The physical meaning of indentation and scratch hardness.“ *Br. J. Appl. Phys.* 7.5 (1956), p. 159. DOI: 10.1088/0508-3443/7/5/301.
- [117] W. Xiong, H. Ke, R. Krishnamurthy, P. Wells, L. Barnard, G. R. Odette, and D. Morgan. „Thermodynamic models of low-temperature Mn–Ni–Si precipitation in reactor pressure vessel steels.“ *MRS Commun.* 4.03 (2014), pp. 101–105. DOI: 10.1557/mrc.2014.21.

- [118] P. Pareige, B. Radiguet, and A. Barbu. „Heterogeneous irradiation-induced copper precipitation in ferritic iron–copper model alloys.“ *J. Nucl. Mater.* Proceedings of the E-MRS 2005 Spring Meeting Symposium N on Nuclear Materials (including the 10th Inert Matrix Fuel Workshop) 352.1–3 (2006), pp. 75–79. DOI: 10.1016/j.jnucmat.2006.02.073.
- [119] U. Birkenheuer, F. Bergner, A. Gokhman, and M. Posselt. *Tested rate theory model of microstructure evolution in FeCuNi alloys*. Deliverable D1-3.13b, FP7-232612-PERFORM 60. 2012.
- [120] H.-W. Viehrig, M. Houska, and E. Altstadt. „Radiation and annealing response of WWER 440 beltline welding seams.“ *J. Nucl. Mater.* 456 (2015), pp. 334–343. DOI: 10.1016/j.jnucmat.2014.10.004.
- [121] E. Meslin, M. Lambrecht, M. Hernández-Mayoral, F. Bergner, L. Malerba, P. Pareige, B. Radiguet, A. Barbu, D. Gómez-Briceño, A. Ulbricht, and A. Almazouzi. „Characterization of neutron-irradiated ferritic model alloys and a RPV steel from combined APT, SANS, TEM and PAS analyses.“ *J. Nucl. Mater.* 406 (2010), pp. 73–83.
- [122] E. Meslin, B. Radiguet, P. Pareige, and A. Barbu. „Kinetic of solute clustering in neutron irradiated ferritic model alloys and a French pressure vessel steel investigated by atom probe tomography.“ *J. Nucl. Mater.* 399.2–3 (2010), pp. 137–145. DOI: 10.1016/j.jnucmat.2009.11.012.
- [123] E. Meslin, B. Radiguet, P. Pareige, C. Toffolon, and A. Barbu. „Irradiation-Induced Solute Clustering in a Low Nickel FeMnNi Ferritic Alloy.“ *Exp Mech* 51.9 (2011), pp. 1453–1458. DOI: 10.1007/s11340-011-9476-1.
- [124] E. Meslin, A. Barbu, L. Boulanger, B. Radiguet, P. Pareige, K. Arakawa, and C. C. Fu. „Cluster-dynamics modelling of defects in alpha-iron under cascade damage conditions.“ *J. Nucl. Mater.* Proceedings of the Symposium on Microstructural Processes in Irradiated Materials, as part of the annual meeting of The Minerals, Metals & Materials Society 382.2–3 (2008), pp. 190–196. DOI: 10.1016/j.jnucmat.2008.08.010.
- [125] A. Gokhman and F. Bergner. „Cluster dynamics simulation of point defect clusters in neutron irradiated pure iron.“ *Radiat. Eff. Defects Solids* 165.3 (2010), pp. 216–226. DOI: 10.1080/10420151003631928.
- [126] M. I. Pascuet, N. Castin, C. S. Becquart, and L. Malerba. „Stability and mobility of Cu–vacancy clusters in Fe–Cu alloys: A computational study based on the use of artificial neural networks for energy barrier calculations.“ *J. Nucl. Mater.* 412.1 (2011), pp. 106–115. DOI: 10.1016/j.jnucmat.2011.02.038.
- [127] A. Al-Motasem, M. Posselt, F. Bergner, and U. Birkenheuer. „Structure, energetics and thermodynamics of copper–vacancy clusters in bcc-Fe: An atomistic study.“ *J. Nucl. Mater.* 414.2 (2011), pp. 161–168. DOI: 10.1016/j.jnucmat.2011.02.051.

- [128] A. Al-Motasem, M. Posselt, and F. Bergner. „Nanoclusters in bcc-Fe containing vacancies, copper and nickel: Structure and energetics.“ *J. Nucl. Mater.* 418.1–3 (2011), pp. 215–222. DOI: 10.1016/j.jnucmat.2011.07.002.
- [129] Y. Nagai, Z. Tang, M. Hasegawa, T. Kanai, and M. Saneyasu. „Irradiation-induced Cu aggregations in Fe: An origin of embrittlement of reactor pressure vessel steels.“ *Phys. Rev. B* 63.13 (2001), p. 134110. DOI: 10.1103/PhysRevB.63.134110.
- [130] F. Vurpillot, A. Bostel, and D. Blavette. „Trajectory overlaps and local magnification in three-dimensional atom probe.“ *Appl. Phys. Lett.* 76.21 (2000), p. 3127. DOI: 10.1063/1.126545.
- [131] A. Morley, G. Sha, S. Hirosawa, A. Cerezo, and G. Smith. „Determining the composition of small features in atom probe: bcc Cu-rich precipitates in an Fe-rich matrix.“ *Ultramicroscopy* 109.5 (2009), pp. 535–540. DOI: 10.1016/j.ultramicro.2008.09.010.
- [132] M. K. Miller and M. G. Burke. „Characterization of irradiated A533B pressure vessel steel weld.“ *J. Phys. Colloq.* 48 (C6 1987), pp. C6–429–C6–434. DOI: 10.1051/jphyscol:1987670.
- [133] P. Pareige, J. C. Van Duysen, and P. Auger. „An APFIM study of the microstructure of a ferrite alloy after high fluence neutron irradiation.“ *Applied Surface Science* 67.1–4 (1993), pp. 342–347. DOI: 10.1016/0169-4332(93)90336-A.
- [134] M. Eldrup, B. N. Singh, S. J. Zinkle, T. S. Byun, and K. Farrell. „Dose dependence of defect accumulation in neutron irradiated copper and iron.“ *J. Nucl. Mater.* 307–311, Part 2 (2002), pp. 912–917. DOI: 10.1016/S0022-3115(02)01160-1.
- [135] E. Vincent, C. S. Becquart, and C. Domain. „Ab initio calculations of self-interstitial interaction and migration with solute atoms in bcc Fe.“ *J. Nucl. Mater.* 359.3 (2006), pp. 227–237. DOI: 10.1016/j.jnucmat.2006.08.022.
- [136] P. Olsson, T. P. C. Klaver, and C. Domain. „Ab initio study of solute transition-metal interactions with point defects in bcc Fe.“ *Phys. Rev. B* 81.5 (2010), p. 054102. DOI: 10.1103/PhysRevB.81.054102.
- [137] H. Huang, B. Radigue, P. Todeschini, G. Chas, and P. Pareige. „Atom Probe Tomography characterization of the microstructural evolution of a low copper reactor pressure vessel steel under neutron irradiation.“ *MRS Online Proc. Libr.* 1264 (2010), pp. 235–241. DOI: 10.1557/PROC-1264-BB05-18.
- [138] R. E. Stoller. „Modeling the influence of irradiation temperature and displacement rate on hardening due to point defect clusters in ferritic steels.“ *Eff. Radiat. Mater. 16th Int. Symp.* ASTM STP 1175 (1993), pp. 394–423.

- [139] R. Kasada and A. Kimura. „Modeling of microstructure evolution and mechanical property change of reduced-activation martensitic steel during varying-temperature irradiation.“ *J. Nucl. Mater.* 9th Int. Conf. on Fusion Reactor Materials 283–287, Part 1 (2000), pp. 188–192. DOI: 10.1016/S0022-3115(00)00306-8.
- [140] R. Kasada, T. Kudo, A. Kimura, H. Matsui, and M. Narui. „Effects of neutron dose, dose rate and irradiation temperature on the irradiation embrittlement of a low-copper reactor pressure vessel steel.“ *J ASTM Int* 2 (2005), JAI12399.
- [141] G. S. Was and T. Allen. „Intercomparison of microchemical evolution under various types of particle irradiation.“ *J. Nucl. Mater.* 205 (1993), pp. 332–338. DOI: 10.1016/0022-3115(93)90097-1.
- [142] G. S. Was. *Fundamentals of radiation materials science: metals and alloys*. Springer, 2007. 839 pp. ISBN: 978-3-540-49471-3.
- [143] R. B. Jones and T. J. Williams. „The dependence of radiation hardening and embrittlement on irradiation temperature.“ *ASTM STP* 1270 (1996), pp. 569–590.
- [144] R. B. Jones. Personal communication. 2011.

LIST OF PUBLICATIONS

A. Wagner, A. Ulbricht, F. Bergner, and E. Altstadt. „Influence of the copper impurity level on the irradiation response of reactor pressure vessel steels investigated by SANS.“ *Nucl. Instrum. Meth. B* 280 (2012), pp. 98–102. DOI: 10.1016/j.nimb.2012.03.008

A. Wagner, F. Bergner, A. Ulbricht, and C. Dewhurst. „Small-angle neutron scattering of low-Cu RPV steels neutron-irradiated at 255 °C and post-irradiation annealed at 290 °C.“ *J. Nucl. Mater.* 441.1–3 (2013), pp. 487–492. DOI: 10.1016/j.jnucmat.2013.06.032

F. Bergner, C. Pareige, V. Kuksenko, L. Malerba, P. Pareige, A. Ulbricht, and A. Wagner. „Critical assessment of Cr-rich precipitates in neutron-irradiated Fe–12 at%Cr: Comparison of SANS and APT.“ *J. Nucl. Mater.* 442.1–3 (2013), pp. 463–469. DOI: 10.1016/j.jnucmat.2013.05.023

A. Wagner, F. Bergner, R. Chaouadi, H. Hein, M. Hernández-Mayoral, M. Serrano, A. Ulbricht, and E. Altstadt. „Effect of neutron flux on the characteristics of irradiation-induced nanofeatures and hardening in pressure vessel steels.“ *Acta Mater.* 104 (2016), pp. 131–142. DOI: 10.1016/j.actamat.2015.11.027

I. Hilger, F. Bergner, A. Ulbricht, A. Wagner, T. Weißgärber, B. Kieback, C. Heintze, and C. D. Dewhurst. „Investigation of Spark Plasma Sintered Oxide-Dispersion Strengthened Steels by Means of Small-Angle Neutron Scattering.“ *J. Alloys Compd.* 685 (2016), pp. 927–935. DOI: 10.1016/j.jallcom.2016.06.238

LIST OF FIGURES

Figure 1	Technical drawing and photograph of a VVER-type RPV. . . .	2
Figure 2	Schematic plot of the evolution of the irradiation damage. . .	4
Figure 3	(a) Schematic representation of a collision cascade. (b) Simulated PD distribution.	5
Figure 4	Geometrical relationship between the incident and scattered wave vector.	12
Figure 5	Form factor of a spherical scatterer with radius $R = 1$ nm as a function of QR	14
Figure 6	Basic set-up of an APT device.	21
Figure 7	Geometric relations for the APT image compression factor G	23
Figure 8	(a) Top view of a 3D APT reconstruction. (b) Magnified view of the pole region.	25
Figure 9	Magnified view of a TOF mass spectrum.	26
Figure 10	2D illustration of the iso-concentration algorithm.	27
Figure 11	Temperature profile of a typical heat treatment of RPV steel.	31
Figure 12	Cutting profile for SANS specimens.	35
Figure 13	Schematic view of a SANS set-up.	36
Figure 14	SANS scattering intensity pattern.	39
Figure 15	Schematic illustration of electro-polishing procedure.	41
Figure 16	APT needle viewed in an optical microscope and in a TEM.	42
Figure 17	Magnetic scattering curves and size distribution of flux-effect samples (GBC, GWC, GWD)	46
Figure 18	Magnetic scattering curves and size distribution of flux-effect samples (BBA, FWA).	47
Figure 19	Characteristics of irradiation-induced clusters and hardness increase as a function of the neutron flux.	49
Figure 20	Changes of cluster parameters and hardness increase as a function of flux.	50
Figure 21	Magnetic scattering curves and size distribution of JPB and JPC irradiated at the RH reactor.	52
Figure 22	Magnetic scattering curves and size distribution of JPB and JPC irradiated at the BR2 reactor.	53
Figure 23	Irradiation-induced cluster-volume fraction and hardness increase of JPB and JPC as function of neutron fluence for RH and BR2 irradiation.	55
Figure 24	Three-dimensional element map of the non-irradiated reference material.	57
Figure 25	Reconstructed APT-sample volumes of the medium-fluence samples of JPC.	59

Figure 26	Reconstructed APT-sample volumes of the high-fluence samples of JPC.	61
Figure 27	APT Cluster-size distribution of JPC RH for the medium- and the high-fluence condition.	62
Figure 28	Evolution of the cluster-volume fraction with neutron fluence of material JPC RH determined by means of SANS and APT.	63
Figure 29	Cluster composition for material JPC RH for medium- and high-fluence samples as a function of cluster radius.	64
Figure 30	Ternary plot of the cluster composition considering only the Mn, Ni and Si concentrations.	65
Figure 31	Normalized cluster characteristics as a function of the neutron flux, showing the radius and the volume fraction.	68
Figure 32	Evolution of the net mean RED distance $\langle \delta^* \rangle^2$ with neutron flux.	71
Figure 33	Normalized cluster characteristics as a function of the neutron flux.	73
Figure 34	Comparison of the flux dependence of hardening models for deterministic growth.	74
Figure 35	Comparison of yield-stress increase from hardness data versus yield-stress increase predicted by different hardening models.	76
Figure 36	Effect of lower detection limit on the measured volume fraction of two cluster populations from low and high fluence.	80
Figure 37	Schematic overview of irradiation-induced cluster evolution in low-Cu RPV steel in three stages.	82
Figure 38	APT element distribution of a Cu-free MNCs from JPC-RH at high neutron fluence.	84
Figure 39	APT cluster-volume fraction of material JPC-RH categorized according to the Cu content.	86

LIST OF TABLES

Table 1	Chemical composition of the materials investigated.	30
Table 2	Irradiation conditions of the samples investigated.	32
Table 3	Yield stress and yield-stress increase for the materials and irradiation conditions studied.	34
Table 4	Main parameters and set-up of the SANS experiments.	37
Table 5	Parameters of irradiation-induced clusters and hardness increase of the flux-effect samples.	48
Table 6	The parameters of the irradiation-induced clusters and hardness increase for material JPB and JPC under RH and BR2 irradiation conditions.	54
Table 7	Chemical composition of material JPC RH for the unirradiated reference, the medium- and high-fluence condition derived from APT.	58
Table 8	Enrichment factors of each element in the clusters in JPC.	62
Table 9	The parameters of the cluster population of material JPC RH determined by APT and SANS.	63
Table 10	APT cluster characterization of JPC-RH split according to the Cu content.	86

ACKNOWLEDGMENTS

Die Durchführung der Experimente und die Anfertigung dieser Arbeit ist nur durch die Unterstützung zahlreicher Menschen möglich gewesen.

An erster Stelle möchte ich mich bei Prof. Reinhard Krause-Rehberg, Dr. Eberhard Altstadt und Dr. habil. Frank Bergner für die Gelegenheit zur Durchführung dieser Arbeit bedanken. Dabei gilt mein besonderer Dank meinem Betreuer Dr. habil. Frank Bergner. Seine wertvollen Anregungen und Denkanstöße habe ich immer sehr geschätzt.

Ich möchte mich bei Dr. Andreas Ulbricht bedanken für die Hilfsbereitschaft und Unterstützung während der SANS-Experimente. Dabei standen uns auch Wissenschaftler vor Ort zur Seite. Mein Dank gilt hier vor allem Charles Dewhurst und Dr. Peter Lindner (ILL Grenoble), Dr. Ferenc Gillemot und Dr. Gyula Török (KFKI Budapest), Dr. Uwe Keiderling (HZ Berlin) und Dr. Marie-Hélène Mathon (LLB Saclay).

Für die einmalige Gelegenheit APT-Untersuchungen an aktiven Proben durchzuführen, möchte ich mich herzlich bei Dr. Bertrand Radiguet (GPM Rouen) bedanken. Mein Dank geht auch an Dr. Constantinos Hatzoglou (GPM Rouen), Prof. Naoki Soneda und Kenji Nishida (CRIEPI Tokio) für die erkenntnisreichen Diskussionen zur Gegenüberstellung von SANS und APT.

Ich danke Hieronymus Hein (Areva GmbH), Dr. Rachid Chaouadi (SCK-CEN Mol), Dr. Marta Serrano Garcia und Dr. Mercedes Hernández-Mayoral (CIEMAT Madrid) für die Bereitstellung von Proben, für zusätzliche Neutronenbestrahlungen sowie für die wertvollen Diskussionen zu Flusseffekten.

Bei Dr. Hans-Werner Viehrig möchte ich mich für seine Hilfe in metallurgischen Fragestellungen bedanken. Mein besonderer Dank geht an Mario Houska, Jens Pietzsch, Dr. Gudrun Müller und Michaela Roßner für ihre Unterstützung im Metallografielabor und an der Drahterodiermaschine. Ohne die präzise Probenpräparation hätten die APT-Experimente nicht erfolgreich durchgeführt werden können.

Für die freundliche Unterstützung während der GiPS-Messungen bedanke ich mich bei Dr. Maik Butterling, Wolfgang Anwand und Dr. Andreas Wagner.

Bei Isa, Conny, Sonja und Wolfgang möchte ich mich besonders für ihre Unterstützung und die vielen selbstgestopften und getrunkenen Kännchen im Kinderzimmer bedanken.

Von ganzem Herzen möchte ich mich bei meiner Frau Carina für ihre unermüdliche Unterstützung und ihren Zuspruch während meiner Promotionszeit bedanken.

DANKESCHÖN!

Teile dieser Arbeit wurden durch das Bundesministeriums für Wirtschaft und Technologie BMWi unter der Vorhabensnummer 1501393, Projekt „Langzeitspezifische Alterungseffekte in RDB-Stahl“, gefördert. Zusätzlich wurde diese Arbeit durch das 7. Forschungsrahmenprogramm (FP7) der Europäischen Union unter der Vorhabensnummer 249360, Projekt LONGLIFE, gefördert.

CURRICULUM VITAE

PERSÖNLICHE DATEN

Name	Arne Wagner
Geburtsdatum	13. Mai 1982
Geburtsort	Kronstadt
Staatsangehörigkeit	Deutsch

AKADEMISCHER WERDEGANG

Seit 11/2010	Dissertation am Helmholtz-Zentrum Dresden-Rossendorf, Einreichung am Physikalischen Institut der Martin-Luther-Universität Halle-Wittenberg. Titel: <i>Long-term irradiation effects on reactor-pressure vessel steels: Investigations on the nanometer scale.</i>
08/2009 – 08/2010	Diplomarbeit am Fraunhofer ISC, Würzburg, eingereicht am Physikalischen Institut der Universität Bonn. Titel: <i>Der Einfluss von Dotierung auf das Sinterverhalten (Diffusion) von Al₂O₃-Keramiken.</i>
08/2007 – 08/2009	Hauptstudium der Physik an der Universität Bonn.
10/2006 – 04/2008	Studium der Geologie an der Universität Bonn.
10/2002 – 08/2007	Studium der Physik an der Universität Bonn, Vordiplom.

BERUFLICHER WERDEGANG

Seit 10/2015	Physiker, Vorentwicklung Machine Vision & Learning bei Magnetische Pruefanlagen GmbH, Reutlingen.
01/2015 – 09/2015	Gastwissenschaftler am Helmholtz-Zentrum Dresden-Rossendorf.
11/2010 – 12/2014	Wissenschaftlicher Mitarbeiter am Helmholtz-Zentrum Dresden-Rossendorf.
09/2010 – 10/2010	Wissenschaftlicher Mitarbeiter am Kompetenzfeld Sinterwerkstoffe des Fraunhofer ISC Würzburg.
08/2009 – 08/2010	Studentische Hilfskraft am Kompetenzfeld Sinterwerkstoffe des Fraunhofer ISC Würzburg.
08/2005 – 01/2009	Studentische Hilfskraft, Arbeitsgruppe Polarisiertes Target am Physikalischen Institut der Universität Bonn.

DECLARATION

Hiermit erkläre ich an Eides statt, dass ich die vorliegende Arbeit selbstständig und ohne fremde Hilfe verfasst, andere als die von mir angegebenen Quellen und Hilfsmittel nicht benutzt und die den benutzten Werken wörtlich oder inhaltlich entnommenen Stellen als solche kenntlich gemacht habe.

Des Weiteren erkläre ich, dass ich mich bisher keiner weiteren Doktorprüfung unterzogen habe. Ich habe die Dissertation in der gegenwärtigen oder einer anderen Fassung an keiner anderen Fakultät im In- oder Ausland eingereicht.

Halle (Saale), den 04.11.2016

Arne Wagner